**“FEDERICO II” UNIVERSITY OF NAPLES**

Ph.D. in Chemical Sciences - XXX Cycle

# FUNCTIONAL CHARACTERIZATION OF SYNTHETIC METALLOPORPHYRIN-CONTAINING ENZYMES

Vincenzo Firpo

**ADVISOR:** Prof. Angela Lombardi

**EXAMINER:** Prof. Pietro Pucci

**COORDINATOR:** Prof. Luigi Paduano

# SUMMARY

A growing attention is devoted to metalloenzymes has received increasing attention, due to the variety of complex chemical transformations that these molecules are able to perform. The excellent catalytic potential of metalloenzymes derives from their aptitude to form highly reactive intermediates, resulting from the accessibility metal ion to different oxidation states, required for the catalysis. In the effort to resemble the catalytic profile of natural metalloenzymes while improving their chemical stability, a wide variety of bioinspired systems have been devised, obtained modifying either the metal cofactor or the protein matrix. In this context, the miniaturization of heme-containing metalloenzymes has been conveniently developed, to identify the minimal structural elements required for catalytic activity, as well as to build up fully synthetic metalloenzymes enabling new opportunities in catalysis. Among heme-protein models with catalytic potential, metalloporphyrin-peptide conjugates (such as those known as "Mimochromes") have emerged as an important class of artificial enzymes. The structure of Mimochromes – composed of a porphyrin core covalently linked to two peptide chains, resulting into helix-heme-helix sandwich structures – has been devised to closely resemble the active site of natural peroxidases. The characterization of these compounds has shed new light on our understanding of the structure-function relationships in heme-proteins. Most important, because of their considerable chemical robustness and versatility, Mimochromes have demonstrated to represent promising candidates in catalysis.

*Aims*. The development of a novel artificial heme-enzyme belonging to the Mimochrome family (Mimochrome VIa or MC6a) and the evaluation of its catalytic potential have been explored during this PhD project. First of all, the design, synthesis and characterization of $Fe^{III}$-containing MC6a ($Fe^{III}$-MC6a) have been performed. The substitution of specific amino acid residues has been carried out by rational design, with the aim to evaluate the activity of the molecule as a peroxidase biomimetic, investigating its catalytic properties in a specific model reaction. Furthermore, the analysis of the reactivity of MC6a containing a $Co^{III}$ ion (Co-MC6a) has been carried out. These studies, which were carried out in collaboration with Prof. K. L. Bren (University of Rochester, NY), were aimed to investigate the potential MC6a in hydrogen evolution reaction (HER), in order to employ the catalyst in water splitting. Co-MC6a is intended to represent an alternative to natural hydrogenases, whose use as catalysts for HER is limited by their sensitivity to molecular oxygen.

*Results*. *$Fe^{III}$-MC6a as a peroxidase-like catalyst.* Compared to the best candidate among previous Mimochrome members, $Fe^{III}$-MC6a was found to act as an even more efficient peroxidase-like catalyst, since it was able to oxidize the model substrate ABTS with a much higher turnover number (from 5900 to 14000) and turnover frequency (from 2300 to 5900 $s^{-1}$). This feature has been correlated with the presence of two Aib residues in place of $Gln^3$ e $Ser^7$ on the distal peptide (*D* chain). Indeed, this substitution has been found to significantly increase the conformational rigidity of the peptide chain, contributing to a higher preorganization of the molecule toward protein folding. Furthermore, the catalyst was endowed with a higher robustness

if compared to all previous Mimochrome members (up to a two-fold increase), although at the cost of a minor affinity toward $H_2O_2$ (up to a three-fold increase of $K_M$ value). In this case, it has been supposed that the larger hydrophobic character of the (*D*) chain, due to the presence of Aib residues, may have resulted into additional interactions between the peptide chain and the porphyrin ring, thereby providing a more compact structure, which protects the metal cofactor from $H_2O_2$-mediated bleaching.

*$Co^{III}$-MC6a as a hydrogenase-like catalyst.* Differently from most natural enzymes or synthetic organometallic biomimetics, Co-MC6a was found to work as a water-soluble catalyst in the HER, active at neutral pH and in the presence of molecular oxygen. In addition, compared to previous Co-porphyrin based synthetic enzymes (e.g. Co-MP11), Co-MC6a shows similar turnover frequency and overpotential values but with much higher turnover numbers (up to 300000), retaining its activity even after several hours. Interestingly, the comparative analysis of Co-MP11 with Co-MC6a enabled to correlate the overpotential value in HER with the enzyme folding, since the latter beneficially affects the catalytic performance. In addition, preliminary SAR studies have been undertaken, suggesting that a correlation exists between primary coordination shell of the enzyme and its efficacy in the HER. The result of this study will allow exploring the chemical space enabling further improvement in the enzyme-like properties of the catalyst.

*Conclusions*. The results obtained during this PhD thesis represent a significant improvement in our knowledge of peptide-based artificial metalloenzymes, as they have contributed to provide the

most advanced candidate with catalytic potential within the Mimochrome family. Future endeavors will be addressed to an in-depth study of the structural requirements for enzymatic activity, in order to develop new catalysts, even higher performing respect to natural metalloenzymes. Furthermore, given the possibility to easily change the metal cofactors as well as their coordination spheres, efforts will be focused in widening the repertoire of reactions and thereby the potential applications of these enzymes.

*Work outline*. This PhD thesis has been subdivided in two major sections. The first section contains a general overview on natural heme-enzymes (their occurrence, structure and catalytic activity) and on the corresponding bio-inspired mimetics with catalytic activity. Herein, the results concerning the design, synthesis, characterization and evaluation of the catalytic properties of Fe-MC6a are presented. The second section is focused on the water splitting reaction, paying main attention on the role of natural hydrogenases and synthetic biomimetics as catalysts in the HER. The results related to the catalytic potential of Co-MC6a are eventually reported, and compared with those obtained for other Co-containing catalysts.

.

# *TABLE OF CONTENTS*

## SECTION 2

**Natural and Artificial Hydrogenases in Water Splitting Reaction** 84

# *LIST OF ABBREVIATIONS*

Abs: Absorbance
ABTS: 2,2'-azino-bis(3-ethylbenzthiazoline-6-sulphonic acid)
Ac: Acetyl
ACN: Acetonitrile
Aib: 2-amino-2-methylpropanoic acid
Arg: Arginine
Asn: Asparagine
Asp: Aspartic acid
Boc: t-Butoxycarbonyl
CD: Circular dichroism
CDL: Curve Desolvation Line
CT: Charge Transfer
CTM:c-type Cytochrome Maquette
CV: Cyclic Voltammetry
Cys: Cysteine
D: Decapeptide
Dab: 2,4-Diaminobutyric acid
DCM: Dichloromethane
DIEA: Ethyldiisopropylamine
DMF: *N,N*-Dimethylformamide
DPIX: Deuteroporphyrin IX
EDT: 1,2-Ethanedithiol
ee: Enantiomeric Excess
EPR: Electron paramagnetic resonance
Eq.: equivalent
ESI-MS: Electrospray ionization mass spectrometry
Fmoc: 9-Fluorenylmethoxycarbonyl
GC: Gas Chromatography
Gln: Glutamine

Glu: Glutamic acid
GP: Guanylylpyrodinol
HATU: *N*-[(Dimethylamino)-1*H*-1,2,3-triazolo-[4,5-*b*] pyridin- 1-ylmethylene]-*N*-methylmethanaminium hexafluorophosphate *N*-oxide
HER: Hydrogen Evolution Reaction
HFIP: 1,1,1,3,3,3-Hexafluoro-2-propanol
His: Histidine
HMDE: Hanging Mercury Drop Electrode
HOBt: N-hydroxybenzotriazole
HPLC: High Performance Liquid Chromatography
HRP: Horseradish peroxidase
HS: High spin
Ile: Isoleucine
IUPAC: International Union of Pure and Applied Chemistry
Km: Michaelis-Menten Costant
KPi: Potassium Phosphate
Leu: Leucine
Lys: Lysine
MC6a: Mimochrome VIa
MCD: Magnetic circular dichroism
Met: Methionine
Methenyl-$H_4$MPT:Methenyltetrahydromethanpterin
Mmt: (4-methoxyphenyl)diphenylmethyl
MP: Microperoxidase
MTBE: Methyl-*t*-butyl ether
Mtt: (4-methylphenyl)diphenylmethyl
NMP: N-Methyl-2-pyrrolidone
NMR: Nuclear magnetic resonance
Orn: 2,5-Diaminopentanoic acid
Pbf: 2,2,4,6,7-Pentamethyldihydrobenzofuran-5-sulfonyl
PCET: Proton Coupled Electron Transfer
PDB: Protein Data Bank

Pro: Proline
PyBop: (Benzotriazol-1-yloxy)tripyrrolidinophosphonium hexafluorophosphate
QS: Quantum-mechanical admixed spin
$R_f$: Retention factor
RMD: Restrained molecular dynamics
RP-HPLC: Reverse Phase - High Performance Liquid Chromatography
RP: Reverse Phase
$R_t$: Retention time
RT: Room Temperature
SAR: Structure and Activity Relationship
SCE: Saturated Calomel Electrode
Ser: Serine
T.O.N.: Turnover number
tBu: *tert*-butyl
TD: Tetradecapeptide
TES: Triethylsilane
Tf: Triflic
TFA: Trifluoroacetic acid
TFE: 2,2,2-trifluoroethanol
Thr: Threonine
TIS: Triisopropylsilane
TLC: Thin Layer Chromatography
Trt: Trityl
Tyr: Tyrosine

# *PREFACE*

Metalloproteins constitute a huge family of proteins that contain a metal ion cofactor. It has been estimated that approximately the fifty percent of all known proteins are metalloproteins.[1] Over 3-billion years of evolution allowed nature to select specific metals, based on their properties and bioavailability. In proteins, metal ions play a crucial role in performing a wide range of fundamental biological functions, ranging from structure stabilization, signal transduction, oxidation reactions, photochemical reactions, or the protection against toxic and mutagenic agents.[2] Members of metalloprotein family that have enzymatic functions are called metalloenzymes. Transition metals are commonly found in metalloproteins. Their peculiarity is due to the partially filled *d* orbitals; this contributes to the rich variety of spectroscopic, magnetic, and catalytic properties exhibited by the complexes of transition metals, which are able to form complexes with a wide type of ligands.[3]

Ligands can be defined as atoms or groups of atoms capable to donate an electron pair (Lewis base) to the metal (Lewis acid). They are classified as monodentate (or polydentate) ligands if one (or more) electron pair is donated to the metal ion. In metalloproteins the polypeptide chain provides ligands to metal ions: these are named endogenous ligands. Amino acids typically participate in coordination through their side chains containing sulfur, oxygen or nitrogen as donor atoms. Common coordinating amino acid are histidine (His), aspartic acid (Asp), cysteine (Cys), glutamic acid (Glu), methionine (Met). *Vice versa*, tyrosine (Tyr), serine (Ser), lysine (Lys), glutamine (Gln), asparagine (Asn), threonine (Thr), are less commonly present.

Metal ions in proteins can be also coordinated by exogenous ligands, which are not delivered by polypeptide chains. They comprise small inorganic entities, such as oxide, water, hydroxide as well as organic macrocyclic ligands, such as porphyrins.[4]

Porphyrins are a group of aromatic macrocycles, composed of four modified pyrrole subunits interconnected at their α carbon atoms via methine bridges. The porphyrin ring presents two imidazole-like nitrogens and two pyrrole-like nitrogens, for a total of four coordinating positions. Metal is enclosed at the center of the porphyrin ring (Figure i).

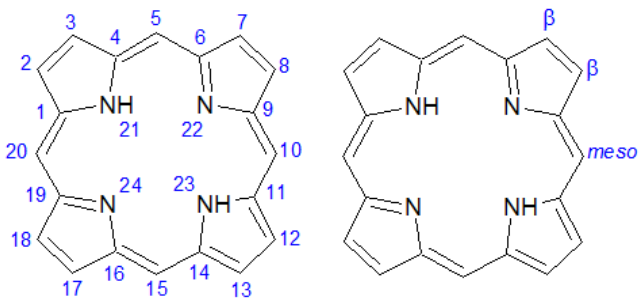


**Figure i.** Chemical structure and numbering scheme, according to IUPAC nomenclature of the porphyrin macrocycle. The 2, 3, 7, 8, 12, 13, 17 and 18 positions are defined *beta* positions, whereas 5, 10, 15 and 20 are *meso* positions.

The prosthetic group is defined as the non-amino acid portion of a conjugated protein. Examples include cofactors such as flavines of cytochromes as well as lipids and polysaccharides, which are the prosthetic groups of lipoproteins and glycoproteins, respectively.[5]

Cofactors are organic molecules or ions (usually metal ions) that are required by an enzyme for its activity. They may be attached

either loosely or tightly to the enzyme. A cofactor binds with its associated protein (apo-enzymes), which is functionally inactive, to form the active enzyme (holo-enzyme).[5]

The second coordination sphere contains those groups interacting with the first coordination sphere ligands. The second coordination sphere modulates metal center activity tuning redox potential, assisting substrate binding/activation, and can provide extra charges for metal stabilization. The number of atoms involved in coordination spheres depends on the size of the metal ion and the sizes of the ligand atoms.[2] Several coordination numbers and geometries are accessible among the metal ions; however, the most found coordination numbers are four and six.

Coordination numbers and geometry in metalloproteins are related to the function that the metal ion achieves. For example, structural sites, which generally stabilize or direct the folding of the protein, exhibit common, coordinately saturated geometries that are well preceded in small-molecule/metal ion complexes. By contrast, functional metal-binding sites often show more unusual ligation geometries, which are largely pre-organized in the folded *apo*-protein.

The biological functions of metalloproteins are strictly related to protein composition, architecture, and to the metal ion. An important feature of metal ions is that each metal presents a characteristic chemistry and then metalloprotein characteristics depend on it.[6] Moreover metal properties can be modulated by the protein environment. This fine modulation is realized through the coordination of different amino acids to the metal, or through the variation of some behaviors of the site, such as the charge distribution, hydrophobicity or hydrogen bond interaction.

The metal binding site, composed by one or more metal ions, coordinating protein side chains, and exogenous ligands define the first coordination sphere. Metal cofactors in proteins play five main roles:

- structural - stabilization of protein tertiary and/or quaternary structure;
- metal storage - absorption, binding, and release of metals;
- electron transfer - uptake, release;
- carrier – small molecules binding, storage and release;
- catalytic - substrate binding, activation, and turnover.

# *SECTION 1*

## *Natural and Artificial Heme-Proteins: Structure and Catalytic Activity*

# *CHAPTER 1.1*

## *Introduction to Natural Peroxidases*

## *1.1.1 NATURAL HEME PEROXIDASES*

Heme-proteins are an extremely important class of macromolecules, pervasive in biological systems, characterized by the prosthetic group **heme**. The heme consists of an iron ion, usually in the +2 or +3 oxidation states, coordinated by the porphyrin.

Hemoproteins are involved in a wide variety of different biological functions, spanning from electron transfer,[7,8] dioxygen transport and activation,[9] ligand sensing,[10] steroid biosynthesis,[11] photo-assisted synthesis,[12] gene expression regulation,[13] xenobiotic metabolism.[14]

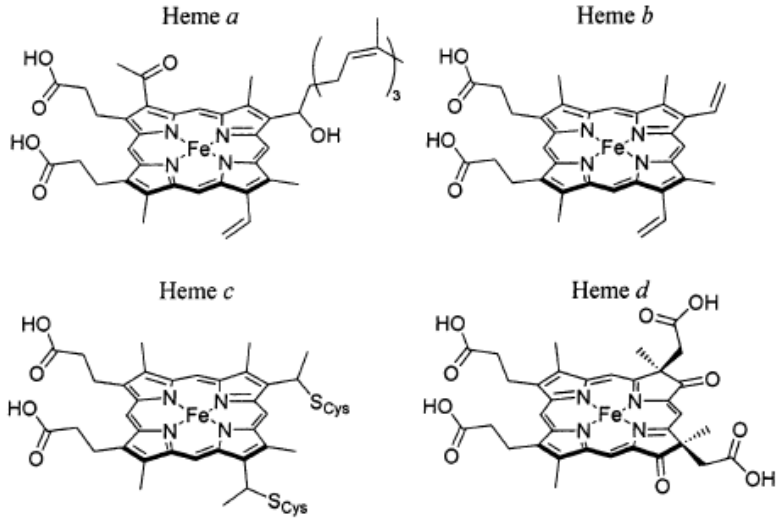


**Figure 1.1.** Chemical structures of naturally occurring hemes *a*, *b*, *c* and *d* [reproduced from ref. 12].

Heme-proteins are classified in different subcategories depending on the type of porphyrin and how it is anchored to the protein (Figure 1.1). The most common heme is iron (II) protoporphyrin IX, known as **heme *b*** or "protoheme". It presents vinyl groups

at positions 8 and 13, methyl groups at positions 3, 7, 12 and 17, and propionates at positions 2 and 18 of the porphyrin. Heme b is anchored to the protein scaffold through the combination of the axial coordinating residues to the iron ion, hydrophobic interactions with the heme macrocycle, and polar interactions with the porphyrin propionic acids.[15]

**Heme *c*** is anchored to proteins via thioether bonds between cysteine residues and the heme vinyl groups. Cytochromes *c* and *f*, in which the heme *c* is found, typically contain a CXXCH sequence motif, in which the two cysteine residues are covalently attached to the porphyrin, while the histidine coordinates the encapsulated iron.[15,16]

**Heme *a*** is synthesized from heme *b* by conversion of the vinyl group at position 8 into a hydroxy-ethylfarnesyl group, followed by oxidation of the methyl at position 3 to formyl group. Heme *a* is both more hydrophobic and more electron-withdrawing with respect to its precursor. It is found only in terminal oxidases, such as mammalian cytochrome *c* oxidase.[15,17]

Other less common heme architectures include heme *d*,[18] heme P-460,[19] siroheme,[20] and chloro-cruoroheme.[21]

The reactivity of the heme is deeply modulated by the protein matrix. Indeed, there are several classes of proteins with different catalytic functions, even though they contain the same prosthetic heme group. Protein composition and structural organization of the peptide fine-tune the environment of the heme cofactor, selecting one reaction as the only or predominant chemical transformation.[22]

Structural peptide organization, amino acid composition, protein tridimensional structure dictate the properties of the primary (metal coordination geometry, number, type and donor

properties of the axial ligands) and secondary (local dielectric constant, hydrophobicity, hydrogen bonding interactions near to the active site) coordination shells. Moreover, the protein directs long-range interactions. All these factors modulate heme-protein redox potentials, electronic structure, spin states, and catalytic properties.[22]

Different amino acids can serve as axial or proximal ligands to the heme. In a data set of non-homologous hemoproteins (Figure 1.2) histidine predominates as an axial ligand, especially in multi-heme proteins. Other residues with side chains acting as axial ligands are methionine, cysteine, and tyrosine.[23] In two cases a change in the axial ligand is observed on reduction: in CO-sensing proteins, the axial ligand Cys75 is replaced by His77 in the reduced state,[24] while in cytochrome cd1 nitrite reductase one of the axial ligands (a tyrosine residue) exits from the coordination sphere on reduction, leaving a vacant site.[25]

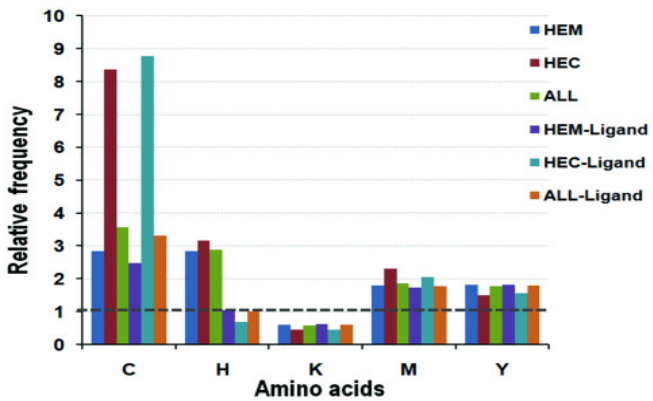


**Figure 1.2.** Occurrence of axial ligands to the heme iron ion in a data set of non-homologous heme-proteins; heme *b* (HEM), heme *c* (HEC), and heme *b* and *c* (ALL) [data taken from ref. **26**].

The coordination number five is frequently found; this is achieved by the protein scaffold that provides only one histidine

as the fifth axial ligand, while the sixth coordination position is left empty to accommodate exogenous molecules. This geometry is commonly found in globins and peroxidases. The second most common coordination motif is six-coordinated, since two His residues bind the metal ion from the opposite faces of the porphyrin ring. This coordination geometry is found, as an example, in electron carrier proteins.

In addition to His, Met and Cys frequently act as sixth axial ligands to the heme. Indeed, a typical six-coordinated ligation motif for heme-proteins consists of a His and Met (e.g. in cytochrome c)[27] or *bis*-methionine (e.g. in bacterioferritin).[28] Conversely, Cys as the axial ligand is mainly observed in five-coordinated heme-proteins, such as cytochrome P-450.[29] Other few amino acid ligands are found in six-coordinated heme-proteins in combination with His (e.g. tyrosine in cytochrome cd1 nitrite reductase).[25] In a very few structures, some residues coordinate the heme iron through their neutral N-terminal amino group, such as a tyrosine in cytochrome f and a proline in CO-sensing protein.[30]

Li *et al.* pointed out that heme binding pockets are enriched in aromatic and non-polar amino acids.[26] Through bioinformatic tools, they analyzed the occurrence of amino acid residues in a non-redundant data set of 125 heme-proteins. (Figure 1.3)

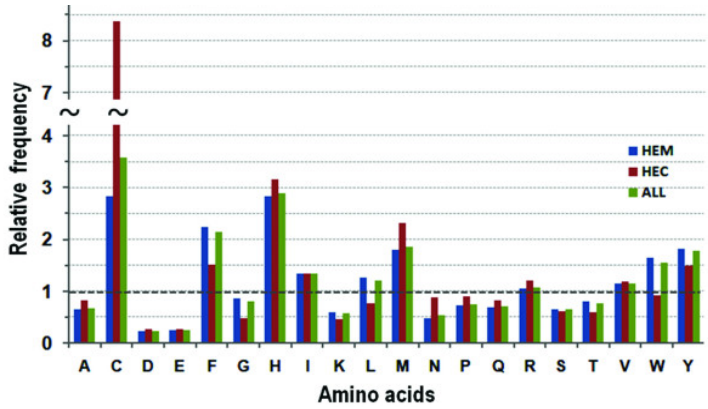


**Figure 1.3.** Relative frequency of the residues in heme *b* (HEM), heme *c* (HEC), and heme *b* and *c* (ALL) [reproduced from ref. 26].

In heme *c* proteins, the occurrence of Cys residues is very common, due to the large presence of the classic CXXCH binding motif, as mentioned above.[31]

The aromatic residues (Phe, Tyr, Trp) play important roles in protein-heme interactions through π-stacking interactions with the porphyrin. Aliphatic residues (Leu, Ile, Val) are slightly increased over the background frequencies: they make hydrophobic interactions with the heme macrocycle. The residues with the fewest occurrences (Asp, Glu, Lys) are charged residues, suggesting that the heme binding pocket is mainly placed within a hydrophobic environment.

Analyzing the heme-protein secondary structures (Figure 1.4), the dominance of α-helical structures for the three-quarters was observed (77%), although heme-proteins composed of β-sheets or mixed α/β structures are not uncommon (13% and 10%, respectively). This analysis has been performed using the CATH database, which hierarchically categorized protein structures by class, architecture, topology and homologous superfamily.[15]

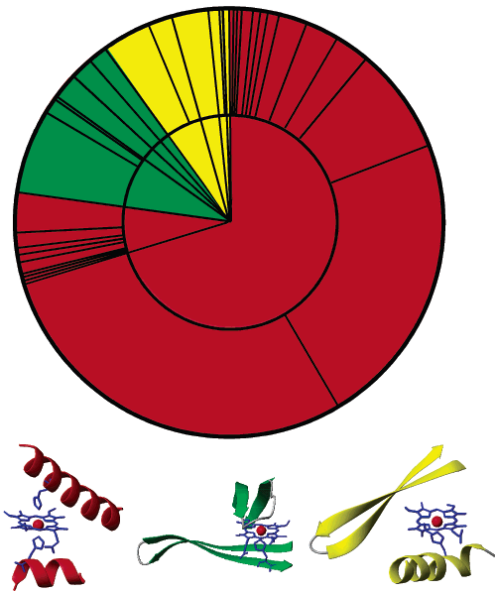

**Figure 1.4.** A CATH wheel representation of natural heme-protein secondary structures: α-helical in red, *β*-sheet in green, mixed α/*β* in yellow. At the bottom, an example for each type: myoglobin in red, nitrophorin in green, and FixL in yellow. Reproduced from ref. 15.

## *1.1.2 HORSERADISH PEROXIDASE (HRP)*

Peroxidases are a large family of ubiquitous enzymes that catalyze the oxidation of different organic and inorganic substrates, such as aromatic compounds (amine, phenols, thioanisole), using hydrogen peroxide ($H_2O_2$) as oxidizing agent. Peroxidases are widely studied enzymes, due to their relevant position in chemistry, biotechnology and medicine. All peroxidases contain $Fe^{III}$-protoporphyrin IX as the prosthetic group, except for myeloperoxidase, which contains also halides ($Cl^-$, $Br^-$, $I^-$) and pseudohalides, such as $[SCN]^-$[32]. In the resting state of the enzyme, the Fe ion is invariantly penta-coordinated: four ligands are provided by the porphyrin (four nitrogen of the heme in equatorial positions), whereas His is coordinated as the axial fifth ligand (namely, the proximal His).[33] The sixth coordination position is occupied by the solvent, thus iron is in a high spin S = 5/2 state.

As all peroxidases, HRP belongs to a large family of different enzymes, named isoenzymes, which catalyze the same reactions but they have different physical, chemical and kinetic properties, because of their small differences in amino acid sequences.

In the *Armoracia rusticana* root extract, several horseradish peroxidases have been found; among them, isoenzyme C (HRP C) is the most abundant enzyme. HRP C comprises a single polypeptide chain of 308 amino acid residues, with the N-terminal blocked by pyroglutamate and a heterogeneous C-terminus, with some molecules lacking the terminal residue (Ser308).[34] Nine potential N-glycosylation sites can be recognized in the primary sequence from the motif N-x-S/T and of these, eight are occupied. The total carbohydrate content of HRP C is

not constant and it depends on the provenance of the enzyme. Values between 18% and 22% are typically found. [35]

HRP C contains three different metallic cofactors, $Fe^{III}$-protoporphyrin IX and two calcium atoms; all of them are essential for the structural and functional integrity of the enzyme.[36]

The heme group is attached to the enzyme by a coordination bond with the $N_\varepsilon$ of histidine 170 (proximal His). The second axial coordination position on the heme distal side, is unoccupied and this represent the hydrogen peroxide binding site during catalysis.

HRP tertiary structure is composed of 13 α-helices and three β-sheets.[37] Protein conformation is stabilized by four disulfide bonds (Cys 11–91, Cys 44-49, Cys 97–301, and Cys 177–209). The protein has a quaternary structure composed of two domains, one distal and one proximal; between them, the heme group is located (Figure 1.5).

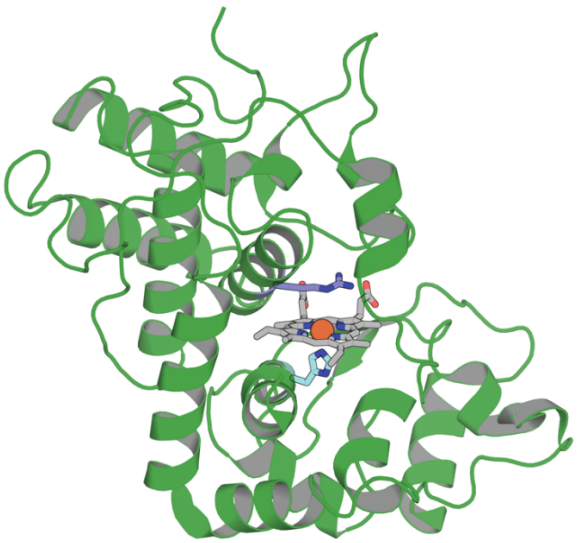

**Figure 1.5.** Three-dimensional representation of the X-ray crystal structure of HRP C (PDB entry ID: 1H57).

Most reactions catalyzed by HRP C and other horseradish peroxidase isoenzymes can be expressed by the following equation:

$$H_2O_2 + 2AH \xrightarrow{HRP} 2H_2O + 2A^{\cdot}$$

in which AH and $A^{\cdot}$ represent respectively the reducing substrates (such as phenols, aromatic acids, aniline derivate, sulfides) and its radical product.

The catalysis occurs in a three-step process, in which the enzyme is first oxidized by $H_2O_2$ and then reduced back to the resting state by two sequential steps, passing through two enzyme intermediates, Compounds I and II (Figure 1.6).[38]

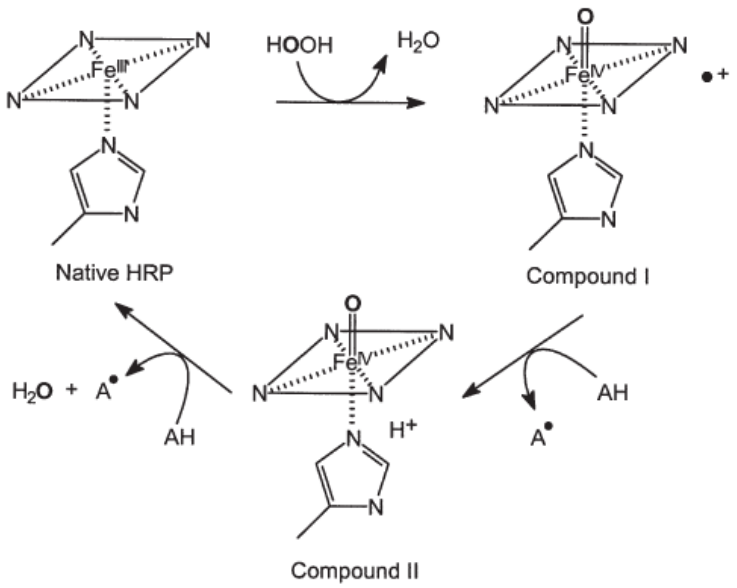


**Figure 1.6.** Catalytic cycle of HRP.

The first step consists in the cleavage of the $H_2O_2$ peroxidic bond with the concomitant release of water and the incorporation of an oxygen atom to yield Compound-I, which contains an oxoferryl group, with the iron in the +4 oxidation state, and a porphyrin in π-radical cation.

Compound-I is able to oxidize a wide range of reducing substrates. By a single-electron transfer mechanism, the compound-I π-radical cation is reduced, leading the second enzyme intermediate, called Compound-II. This still contains an oxoferryl group, which is able to oxidize a second substrate molecule, going back to the native ferric enzyme form (Fe +3). During these double one-electron reductions, the oxygen accepts two protons to form a water molecule released from the heme.

The presence of a strong hydrogen bond between the $N_\delta$ atom of the proximal histidine and an aspartate side chain (Asp247)

represents a key factor in the modulation of redox potential of the penta-coordinated complex. This hydrogen bond increases the basicity of the coordinating histidine, stabilizing the high oxidation state of the intermediates, such as the high valent oxoferryl center.[39]

Hydrogen peroxide bindings occur in the distal site, which is characterized by distal His and Arg residues (Figure 1.7). These two amino acids are invariant in all plant peroxidases and play a major role in the formation and stabilization of Compound I. Distal His (His42) acts mainly as a general acid–base catalyst: it assists the hydrogen peroxide deprotonation and the subsequent heterolytic cleavage of the peroxidic bond during Compound I formation.[40] Distal Arg 38 is involved in charge stabilization, mediated by its positively charged guanidinium group. Furthermore, once the O–O bond is cleaved, Arg contributes to stabilize the oxoferryl species via hydrogen bond formation.

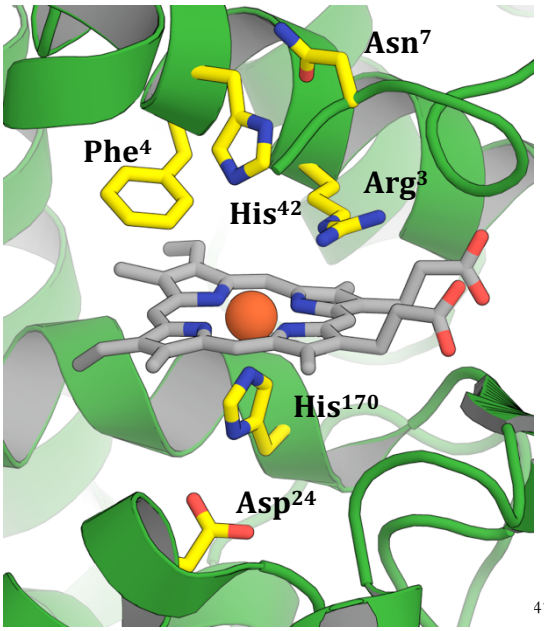


**Figure 1.7.** Proximal and distal sites of HRP (PDB entry ID: 1H57).

The replacement of these highly conserved residues causes a drastic reduction of Compound I rate formation, and therefore of HRP catalytic activity. This is a proof of their foundamental role in catalysis. Treatment of the enzyme with an excess of hydrogen peroxide provides Compound III, whose structure is best described as a resonance of $Fe^{2+}$-$O_2$ and the isoelectronic $Fe^{3+}$-$O_2^-$ form. Berglund and co-workers succeeded in obtaining a three-dimensional movie of the X-ray-driven catalytic conversion of the bound dioxygen species to two molecules of water in the active site.[42] The mechanism involves four successive, one-electron reductions with the concomitant uptake of a proton, from Compound III to the ferrous HRP, via the intermediate forms of Compound I, Compound II and ferric HRP. The high-resolution crystal structure of Compound III shows dioxygen bound to heme iron in a bent conformation.[42]

# CHAPTER 1.2

## *Introduction to Heme-Protein Models*

## *1.2.1 ARTIFICIAL METALLOENZYMES: BIOINSPIRED IRON PORPHYRINS WITH CATALYTIC POTENTIAL*

The most fundamental aspects of metal cofactor assembly and metalloprotein function have already been clarified, mainly through structural–functional studies on natural metalloproteins and related mutants.[43] Despite these progresses, several questions are still open. While the control of the functional specificity by the primary coordination sphere is well understood, the contribution of medium and long range interactions remains to be determined. Thus, it is not surprising that many efforts are being devoted to the development of metalloprotein mimics, with the aim to:

- provide further insight for structure-activity relationship (SAR) studies;
- understand the minimal requirements for function;
- reproduce the properties of the parent native proteins in smaller molecules, with improved properties, such as higher stability and greater efficiency;
- construct new, tailor-made molecules useful for biomedical, pharmaceutical and environmental applications.

Over the years, heme-protein models have been developed using quite different strategies. They differ in molecular structures, ranging from simple *meso*-substituted tetra-aryl metalloporphyrins to more complex peptide-porphyrin conjugates. A common feature in the compounds so far developed is the assembly,

around the porphyrin ring, of several different chemical components, which are intended to fulfill the features of the protein matrix and make the heme able to accomplish specific functions.

The first low molecular weight heme-protein models date back to the early 1970s. All these systems showed penta-coordination, obtained both by using hindered ligands and by covalently attaching the axial ligand to the porphyrin ring. A bulky moiety was needed to cover one face of the porphyrin ring, preventing the formation of a hexa-coordinated species.[44]The pioneering works of Traylor,[45,46], Momenteau,[47] and Reed[48] can be considered fundamental for the development of dioxygen-binding molecules. Some representative examples are constituted by the picnic-basket[49] and capped[46] porphyrin systems, where the coordination state of the iron(II) was achieved using hindered substituents on the *meso* or the pyrrole positions of a 5, 10, 15, 20-tetraphenylporphyrin. These systems can be considered as fundamental for the development of dioxygen binding molecules and have contributed to a better understanding, at a molecular level, of the properties of natural heme-proteins. Even though they displayed enhanced and interesting activity, their practical application was limited to the use in organic solvents.

Peptide-based models are fundamental in assisting our understanding of the factors governing the heme properties. They also offer the additional advantage of making the highly hydrophobic heme water-soluble, by simply accommodating the prosthetic group in a hydrophobic pocket of an amphiphilic structure. Being between small molecule models and large proteins, artificial peptide-based models are the best candidates to mimic both the structural characteristics and reactivity of natural systems. Their structures are simpler than those of natural

proteins, but they have sufficient size and chemical diversity to allow substrate recognition and to resemble the high chemo, regio, and stereoselectivity of natural hemoproteins.

The development of peptide-based models takes advantage from recent progress in both the design and the chemical synthesis of peptides and proteins. It is now possible to construct recognition and catalytic sites in a scaffold and to systematically vary the amino acid composition, allowing to (1) optimize the structural and functional properties of the initial target in terms of stability, catalytic activity and selectivity, (2) test how small changes in the sequence can affect heme properties and functions and (3) investigate the effect of variation in the first and second coordination spheres.[5,]

Microperoxidases (MPs) represent the first studied covalent heme-peptide fragments, which can be obtained by the proteolytic digestion of cytochromes *c*.' The peptide moiety is covalently linked to the heme through thioether bonds, by the Cys-$(Xaa)_2$-Cys-His motif. The amino acid sequence of the polypeptide chain in MPs is numbered according to the one of the parent cytochrome c. Selective proteolysis of cytochrome *c* affords various MPs, differing in the peptide chain length.[50] The most studied example among MPs is MP8, which is obtained from the tryptic digestion of horse heart cytochrome *c*; it retains the amino acid residues 14–21 of the starting protein. MP11 retaining residues 11–21, and MP9 retaining residues 14–22 have also been studied extensively. These MPs contain the minimal requirements for a heme-protein mimic, by retaining a His residue at position 18, which coordinates the heme iron and acts as a proximal ligand. In addition, the sixth coordination site to the heme is occupied by a water molecule, which is readily displaced by an entering exogenous ligand (Figure 1.8).

One of the most interesting features of the chemistry of MPs is that, despite their relatively small size, they are able to selectively oxidize a variety of organic substrates, including ABTS (2,2'-azino-bis(3-ethylbenzthiazoline-6-sulphonic acid)), anilines, naphthols, phenols.[51] MP11 has been shown to oxidize sulfides enantioselectively, although with only modest enantiomeric excess (ee) values (16–25%).[52]

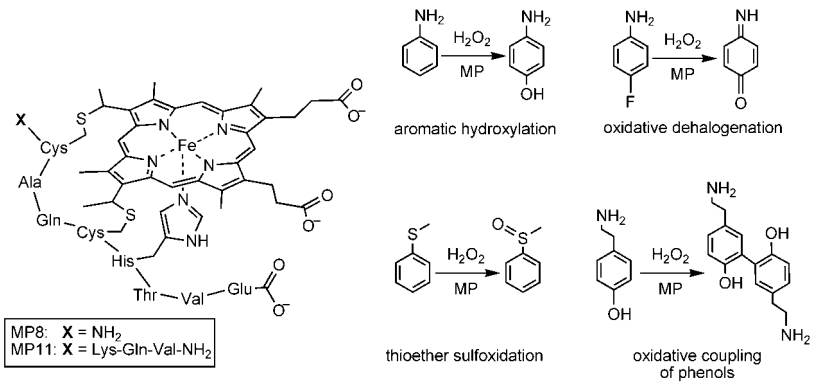


**Figure 1.8. left** Structure of Microperoxidases; **right** and some of the peroxidase and oxygenase-like reactions catalyzed by MPs.

It has been suggested that the peptide retains a conformation very similar to the amino acid residues of the parent protein. Molecular dynamics simulations of MP8 and MP11 suggests that the peptide only covers the proximal face of the porphyrin, while the distal face is totally open to the solvent.[22]

Despite their extensive use, no full atomic-resolution structure for any MP is available owing to the conformational flexibility of the peptide portion. Recently, a new MP analog, $MP9_{cb562}$, was obtained from the tryptic digestion of cytochrome cb562. The immobilization of $MP9_{cb562}$ inside a protein lattice cage allowed the first crystallographic structure determination for any member of the MP family (Figure 1.9).[53]

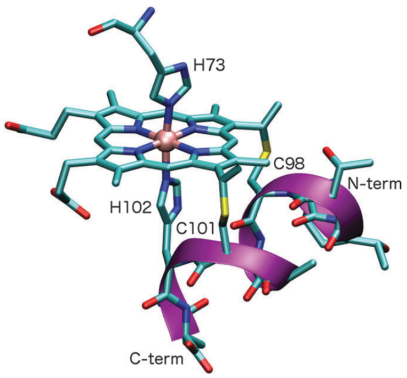


**Figure 1.9.** Crystal structure of $MP9_{cb562}$, obtained from the tryptic digestion of cytochrome cb562, and the distal position is occupied by the solvent exposed His 73 from the co-crystallized cytochrome cb562 (PDB ID: 3m4c)

The structure of $MP9_{cb562}$ reveals an α-helical peptide conformation throughout its length that is slightly more expanded than that of the corresponding segment within the holo-protein. Nevertheless, the fact that a nine-residue long fragment can adopt a helical architecture outside the context of a folded protein suggests that *c*-type linkages may provide some bias to the formation of an α-helical structure toward both N- and C-terminal ends. [9]

The application of MPs as catalysts is limited by their low stability under catalytic conditions. The accessibility of the distal side causes the degradation of the porphyrin ring during catalysis, either by the direct action of $H_2O_2$ or by intermolecular reactions with another active iron–oxo species. Despite these limitations, MPs are still much more stable than simple protoporphyrin systems, indicating that the presence of the small peptide chain can play an important protective role and make the catalyst more robust.

The use of α-helical peptides able to cage the heme group, has been and remains the focus of the most of works in the field of peptide-based models, because the α-helix motif is a recurring structural motif that surrounds the heme cofactor in numerous natural hemeproteins.[54] Over the years, a large number of helical hemeprotein models have appeared in the literature. They differ in structural complexity, and can be grouped into two classes, according to the nature of the interactions between the heme and the helical peptides: 1) models in which peptide chains are covalently linked to the heme; 2) models in which peptide chains incorporate one or more heme groups, by non-covalent self-assembling around the heme.

The four-helix bundle motif has been widely used as protein cage for mono-heme and multi-heme binding. It should be highlighted that the assembly of α-helices into the four-helix bundle motif is a ubiquitous and functionally important architecture found in several hemeproteins, such as cytochrome c and cytochrome $b_{562}$.

Excellent examples of covalent heme-peptide assemblies are the peptide sandwiched deuteroheme MP3. In a very recent paper, the construction of a *de novo* artificial heme-binding "maquette" able to efficiently catalyze oxidation reactions using $H_2O_2$ has been reported.[9,55].

MP3 has been designed by combining the excellent structural properties of four-helix bundle protein scaffolds with the activity of natural peroxidases[56] (Figure 1.10). It houses two peptide chains of different composition covalently linked the deuteroporphyrin IX through the side chain of two lysine residues, to obtain an asymmetric helix/loop/helix-heme-helix/loop/helix sandwich arrangement. MP3 is a penta-coordinated complex, characterized by: 1) a His residue on one

chain as the axial ligand to the heme iron; 2) an empty distal site, able to accommodate exogenous ligands or substrates; 3) an arginine residue in the distal site, that should assist in hydrogen peroxide activation, mimicking Arg38 in HRP.

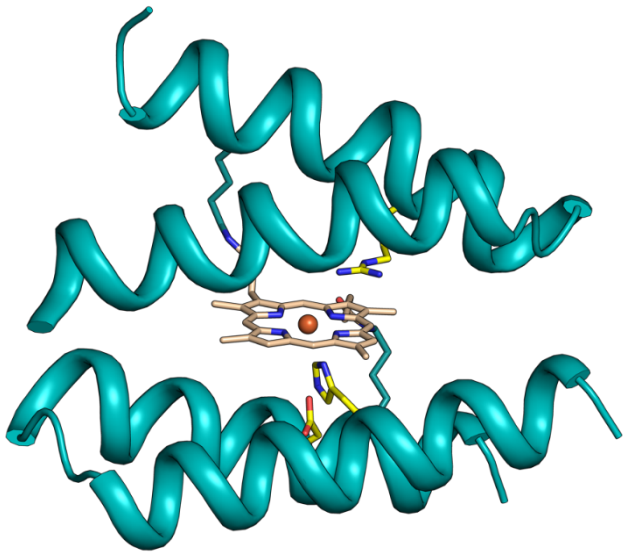

**Figure 1.10.** Computer model of MP3. Tridimensional model of MP3 side-chains of key-residues are depicted as green sticks.

MP3 was synthesized and characterized as its Fe(III) complex. CD spectroscopy suggested that MP3 scaffold possessed high intrinsic helical propensity in water, even if complete folding of the helices occurred only in the presence of TFE (2,2,2-trifluoroethanol). UV/Vis, MCD and EPR spectroscopies gave insight into the coordination geometry and spin state of the metal, confirming mono-His coordination above pH 4. MP3 showed a high catalytic turnover in the oxidation ABTS by $H_2O_2$, with a catalytic efficiency only three-fold lower than that of HRP.

The maquette approach is based on the identification of a peptide sequence able to adopt a four-helix bundle. Maquettes-simple
4-α-helix bundles designed from first principles[57] in particular provide a blank canvas for tractable and iterative design processes, as demonstrated by the successful incorporation of sophisticated functions common to oxidoreductases such as intermolecular electron transfer[57] and oxygen binding[58]. An example of four helix bundle was reported by Anderson and co. workers. In early studies, the artificial maquettes were modified by the post-translational cytochrome c maturation system of *E. Coli* enabling covalent incorporation of the heme cofactor *in vivo*, giving rise to the "c-type cytochrome maquettes" (CTMs).[59] In this case, a heme bearing a His coordination as active site was introduced through a simple and few-steps design process.[55]

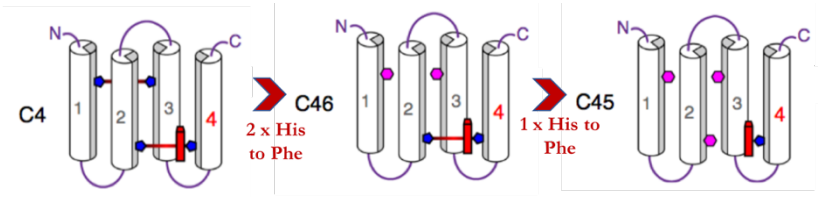


Figure 1.11: Key-steps in the developing of a catalytic c-type maquette (C45).

The resulting artificial enzyme (Figure 1.11), called C45, was endowed with very high catalytic activity regarding ABTS oxidation, even at high temperatures. Remarkably, C45 demonstrated high catalytic versatility, promoting a wide variety of oxidation reactions, including the oxidation of guaiacol, luminol, *o*-phenylenediamine, *p*-anisidine, 5-aminosalycilic acid and the oxidative dehalogenation of 2,4,6-trichlorophenol and its brominated and fluorinated congeners.

## 1.2.2 MIMOCHROMES: MINIATURIZED HEME-PROTEIN MODELS

The *Artificial Metallo-Enzyme Group* in Naples approached the challenge of constructing heme-protein models using a miniaturization process. By this strategy, a class of artificial heme-proteins has been developed, named Mimochromes.

Mimochromes are peptide-sandwiched deutero-heme systems, obtained by miniaturizing natural heme-proteins, with aim to resemble their structural and functional properties. Analyzing natural heme-protein structures, it emerges that the prosthetic group is almost completely embedded between two relatively small α-helical peptide fragments.

The natural motif helix-heme-helix was used as a template to engineer the family prototype, Mimochrome I.[60,61] To design a mini-heme protein, the copious interactions of the peptide moiety with the heme commonly found in natural proteins were replaced by a few strong local constraints. The smallest sequence required for a complete coating of one face of the heme, was identified in a nine-residue peptide, based on the F helix of hemoglobin β-chain (Figure 1.12).

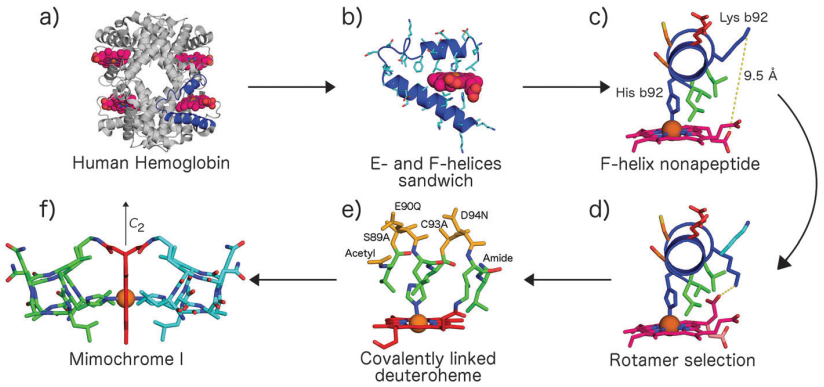


**Figure 1.12.** Miniaturization design from hemoglobin (PDB ID: 2hhb) to mimochrome I. (a and b) Active site identification and extraction. (c) Isolation of heme covering the nonapeptide. (d) Mutual approach of heme propionate towards Lys92 by proper rotamer selection. (e) Selection of solvent exposed residues and protoporphyrin IX to deuteroporphyrin mutation. (f) Symmetry-generated hexacoordinated deuteroheme. The structures were generated using PyMol.335

Mimochrome I peptide sequence contains: a central His residue to coordinate the heme iron; Leu residues at positions i-4 and i+4 relative to the His to hydrophobically interact with the heme macrocycle; a Lys residue to anchor the heme group; two alanine residues (that substitute Ser89 and Cys93), chosen for their high α-helical propensity; glutamine and asparagine residues (that substitute Glu90 and Asp94) to remove charge residues that could destabilize the target conformation (Figure 1.13).

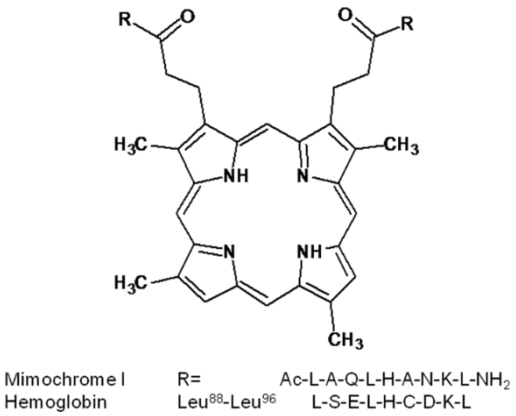


**Figure 1.13.** Schematic structure of Mimochrome I and the comparison of the peptide sequence with the L88-L96 fragment of the F helix in the β-chain of hemoglobin. Figure reproduced from ref. [61].

Deuteroporphyrin IX was preferred to the more common protoporphyrin IX to avoid the possibility of degradation of the sensitive vinyl substituents during the synthesis. Two identical copies of the peptide were covalently linked to the porphyrin propionic groups through the ε-amino function of Lys, obtaining a *pseudo*-$C_2$-symmetric dimer

The insertion of cobalt ion into the porphyrin ring gave two diastereomers. In fact, linker flexibility between the peptide and the deuteroporphyrin ring allows each peptide chain to be positioned either above or below the porphyrin plane, producing enantiomeric configurations around the metal center. The presence of the substituents on the porphyrin ring and the chirality of the peptide chain contribute to establish a diasteromeric correlation between the Δ and Λ isomers of $Co^{III}$-Mimochrome I. This finding was confirmed by structural NMR characterization of the two previously separated Co(III) complexes[62] (Figure 1.14).

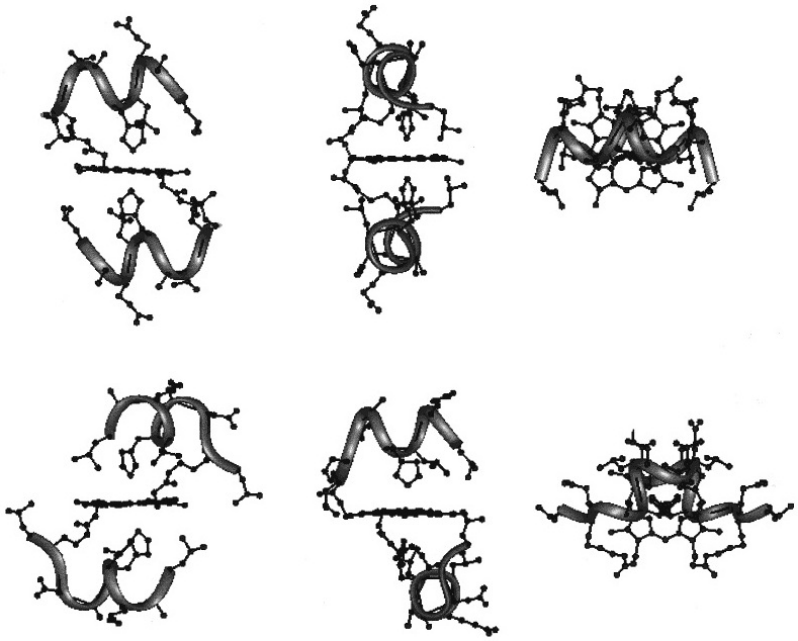

**Figure 1.14.** Front, side and top views of the average molecular structures obtained from NMR data and RMD calculations for Δ isomer (top) and Λ isomer (bottom) of Co(III)-Mimochrome I. Figure reproduced from ref. 55.

The information derived from Mimochrome I was applied for improving the design. Over the years, quite a few other models were developed, with same or different peptide chains linked to the deuteroporphyrin ring (Table 1.1).

| Mimochrome | | $R_1$, $R_2$ |
|---|---|---|
| I | $R_1=R_2$ | Ac-L-A-Q-L-H-A-N-K-$NH_2$ |
| II | $R_1=R_2$ | Ac-D-L-S-D-L-H-S-K-K-L-K-I-T-L-$NH_2$ |
| IV | $R_1=R_2$ | Ac-E-S-Q-L-H-S-N-K-R-$NH_2$ |
| III, V | $R_1$ | Ac-D-E-H-K-L-H-S-K-K-R-K-I-T-L-$NH_2$ |
| | $R_2$ | Ac-D-E-H-K-L-Y-S-K-K-R-K-I-T-L-$NH_2$ |
| VI | $R_1$ | Ac-D-E-Q-Q-L-H-S-Q-K-R-K-I-T-L-$NH_2$ |
| | $R_2$ | Ac-D-E-Q-Q-L-S-S-Q-K-R-$NH_2$ |

H= Histidine coordinating the metal center; Y= Gly or Ser
K= Lysine bound to the deuteroporphyrin

**Table 1.1.** Peptide sequences of various Mimochrome members.

Mimochrome II[63] presents two identical and elongated peptide chains, modeled in an extended conformation, whose residues were carefully chosen to improve water solubility and to stabilize a unique diastereomer.

Later, another complex with identical peptide chains was designed: Mimochrome IV.[64,65] This model considers intra-molecular inter-helical interactions, provided by an ion pair between the carboxylate side chain of a Glu residue at position 1 of one peptide chain and the guanidine group of an Arg residue at position 9 of the other peptide chain (both side chains being modelled in an appropriate extended conformation). Moreover, the helix was further stabilized by a positively charged residue (Arg) at the C-terminus and a negatively charged residue (Glu) at the N-terminus, which reduced the intensity of the helix dipole.

Mimochrome IV was the first molecule with a unique topology within the Mimochrome family. The corresponding Co(III)

complex was extensively characterized both in solution and in solid state, confirming the presence of the Λ topology (Figure 1.15). The structural characterization evidenced that in the solid-state crystal packing interactions strongly affected the molecular folding, with intra-chain Glu1–Arg9 ion pairs that were preferred over the designed, and experimentally found in solution, inter-chain interactions.

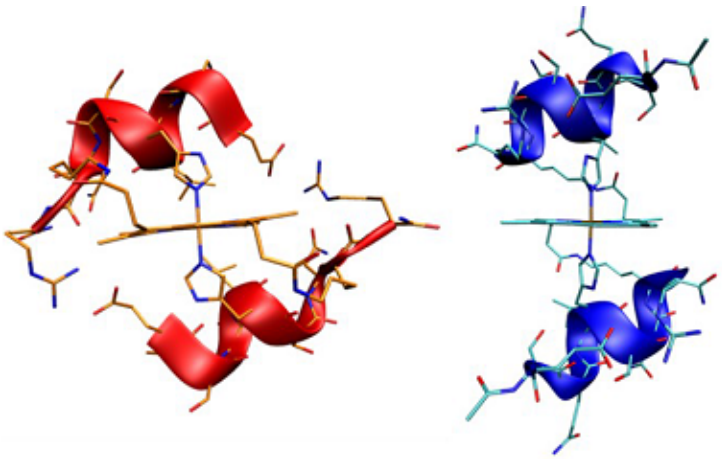

**Figure 1.15.** NMR (on the left) and X-ray (on the right) structures of Co(III)-Mimochrome IV. Figure reproduced from ref. 64.

## *1.2.3 CATALYTICALLY ACTIVE MIMOCHROMES: MC6 AND ITS CONGENERS*

Since Mimochrome IV, despite its small size, adopted a unique well-defined secondary and tertiary structure, the successive goal was to introduce peroxidase-like activity into Mimochrome's architecture, with the perspective to obtain enzyme-mimicking molecules having a higher stability and even with improved catalytic properties compared to native hemoproteins.

Among the Mimochrome family, Mimochrome VI was the first model showing catalytic potential.[66] It was composed by a 14-residue peptide, with a His residue at position 6 acting as axial ligand of the heme (proximal site) and a 10-residue peptide lacking a heme-coordinating moiety, to create a cavity around the metal ion (distal site). This unsymmetrical penta-coordinated mono-His model was designed starting from the NMR solution structures of both the symmetric *bis*-His Mimochrome II and Mimochrome IV.

The tetradecapeptide was designed to adopt a short helical conformation (residues 1-9), a loop $\gamma\beta_D$ (residues 10 and 11) and a short β-strand (residues 12-14) that folded back to interact with the helical part. The decapeptide chain also was designed to adopt a helical conformation (residues 1-8). Stabilization of the secondary structure was also given by the positively charged Arg10 and the negatively charged Glu2 at the C-terminal and N-terminal ends, respectively, with the opposite sign relative to the helix dipole (Figure 1.16).

The tertiary structure could be viewed as a sandwich, which is a characteristic trait of the Mimochrome family members, in which the two peptide chains embraced the metalloporphyrin; peptide helices were antiparallel to each other and the helix axes were conceived to be about parallel to the porphyrin plane. Stabilization of the tertiary structure was enhanced by inter-chain ion pairs between the carboxylate side chains of a glutamate residue (Glu2) on one helix and the guanidine group of an arginine residue (Arg10) on the other helix. Finally, several glutamines (Gln3, 4 and 8) and a serine (Ser7) were introduced in the solvent exposed positions to promote water solubility.

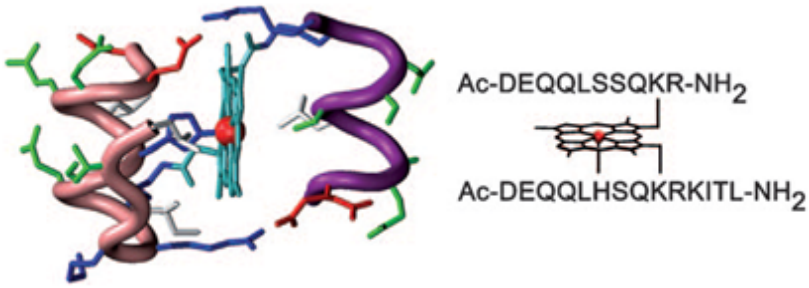


**Figure 1.16.** Molecular model and amino acid sequence of $Fe^{III}$-Mimochrome VI. Figure reproduced from ref. 65.

Catalytic activity studies showed that $Fe^{III}$-Mimochrome VI (FeMC6) acted as an artificial peroxidase, since it catalysed oxidation reactions resulting from $H_2O_2$ activation.[65]

FeMC6 showed a catalytic performance comparable to that of the natural enzyme, with a $k_{cat}$ value only 11-fold lower than that of HRP (Table 1.2).

| Enzyme | $k_{cat}\cdot10^{-2}$ ($s^{-1}$) | $K_m^{H_2O_2}$ (mM) | $K_m^{AH_2}\cdot10^{2}$ (mM) | $k_{cat}/K_m^{H_2O_2}$ ($mM^{-1}\,s^{-1}$) | $k_{cat}/K_m^{AH_2}\cdot10^{-3}$ ($mM^{-1}\,s^{-1}$) |
|---|---|---|---|---|---|
| **Mimochrome VI** | 3.7 ± 0.1 | 44 ± 2 | 8.4 ± 0.2 | 8.4 ± 0.5 | 4.4 ± 0.2 |
| **HRP** | 62 ± 1 | 0.85 ± 0.01 | 107 ± 1 | $(7.3\pm0.2)\cdot10^{3}$ | 5.8 ± 0.1 |

**Table 1.2** Catalytic parameters for the oxidation of ABTS ($AH_2$) by $H_2O_2$ activation for Mimochrome VI and HRP in the experimental conditions for maximal activity for each enzyme.

When evaluated at near neutral pH (pH 6.5), FeMC6 exhibited more than 4000 turnovers within 10 min in the ABTS oxidation. HRP worked with higher catalytic efficiency at more acidic pH (pH 4.5), this is notable if the catalyst should be used for wastewater depuration. FeMC6 also catalyzed: (a) the oxidation of guaiacol, with a $k_{cat}$ value 50-fold lower than that of HRP; (b) the conversion of phenols to 4- and 2-nitrophenol in presence of $NO_2$ and $H_2O_2$ in high yields; (c) the coupling reaction of tyrosine residues.

In the following stage of design, attention was focused on Glu2 and Arg10 in the decapeptide and tetradecapeptide chains, since both peptides were involved in finely tune the reactivity.

In Mimochrome VI design, these residues were placed at the N- and C- termini, respectively, to contribute to stabilize both secondary and tertiary structures. By individually replacing Glu2 and Arg10 on both peptide chains with a Leu residue, four analogues were obtained (Figure 1.17), which were screened for peroxidase-like activity.[67]

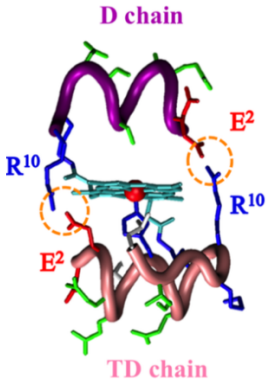


| | | |
|---|---|---|
| MC6 | Ac-D-E-Q-Q-L-H-S-Q-K-R-K-I-T-L-NH$_2$ | (*TD*) chain |
| | Ac-D-E-Q-Q-L-S-S-Q-K-R-NH$_2$ | (*D*) chain |
| E$^2$L(*TD*)-MC6 | Ac-D-L-Q-Q-L-H-S-Q-K-R-K-I-T-L-NH$_2$ | (*TD*) chain |
| | Ac-D-E-Q-Q-L-S-S-Q-K-R-NH$_2$ | (*D*) chain |
| R$^{10}$L(*TD*)-MC6 | Ac-D-E-Q-Q-L-H-S-Q-K-L-K-I-T-L-NH$_2$ | (*TD*) chain |
| | Ac-D-E-Q-Q-L-S-S-Q-K-R-NH$_2$ | (*D*) chain |
| E$^2$L(*D*)-MC6 | Ac-D-E-Q-Q-L-H-S-Q-K-R-K-I-T-L-NH$_2$ | (*TD*) chain |
| | Ac-D-L-Q-Q-L-S-S-Q-K-R-NH$_2$ | (*D*) chain |
| R$^{10}$L(*D*)-MC6 | Ac-D-E-Q-Q-L-H-S-Q-K-R-K-I-T-L-NH$_2$ | (*TD*) chain |
| | Ac-D-E-Q-Q-L-S-S-Q-K-L-NH$_2$ | (*D*) chain |

**Figure 1.17.** Left: molecular model of Fe$^{III}$-Mimochrome VI, highlighting the R$^{10}$-E$^2$ ion pair interactions. Right: peptide sequences of Fe$^{III}$-Mimochrome VI (MC6) and its analogues: acid, basic and non-polar residues in position 2 and 10 are indicated in red, blue and green, respectively. Image reproduced from ref. 66.

The apparent catalytic constant of the analogues substituted on the tetradeca chain was about 2-fold higher with respect to MC6. The best performances were obtained for E2L(*TD*)-MC6, which displayed an improvement in the apparent catalytic constant ($k_{cat}$ = $7.8 \cdot 10^2$ $s^{-1}$), and catalytic efficiency towards both $H_2O_2$ and ABTS ($k_{cat}/K_m$ = 25 $mM^{-1}$ $s^{-1}$, and $16 \cdot 10^3$ $mM^{-1}$ $s^{-1}$, respectively). In contrast, analogues with an altered decapeptide chain showed an almost unmodified reactivity compared with MC6, the worst catalyst being the E2L(*D*)-MC6 congener. All MC6 members could perform thousands of turnovers, without bleaching. The turnover numbers (T.O.N.) reflected the trend of the catalytic efficiency, being higher in E2L(*TD*)-MC6 and lower in R10L(*TD*)-MC6 (Table 1.3).

| Enzyme | pH | $H_2O_2$ | ABTS | | $H_2O_2$ | ABTS | |
|---|---|---|---|---|---|---|---|
| | | $K_m$ (mM) | $K_m$ $10^2$ (mM) | $k_{cat}$ $10^{-2}$ ($s^{-1}$) | $k_{cat}/K_m$ (mM $s^{-1}$) | $k_{cat}/K_m$ $10^{-3}$ (mM $s^{-1}$) | T.O.N. $10^{-3}$ |
| MC6 | 6.5 | 44 ± 2 | 8.4 ± 0.2 | 3.7 ± 0.1 | 8.4 ± 0.6 | 4.4 ± 0.2 | 4.0 |
| $E^2$L(*TD*)-MC6 | 6.5 | 31 ± 2 | 5.0 ± 0.4 | 7.8 ± 0.6 | 25 ± 3 | 16 ± 2 | 5.9 |
| $R^{10}$L(*TD*)-MC6 | 6.5 | 54 ± 2 | 3.8 ± 0.1 | 6.8 ± 0.3 | 13 ± 1 | 18 ± 1 | 5.6 |
| $E^2$L(*D*)-MC6 | 6.5 | 96 ± 7 | 11 ± 1 | 3.8 ± 0.3 | 4.0 ± 0.6 | 3.4 ± 0.6 | 3.6 |
| $R^{10}$L(*D*)-MC6 | 6.5 | 18 ± 1 | 3.0 ± 0.2 | 1.7 ± 0.1 | 9 ± 1 | 5.7 ± 0.7 | 3.3 |

**Table 1.3** Steady-state kinetic parameters for $Fe^{III}$-Mimochrome VI (MC6) and its analogues (reproduced from ref. 66).

A detailed spectroscopic characterization allowed to hypothesize the catalytic role of Arg10 on the decapeptide chain. Arg10 was suggested to approach the heme, contributing to the stabilization of compound I and assisting ligand binding, similarly to the conserved distal arginine (Arg38) in HRP. Indeed, there is experimental evidence that the catalytic cycle of E2L(*TD*)-MC6 occurred with a peroxidase-like mechanism, through the formation of compound I, proving its similarity with natural peroxidases, whose reactivity is influenced by the proximal and distal heme environments.[66]

# *CHAPTER 1.3*

## *A Novel Artificial Metalloprotein with Peroxidase-Like Activity*

## 1.3.1 DESIGN AND SYNTHESIS OF $Fe^{III}$-MC6a

Based on literature data discussed in Chapter 1.1 and 1.2, one of the focus of this PhD project has been the development of a novel artificial enzyme belonging to the Mimochrome family (Mimochrome VIa or MC6a; Figure 1.18).

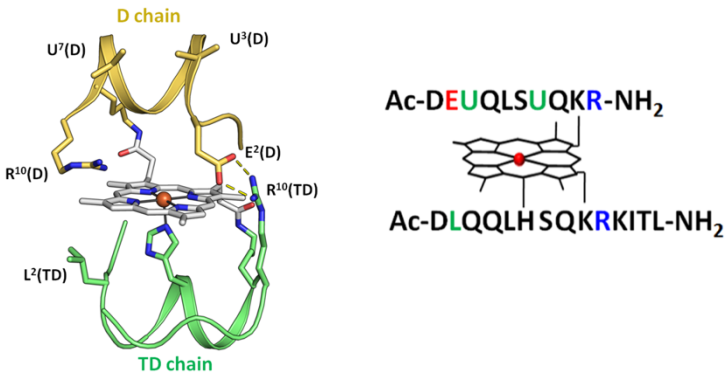


**Figure 1.18.** Schematic representation of $Fe^{III}$-MC6a.

The newly developed Mimochrome has been designed to introduce some new structural constraints, with the aim to stabilize the three-dimensional sandwich structure, typical of Mimochromes, while preserving or even enhancing its functional features. In the previous $Fe^{III}$-Mimochrome VI ($Fe^{III}$-MC6), the catalytic performance of the enzyme was demonstrated to be modulated by mutating even one single residue at the N- or C-terminus on either the tetradecapeptide (*TD*) or the decapeptide (*D*) chain.[66] In particular, the substitution of a glutamic acid with a leucine on the *TD* chain to give ($E^2L$(*TD*)-MC6) doubles the $k_{cat}$ and quadruples the catalytic efficiency ($k_{cat}/K_M$), by allowing the arginine residue on the *D* chain to assist the catalysis as

observed in natural peroxidases. $Fe^{III}$-MC6 showed a compact structure that allowed accomplishing several thousands of turnovers in water without bleaching. Moreover, the *D* chain was observed to provide a major contribution to chemical stability by protecting the high-valence intermediate. Indeed, a lower number of turnovers (TON) has been observed with the compound lacking the *D* chain. Accordingly, during this PhD thesis we studied the relationship between the rigidity of the *D* chain as well as its hydrophobicity, catalyst robustness and catalytic efficiency, as resulting by introducing two 2-amino isobutyric acid (Aib, U) residues at positions 4 and 9. Aib is a natural, non-coded amino acid, with a high helical propensity, commonly found in peptides produced by microbes.[68] The replacement of hydrogen atoms with two methyl groups at Cα of the glycine produces severe restrictions on its conformational freedom: for Aib-containing peptides, the formation of α-helix secondary structures is strongly favored. Moreover, the equilibrium between the α-helix and $3_{10}$-helix in Aib-containing peptides has been observed to be dependent on several parameters, mainly including the peptide length and the Aib content.[69]

In order to find the best positions for Aib mutation in the (*D*) sequence, a search based on the helix propensity was performed.[70] Five positions were excluded from this search: (1) $Asp^1$ at the N-terminus; (2) $Glu^2$ and $Arg^{10}$ for their established contribution to catalysis;[1] (3) $Ser^6$ as it corresponds to the active site cleft; (4) $Lys^9$ because it is involved in the covalent binding with the porphyrin. Four out of eight possible sequences gave the best score (Table 1.4). The sequence containing $Q^3U$ and $S^7U$ was selected for synthesis and characterization. Indeed, according to our model, in the new compound both Aib residues face towards the porphyrin, offering a tiny hydrophobic patch for the substrate binding.

**Table 1.4.** Energy in Kcal/mol of the possible sequences for the new Decapeptide chain.

| | Sequence | ΔΔG values (kcal/mol) * |
|---|---|---|
| 1 | DEQQLSSQKR | -4.06 |
| 2 | DEUQUSSQKR | -4.49 |
| 3 | DEUQLSUQKR | -4.76 |
| 4 | DEUQLSSUKR | -4.78 |
| 5 | DEQULSUQKR | -4.76 |
| 6 | DEQULSSUKR | -4.78 |
| 7 | DEQQUSUQKR | -4.47 |
| 8 | DEQQUSSUKR | -4.49 |

The amino acid sequence of the full protected decapeptide chain was therefore:

**Ac-Asp$^{1}$(tBuO)-Glu$^{2}$(OtBu)-Aib$^{3}$-Gln$^{4}$(Trt)-Leu$^{5}$-Ser$^{6}$(tBu)-Aib$^{7}$-Gln$^{8}$(Trt)- Lys$^{9}$(Mmt)-Arg$^{10}$(Pbf)-NH$_2$**

The amino acid sequence of the full protected tetradecapeptide chain was:

**Ac-Asp$^{1}$(tBuO)-Leu$^{2}$-Gln$^{3}$(Trt)-Gln$^{4}$(Trt)-Leu$^{5}$-His$^{6}$(Trt)-Ser$^{7}$(tBu)-Gln$^{8}$(Trt)-Lys$^{9}$(Mmt)-Arg$^{10}$(Pbf)-Lys(Boc)$^{11}$-Ile$^{12}$-Thr(tBu)$^{13}$-Leu$^{14}$-NH$_2$**

The synthesis of Fe$^{III}$-MC6a was carried out according to the following Scheme 1.

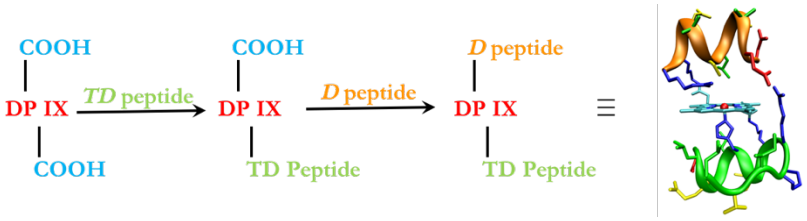


**Scheme 1.** Schematic representation of the synthetic strategy.

In line with the synthesis of previous catalysts,[67] Mimochrome VIa was first prepared on a small scale (20 μmol). An automated peptide synthesizer was used for the synthesis of the two peptides chains. The coupling steps of the peptides to the porphyrin and the final deprotection were performed in solution. Subsequently, the synthesis was applied to a medium scale (20 mmol), using (as the only exception between the two procedures) a medium size reactor for solid-phase synthesis during peptide assembly. In both cases, peptide synthesis was performed using 9-fluorenylmethoxycarbonyl (Fmoc) chemistry, using a super acid labile resin. Regarding the two Lys residues involved in amide bond with porphyrin, ((4-methoxyphenyl)diphenylmethyl (Mmt) was chosen as the protecting group. Mmt was easily removed under mild acid conditions,[71] leaving all the remaining protecting groups unreacted.

Once the synthesis was completed, a small amount of peptidyl-resin was fully deprotected and the product was analyzed by TANDEM mass spectrometry coupled to liquid chromatography. A single peak, corresponding to the desired peptide, was found and its product ion scan showed the expected transitions (Table 1.5 and 1.6).

**Table 1.5.** Mass table of Decapeptide fragmentation. Green numbers represent the theoretical fragments found.

| # | Immon. | b | $b^{++}$ | $b^{+++}$ | Seq. | y | $y^{++}$ | $y^{+++}$ | # |
|---|---|---|---|---|---|---|---|---|---|
| **1** | 88.10 | | | | **D** | 1215.34 | **608.17** | 405.78 | **10** |
| **2** | 102.13 | **287.25** | 144.13 | 96.42 | **E** | 1058.21 | 529.61 | 353.41 | **9** |
| **3** | 58.12 | ***372.32*** | 186.68 | 124.79 | **U** | **929.10** | 465.05 | 310.37 | **8** |
| **4** | 101.14 | ***500.48*** | 250.74 | 167.50 | **Q** | **843.99** | 422.50 | 282.00 | **7** |
| **5** | 86.17 | **613.64** | **307.32** | 205.22 | **L** | **715.86** | 358.44 | 239.29 | **6** |
| **6** | 60.09 | 700.71 | 350.86 | 234.24 | **S** | **602.71** | **301.86** | 201.57 | **5** |
| **7** | 58.12 | 785.82 | 393.41 | 262.61 | **U** | 515.63 | 258.32 | 172.55 | **4** |
| **8** | 101.14 | 913.95 | 457.48 | 305.32 | **Q** | ***430.52*** | 215.77 | 144.18 | **3** |
| **9** | 101.19 | 1042.12 | 521.56 | 348.05 | **K** | **302.40** | 151.70 | 101.47 | **2** |
| **10** | 129.20 | | | | **R** | | | | **1** |

**Table 1.6.** Mass table of Tetradecapeptide fragmentation.

| # | Immon. | b | $b^{++}$ | $b^{+++}$ | Seq. | y | $y^{++}$ | $y^{+++}$ | # |
|---|---|---|---|---|---|---|---|---|---|
| **1** | 88.04 | | | | **D** | 1749.01 | 875.01 | **583.68** | **14** |
| **2** | 86.10 | **271.13** | 136.07 | 91.05 | **L** | 1591.97 | **796.49** | ***531.33*** | **13** |
| **3** | 101.07 | ***399.19*** | **200.10** | 133.73 | **Q** | 1478.89 | **739.95** | 493.64 | **12** |
| **4** | 101.07 | ***527.25*** | 264.13 | 176.42 | **Q** | 1350.83 | **675.92** | 450.95 | **11** |
| **5** | 86.10 | 640.33 | ***320.67*** | **214.12** | **L** | 1222.77 | **611.89** | 408.26 | **10** |
| **6** | 110.07 | 777.39 | 389.20 | 259.80 | **H** | **1109.69** | **555.35** | 370.57 | **9** |
| **7** | 60.04 | 864.42 | 432.71 | **288.81** | **S** | **972.63** | **486.82** | 324.88 | **8** |
| **8** | 101.07 | 992.48 | 496.74 | 331.50 | **Q** | **885.60** | 443.30 | 295.87 | **7** |
| **9** | 101.11 | ***1120.58*** | 560.79 | 374.20 | **K** | **757.54** | ***379.27*** | ***253.18*** | **6** |
| **10** | 129.11 | 1276.68 | 638.84 | 426.23 | **R** | **629.45** | 315.23 | 210.49 | **5** |
| **11** | 101.11 | 1404.77 | ***702.89*** | 468.93 | **K** | **473.34** | 237.18 | 158.45 | **4** |
| **12** | 86.10 | 1517.86 | 759.43 | ***506.62*** | **I** | 345.25 | 173.13 | 115.75 | **3** |
| **13** | 74.06 | 1618.90 | 809.96 | 540.31 | **T** | **232.17** | 116.59 | 78.06 | **2** |
| **14** | 86.10 | | | | **L** | 131.12 | | | **1** |

The protected *TD* chain was first coupled to the deuteroporphyrin. To direct the (*TD*) peptide coupling toward the *mono*-substituted product (*TD*-DPIX) and to overcome the undesired *homo di*-substituted product (*TD*-DPIX-*TD*), the tetradecapeptide chain was slowly added to an excess of deuteroporphyrin IX, the reaction was monitored by HPLC (Figure 1.19). The chromatogram shows the presence of a main peak at 29.36 min, corresponding to the desired product, and two minor peaks: one corresponding to the homo di adduct ($R_t$ 30.67 min), the second one ($R_t$ 27.14 min) was not characterize. Once the complete consumption of *TD* chian was confirmed, the crude

was purified by direct phase flash chromatography on silica gel, to remove the excess of DPIX and avoid side coupling in the following steps.

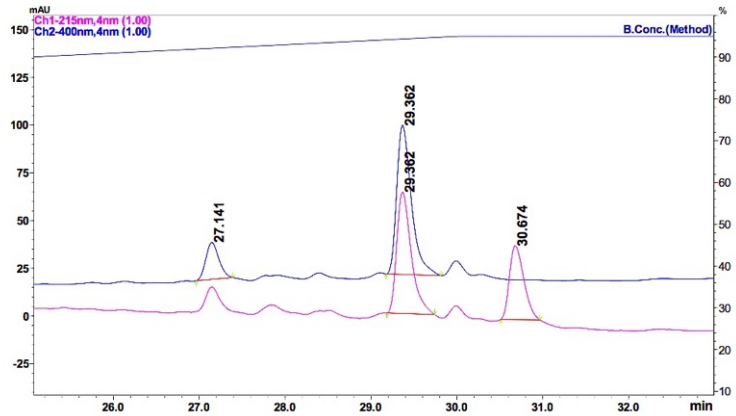


**Figure 1.19.** Overlapped HPLC profiles of the *mono*-substituted product acquired at 400 nm (blue curve) and 215 nm (pink curve). The main product with $R_t$ 29.4 min was the *mono*-substituted TD-DPIX.

The *mono*-substituted TD-DPIX was then coupled with the decapeptide chain following the same coupling condition. Once obtained the protected *apo*-MC6a, it was completely deprotected and characterized by LC-ESI-MS. The HPLC peak with $R_t$ of 26.760 min was correlated to a mass peak of $m/z$ 1147.00 ($[M+3H]^{3+}$) and 860.55 ($[M+4H]^{4+}$), which were consistent with the theoretical mass of $m/z$ 3438.30 ($[M+H]^{+}$) (Figures 1.20 and 1.21).

*Apo*-Mimochrome VIa was purified by preparative RP HPLC to yield the pure product. Coupling of the peptides to the deuteroporphyrin IX was accomplished on a 2 mmol scale, resulting in ~900 mg (0.26 mmol) of the purified free base.

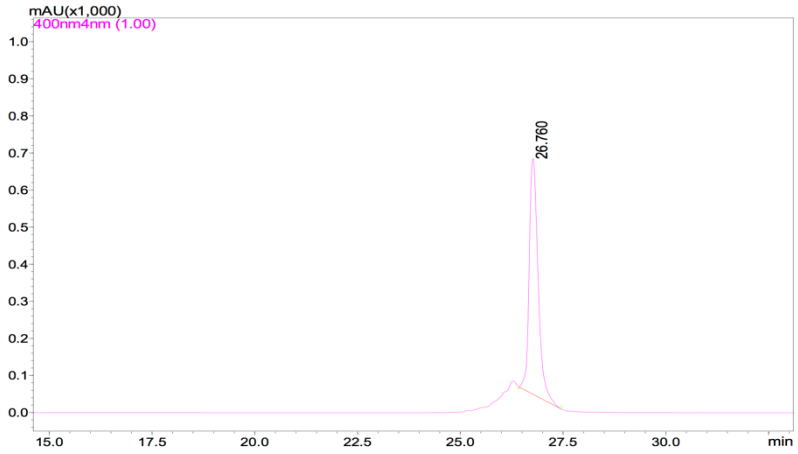


**Figure 1.20.** HPLC profile of the *apo*-MC6a after full deprotection, acquired at 400 nm $R_t$ of *apo*-MC6a was 26.760 min.

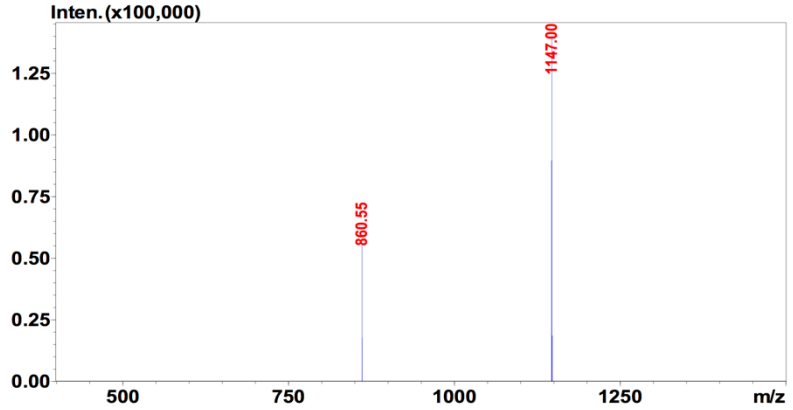


**Figure 1.21.** ESI-MS of the peak with $R_t$ = 26.760 min. The two masses at *m/z* 860.55 and 1147.00 represent respectively the $[M+4H]^{4+}$ and the $[M+3H]^{3+}$ of 3438.30 Da.

## *1.3.2 SYNTHESIS AND SPECTROSCOPIC ANALYSIS OF $Fe^{III}$-MC6a*

Iron ion was inserted in *apo*-MC6a, following the acetate method.[60] The HPLC-MS profiles regarding metal insertion are reported in Figures 1.22 and 1.23.

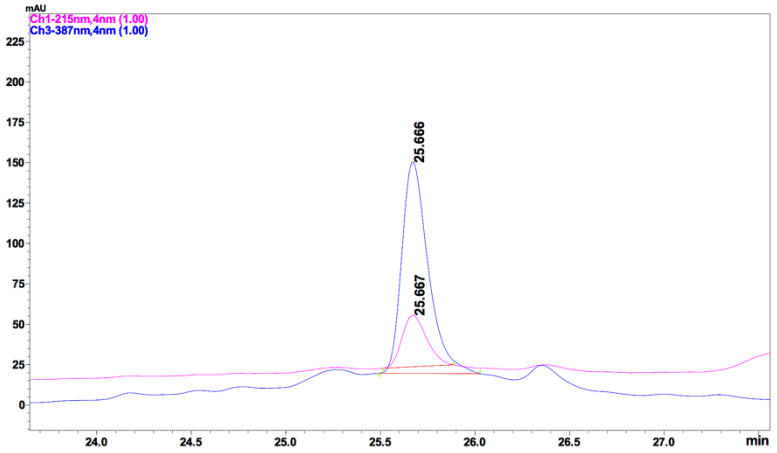


**Figure 1.22.** HPLC profile concerning the insertion of iron ion, acquired at 387 nm (blue curve) and 215 nm (pink curve). $R_t$ for $Fe^{III}$-MC6a was 25.7 min.

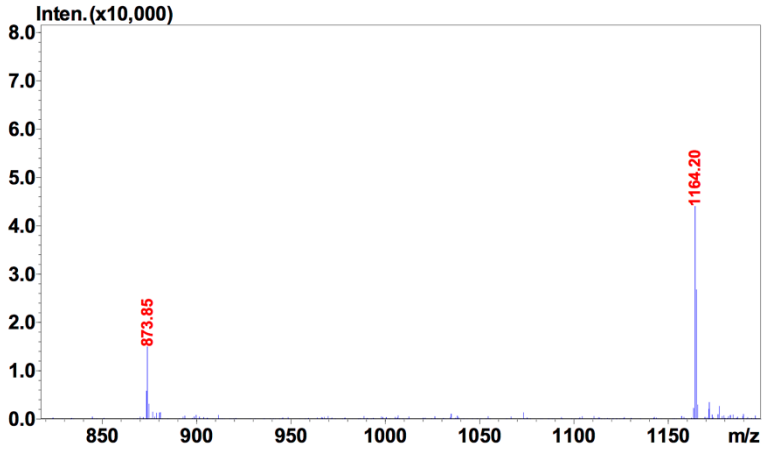


**Figure 1.23.** ESI-MS analysis of the compound at $R_t$ = 25.7 min. The observed masses at *873.85 m/z and 1164.20 m/z* correspond respectively to $[M+4H]^{4+}$ and the $[M+3H]^{3+}$, while the final product has an exact mass of 3489.6 Da $[M+H]^{+}$.

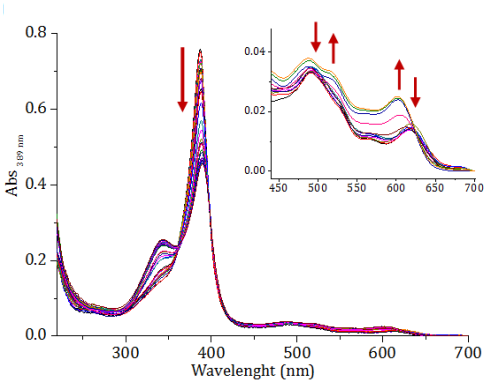


**Figure 1.24.** UV-Vis spectra of $Fe^{III}$-MC6a, pH 2 to pH 9. The red arrows summarize the change in the Soret region and in the Q bands, due to the change in the coordination sphere.

UV-vis analysis at acidic pH revealed a shift of the Soret band due to iron insertion, from 400 nm to 387 nm, while the bands in the visible region were positioned at 494 nm and 610 nm. The spectrum was consistent with a hexacoordinated high-spin

species; the His residue, at acidic pH value, was protonated and the iron was coordinated by two weak axial ligands (two water molecules) (Figure 1.24). [66,72]

To explore the coordination properties, UV-Vis titration was also performed, following the absorbance of the Soret band at 387 nm in the pH range from 2.0 to 9.0 in a mixture of $H_2O$/TFE 50/50 (v/v). pH titration studies were performed by using concentrated solutions of trifluoroacetic acid (TFA) and sodium hydroxide (NaOH), in a 1.0 cm path length cuvette. Plot of absorbance as a function of pH provided Figure 1.25, in which three distinct species were found, based on Soret band shift. Data points were fitted using an equation describing the protonation state of the species involved in the pH-dependent equilibria[67] (Equation 1.1).

$$Abs_{tot} = \frac{\left(Abs_3 + Abs_2 \cdot \frac{[H^+]}{K_{a2}} + Abs_1 \cdot \frac{[H^+]^2}{K_{a1} \cdot K_{a2}}\right)}{\left(1 + \frac{[H^+]}{K_{a2}} + \frac{[H^+]^2}{K_{a1} \cdot K_{a2}}\right)}$$

**Equation 1.1**

where $\mathbf{Abs_{tot}}$ represents the observed absorbance for the Soret band at 387 nm, while $\mathbf{Abs_1}$, $\mathbf{Abs_2}$ and $\mathbf{Abs_3}$ are the specific absorbances of *bis*-$H_2O$, His/$H_2O$, His/$OH^-$ species respectively. $\mathbf{K_{a1}}$ and $\mathbf{K_{a2}}$ are the equilibrium constants relating the mentioned species.

The best fit gave two transitions with mid-points at pH values ≈ 4 and ≈ 7. The determination of $pK_a$ values in the pH range 2.0-5.0 was not possible, because at pH 2.0 the *plateau* was still not reached (Figure 1.25). The spectrum at this pH value can be

considered as a mixture of *bis*-$H_2O$ and His/$H_2O$ ferric complexes. Increasing pH values from 2.0 to 6.6, a decrease in the intensity of the Soret band was observed, along with a slight red shift.

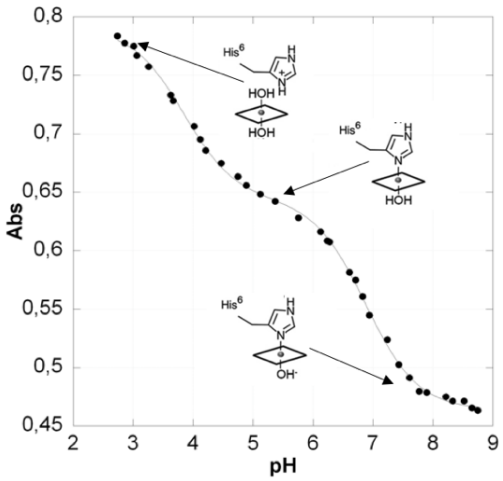


**Figure 1.25.** Plot of Abs at 387 nm versus pH. The black line represents the data point fitting, using the equation reported in ref. 66.

At pH values higher than 6.6, the maximum of the Soret band absorbance shifts from 387 to 391 nm, while the bands in the visible region move from 494 nm to 486 nm (β band) and from 610 to 601 nm (CT band). Furthermore, the band near 350 nm (N band region) broadens and its relative intensity with respect to that of the Soret band changes. These spectral modifications are consistent with changes in the ferric ion axial coordination *bis*-$H_2O$ to His/$H_2O$, in the high spin state.[50] At pH around 8.0, the Soret band shifts to 389 nm, the Q band is observed as a shoulder at 514 nm; the main bands at 487 and 600 nm are attributed to the CT bands of the mainly high-spin ferric hydroxide complex. These spectroscopic features suggest that the

transition with midpoint at pH 6.93 corresponds to a ligand exchange from $H_2O$ to $OH^-$.[73]

## 1.3.3 CD CHARACTERIZATION OF $Fe^{III}$-MC6a

Circular Dichroism (CD) in far-UV region was carried out to obtain information on the peptide secondary structure. Particularly, CD spectroscopy was used to ascertain whether Aib mutations altered $Fe^{III}$-MC6a structural features with respect to its predecessors. Figure 1.26 reports the overlay of the CD spectra of $Fe^{III}$-MC6a, in phosphate buffer (10 mM) pH 6.5 at various TFE concentrations starting from zero up to 50% (v/v).

The CD spectra of $Fe^{III}$-MC6a in absence of TFE presented two negative bands at 203 and 222 nm, and a positive band around 190 nm, indicative of α-helix secondary structure. In the absence of TFE, the molar residue ellipticity suggested that the peptide chain, even with Aib mutations, presents a low helical content. Unexpectedly, Aib mutations did not induce a strong increase in structured content.

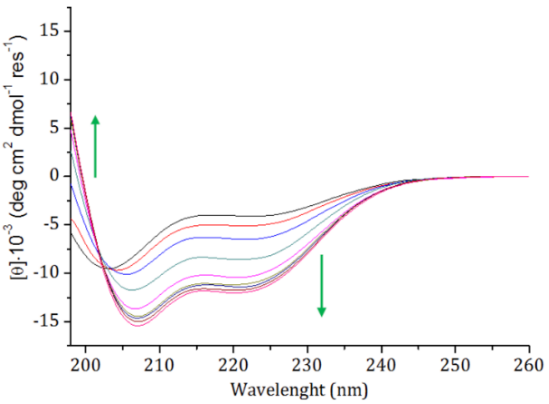


**Figure 1.26.** CD spectra in far UV region of 10 μM of $Fe^{III}$-MC6a in 50 mM phosphate butter (pH 6.5), at increasing TFE concentrations (v/v). The green arrow describes the curves changing during the TFE titration.

CD spectra in far-UV region were then acquired at increasing TFE concentrations (Figure 1.27) in order to study the conformational changes of peptide chain upon TFE addition. The following feature, indicative of peptide folding, can be observed:

- the wavelength of the minimum ($\lambda_{min}$) shifted from 202 nm to 207 nm;

- the decrease of 222 nm ($\theta_{222}$) ellipticity;

- [θ]ratio ($\lambda_{222}/\lambda_{min}$) increased from 0.42 to 0.77;

- $\lambda_0$ shifted from 194.2 to 199.4 nm.

Moreover, an isodichroic point was observed at 201.8 nm, confirming a transition from random coil to a α-helical conformation. The plot of $\theta_{222}$ value as function of TFE concentration showed a saturation behavior starting from 30% (v/v) of TFE (Figure 1.27). These data are in agreement with the previous $E^2L(TD)$-MC6 analogue.[67]

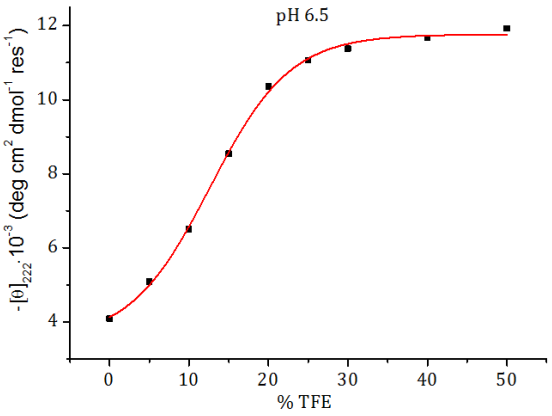


**Figure 1.27.** Plot of $\theta_{222}$ as a function of TFE concentration.

Indeed, CD spectra in the far-UV region did not highlight any significant difference between the two Mimochrome analogues, in terms of secondary structure (Figure 1.28).

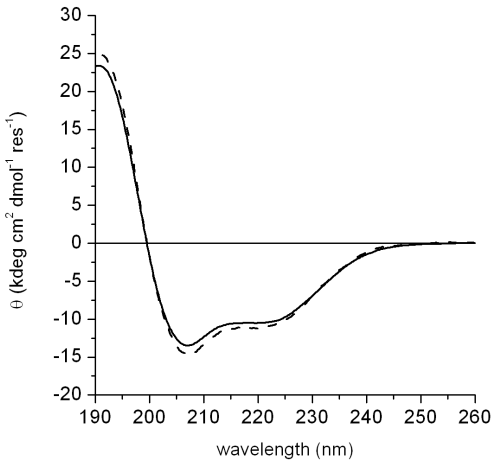


**Figure 1.28.** Comparison of far UV region CD spectra of $Fe^{III}$-MC6a (solid) and $Fe^{III}$-$E^2L$(TD)-MC6 (dashed) in phosphate buffer containing a 50% TFE (v/v) (pH 6.5).

These results led to the conclusion that Aib mutations did not significantly alter the overall secondary arrangement of the newly synthesized analogue.

## 1.3.4 PEROXIDASE-LIKE ACTIVITY OF $Fe^{III}$-MC6a

The peroxidase-like activity of the newly developed $Fe^{III}$-MC6a was evaluated towards the reducing substrate ABTS (2,2'-azino-*bis*-(3-ethylbenzthiazoline-6-sulphonic acid)), which was chosen as model substrate (Figure 1.29). ABTS is easily oxidized in the mono cationic radical form ($ABTS^{+\cdot}$), exhibiting a brilliant green color and therefore its oxidation can be easily detected by a spectrophotometric analysis of the reaction mixture.[74]

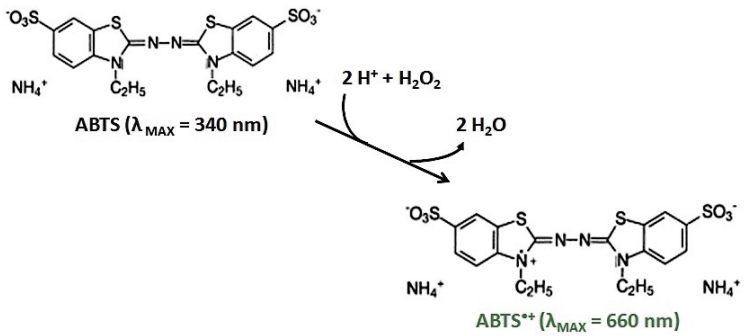


**Figure 1.29.** 2,2'-Azino-*bis*-(3-ethylbenzthiazoline-6-sulphonic acid) (ABTS) and its oxidation product ($ABTS^{+\cdot}$) mediated by $H_2O_2$.

For an accurate determination of the kinetic parameters, the catalysis was performed by stopped flow analysis. Data were fitted with a two substrates Michaelis-Menten kinetic equation (Equation 1.2):

$$v = \frac{[Eo]}{\frac{1}{k_{cat}} + \frac{K_m^A}{k_{cat}[A]} + \frac{K_m^B}{k_{cat}[B]}}$$

**Equation 1.2**.

where:

- $[E]_0$ is the enzyme concentration at the initial time ($t_0$), which is supposed to be constant and not inactivated;
- $k_{cat}$ is the catalytic constant and denotes the maximum number of enzymatic reactions catalysed *per* second;
- [A] and [B] represent ABTS and $H_2O_2$ concentrations, respectively;
- $K_m^A$ and $K_m^B$ are the Michaelis-Menten constants for ABTS and $H_2O_2$, respectively. The Michaelis-Menten constant is the substrate concentration at which the reaction rate is a half of $v_{max}$ and represents the enzyme apparent affinity for the substrate;

The analysis of the experimental kinetic data by Michaelis-Menten fitting provides the catalytic parameters dealing with $k_{cat}$, $K_M^{ABTS}$ and $K_M^{H_2O_2}$. In addition, the catalytic efficiency of the enzyme, calculated as the ratios $k_{cat}/K_m^{ABTS}$ and $k_{cat}/K_m^{H_2O_2}$, were also measured. In all experiments, concentration of $Fe^{III}$-MC6a was fixed at 2.0 $10^{-8}$ M. To determine the Michaelis constant, the experiments were carried out with an excess of one the two substrates, for hydrogen peroxide ($K_M^{H_2O_2}$) ABTS concentration was fixed at 2 mM while $H_2O_2$ was varied from 0 to 900 mM (Figure 1.30 right side). Analogously, for the determination of $K_M^{ABTS}$, $H_2O_2$ concentration was fixed at 450 mM while ABTS concentration was varied from 0 to 0.3 mM (Figure 1.30 left side).

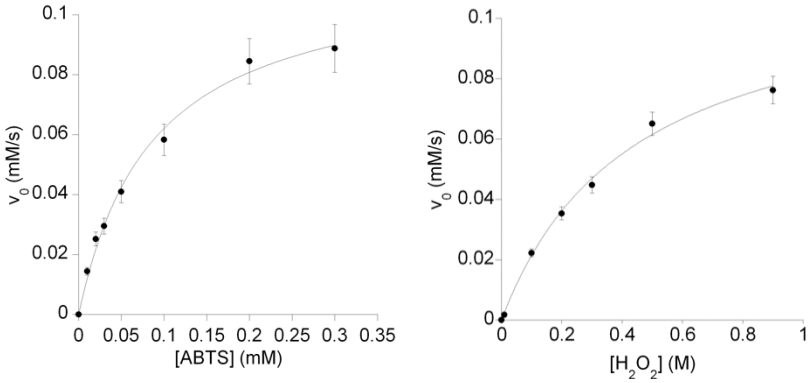


**Figure 1.30.** Peroxidase-like activity of $Fe^{III}$–MC6a. **Left**. Dependence towards ABTS: reaction conditions were $Fe^{III}$–MC6a (20 nM), $H_2O_2$ (450 mM) in 50 mM phosphate buffer pH 6.5/TFE (1:1 v/v). **Right**. Dependence towards $H_2O_2$: reaction conditions were $Fe^{III}$–MC6a (20 nM), ABTS (2 mM) in 50 mM phosphate buffer pH 6.5/TFE (1:1 v/v).

## 1.3.5 pH AND FOLDING EFFECT ON THE CATALYTIC ACTIVITY OF $Fe^{III}$-MC6a

Peroxidase-like activity of $Fe^{III}$-MC6a was then measured as a function of pH. Catalysis was performed at fixed ABTS, $H_2O_2$ and enzyme concentrations in 50 mM phosphate buffer, varying the pH values. Plotting of the reaction rate as a function of pH showed a "bell" shaped curve with the highest activity of $Fe^{III}$-MC6a being at pH 6.5 ± 0.1 (Figure 1.31). The parent molecule, $Fe^{III}$-MC6a, and all the molecules of the first generation of MC6 analogues exhibited the highest activity at the same pH value.[66,67] This finding suggests that the amino acid mutation did not affect the pH at which the maximum of activity was observed.

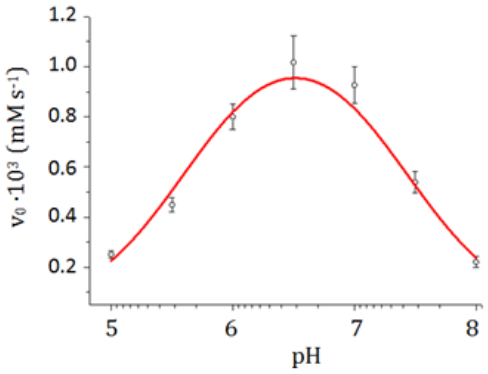


**Figure 1.31.** pH-dependent reaction rate during ABTS oxidation catalyzed by $Fe^{III}$-MC6a (20 nM) in phosphate buffer 50mM. The highest activity was reached at pH 6.5.

Data fitting of $v_0$ *versus* pH, according to model Equation 1.3, gave two pKa values: $pKa_1 \approx 5$ and $pKa_2 \approx 8$, with the maximum of activity at pH ≈ 6.5.

$$k_{cat}H' = \frac{k_{cat}}{1 + \frac{[H^+]}{K_{a1}} + \frac{K_{a2}}{[H^+]}}$$

**Equation 1.3**

This indicated that two ionizable groups were at least involved in the catalysis. In the previous work,[67] the first pKa was supposed to be due to the deprotonation of the $Glu^2$ on the decapeptide chain, which ion-pairs with the $Arg^{10}$ residue on the tetradecapeptide chain. This ion pairing stabilized the sandwich structure and positively influenced the catalytic properties. At pH 3.0, *bis*-aquo iron axial coordination species was the most abundant one. For increasing pH values, a second species start to be present, reaching the maximum concentration at pH 5.5. It corresponded to the active His-iron-water coordination form. In spite of that, the highest catalytic activity was not observed at pH 5.5 but at pH 6.5. This can be explained assuming that before start the catalytic cycle, hydrogen peroxide should be deprotonated to $OOH^-$. Considering the $H_2O_2$ pKa is 11.7, at pH 6.5 there will be a higher molar fraction of $OOH^-$ compared to pH 5.5, even though the molar fraction of catalytic active His/water form correspond to the 68% at pH 6.5. Increasing the pH values from 6.5 to 8.0 a decreasing in in the catalytic activity was observed. This can be attributed to a higher molar fraction of the histidine-iron-hydroxide coordination form.

Indeed, the optical transition observed in the UV/Vis pH titration with midpoint at pH ≈ 7 (data not shown), has been attributed to a ligand exchange from water to the harder hydroxide ion ligand. This ligand exchange, occurring at the distal site above pH 6.5, interferes with the $H_2O_2$ binding and catalysis triggering, causing a decrease in efficiency.

$Fe^{III}$-MC6a catalytic activity was then studied varying TFE concentration to correlate the peptide helix content on the catalytic activity. As reported in Figure 1.32, increasing TFE concentration the catalytic activity rising reaching a maximum around 30 % (v/v) of TFE. This perfectly correlates with the increase of the α-helix content (Figure 1.32, filled circles). This result demonstrates that correct folding of this synthetic class of enzymes is necessary to achieve their functions. Comparison of $Fe^{III}$-MC6a catalytic behavior and the previous $Fe^{III}$-$E^2L$(*TD*)-MC6, as function of TFE concentration, pointed out that Aib mutations had a positive effect on the catalysis. In particular $Fe^{III}$-MC6a increased faster its catalytic activity, indeed 20% of TFE was sufficient to achieve *ca* 70 % of the maximum activity, while under the same catalytic conditions only 40% of $Fe^{III}$-$E^2L$(*TD*)-MC6 maximum activity was gained. Finally, 30% TFE was sufficient to exceed the performance of $Fe^{III}$-$E^2L$(*TD*)-MC6 molecule under its optimal catalytic conditions.

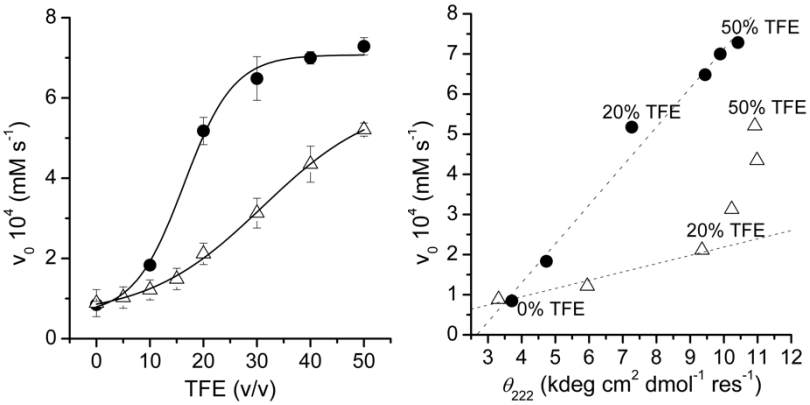


**Figure 1.32.** Catalytic performance of $Fe^{III}$-MC6a (20 nM) (closed circles) and $Fe^{III}$-$E^2L$(*TD*)-MC6 (20 nM) (open triangles). **Left:** initial rate of ABTS oxidation as a function of TFE. **Right:** initial rate of ABTS oxidation as a function of molar residue ellipticity at 222 nm as measured at different TFE concentrations.

This could be ascribed to a more compact tertiary arrangement of the new catalyst. This was indicated by the stronger correlation between the kinetic data and the helical contribution in terms of $\theta_{222}$. In the case of $Fe^{III}$-MC6a, higher helical content induced by TFE, results in a productive increase of the catalytic efficiency. Whilst, for the previous $Fe^{III}$-$E^2$L(*TD*)-MC6 the behavior observed was different. At 20% of TFE concentration no significant change in the initial rate was observed, although the helical content increased. In fact the $\theta_{222}$ for the peroxidase mimetics in this condition are similar (-7.2 MC6a; -9.3 $E^2$L(*TD*)-MC6 kdeg $cm^{-2}$ $dmol^{-1}$ $res^{-1}$), even though $Fe^{III}$-MC6a outplay its predecessor by a factor of three in ABTS oxidation. Likely, $Fe^{III}$-MC6a Decapeptide chain on average sits closer to the porphyrin, resulting in a stronger interaction with the heme at lower TFE concentration. Indeed, $Fe^{III}$-$E^2$L(*TD*)-MC6 reaches its desired globular folding only at TFE concentrations higher than 30%.

$K_M$ and $k_{cat}$ values of the catalyst were calculated using stopped-flow techniques for both $Fe^{III}$-$E^2L$(*TD*)-MC6 and $Fe^{III}$-MC6a.

**Table 1.7.** Catalytic parameters of $E^2L$(TD)-MC6a, MC6a and HRP.

| Enzyme | $K_m$ $H_2O_2$ (mM) | $K_m$ ABTS ($10^{-2}$mM) | $k_{cat}$ ($10^3$ $s^{-1}$) | $k_{cat}/K_m$ $H_2O_2$ ($10^3$ $mM^{-1}s^{-1}$) | $k_{cat}/K_m$ ABTS ($10^3$ $mM^{-1}s^{-1}$) | TON ($10^3$) |
|---|---|---|---|---|---|---|
| $E^2L$(TD)-MC6 | 130±20 | 5.0±.6 | 2.3±.2 | 0.018±.003 | 46±7 | 5.9 |
| MC6a | 440±50 | 9±1 | 5.8±.3 | 0.013±.002 | 64±8 | 14 |
| HRP | 0.93±.05 | 70±8 | 2.70±.03 | 2.9±.2 | 3.8±.5 | 50 |

As reported in Table 1.7, $Fe^{III}$-MC6a showed a turnover frequency and $k_{cat}$ value 2.5-times higher compared to its predecessor. However, the catalytic efficiencies ($k_{cat}/K_M$) for both hydrogen peroxide and ABTS, were comparable to those of $Fe^{III}$-$E^2L$(*TD*)-MC6, mainly due to the increase of the $K_M$ towards hydrogen peroxide (Table 1.7). This can be explained considering the accessibility to the active site, which due to the structural effect of the Aib residues, is now better hindered by the *D* chain. Moreover, the positive effect of $R^{10}$ is maximized,[32] thanks to the improved folding of the *D* chain, which results into a strong increase of the $k_{cat}$ value.

As the next step, turnover numbers (TON) in ABTS oxidation were determined. TON was calculated measuring the lowest $Fe^{III}$-MC6a concentration needed to oxidize 0.1 M of ABTS with an excess of hydrogen peroxide (3.0 mM). The reaction was followed by UV-vis spectroscopy reading at the wavelength of 660 nm corresponding to $ABTS^{\cdot+}$. Substrate was completed oxidized by 7 nM of $Fe^{III}$-MC6a, which corresponded to fourteen

thousand turnovers. The experimental data were interpolated with a pseudo-first order kinetic model, that considered the complete ABTS oxidation. The previous $Fe^{III}$-$E^2L$(*TD*)-MC6 catalyst was subjected to complete bleaching when 10.0 nM of catalyst was used under the same conditions. $Fe^{III}$-MC6a showed a 2-fold increase of TON without bleaching with respect to $Fe^{III}$-$E^2L$(*TD*)-MC6 (Figure 1.33).

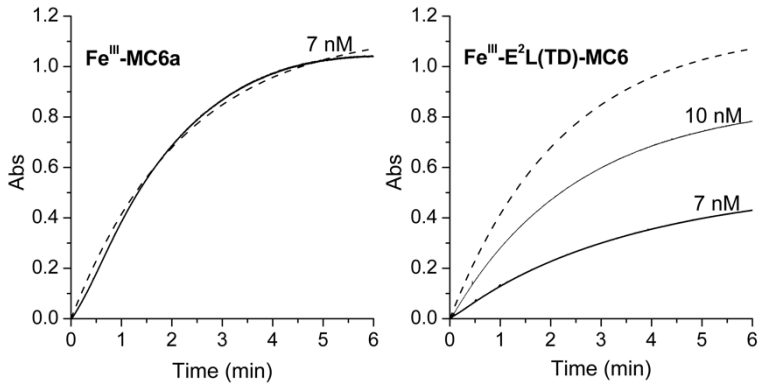


**Figure 1.33.** ABTS oxidation as followed at 660 nm catalyzed by 7.0 nM $Fe^{III}$-MC6a (A solid line) and by 7.0 and 10 nM $Fe^{III}$-$E^2L$(*TD*)-MC6 (B solid line). Dashed line curves simulate the complete ABTS oxidation considering a pseudo-first order kinetic model.

All these data pointed out the lower bleaching rate for $Fe^{III}$-MC6a. Since the TON has been correlated to the protective role of the *D* chain for this class of compounds,[2] these experiments point out that the decapeptide in $Fe^{III}$-MC6a is more stably positioned on the distal side of the heme. This would mean that ABTS electrons are more readily donated to the high-valence iron intermediate, thanks to the *D* chain, preventing catalyst oxidation processes to occur.

# CHAPTER 1.4

## CONCLUDING REMARKS AND OUTLOOK

The research project reported in this PhD thesis has been focused on the design, synthesis, and characterization of a new class of miniaturized enzymes with catalytic potential belonging to Mimochrome family. Starting from $Fe^{III}$-MC6, punctual amino acid substitutions have been introduced in the peptide sequence, with the aim to improve the catalytic activity. Substitutions were introduced on the *D* chain, since it presents higher conformational freedom, due to the lack of the coordinating histidine, which anchors the *TD* chain on the heme. The Aib (U) amino acid was introduced in 3 and 7 positions of the decapeptide chain, obtaining a new molecule, named MC6a. The Aib residue was chosen because of its reduced conformational freedom, inducing higher helical propensity into the peptide chain. The resulting enzyme was endowed with an improved chemical stability and a more produced a higher catalytic activity. Particularly, the helix-inducing U residues allowed $Fe^{III}$-MC6a to exceed in TON and in TOF its predecessors, with the side effect to increase $K_M$ for both substrates. Despite the progresses obtained in this field, other issues remain to be addressed. Indeed, this compound still suffers of some degradation at higher concentrations of hydrogen peroxide. Our rational design provided an answer to the request of stability by increasing the interaction between the porphyrin and the *D* peptide chain. Furthermore, $Fe^{III}$-MC6a presents other advantages compared to HRP, over all the reduced size (3.5 kDa), and the easy scale-up of the synthetic route. Exploiting these beneficial features, the use of this catalyst for potential biotechnological applications is currently under evaluation.

# CHAPTER 1.5

## *Materials and Methods*

## *1.5.1 MATERIALS AND METHODS*

Peptide synthesis was carried out using reagent grade anhydrous solvents. All the solvents used during HPLC and LC-MS analysis as well as during the spectroscopic characterization stages were HPLC-grade or higher grade (Romil). Scavengers (EDT, TIS, TES) and TFE were supplied by Sigma Aldrich; TFA and DIEA were from Applied Biosystem; acetic anhydride was from Fluka and piperidine was from Merck. DMF, DCM, NMP, HFIP, ethanol and methanol were supplied by Romil. All reagents were used without further purification. The NovaSyn® TG Sieber resin (substitution level 0.45 mmol/g) and all the *N*-α-Fmoc amino acids were purchased from NovaBiochem; activating agents HOBt, HATU and PyBop were provided by LC Sciences, Anaspec and NovaBiochem, respectively. Deuteroporphyrin IX was from Porphyrin Products. Cobalt (II) acetate and iron (II) acetate were purchased from Sigma Aldrich. Precoated silica G-60 plates, F254, purchased from Merck, were used for thin-layer chromatography (TLC). Phosphate salts (mono- and dibasic) for buffer preparation were provided by Fluka. Solvent mixtures are indicated in the respective sections. HPLC and LC-MS analyses were performed with a Shimadzu LC-10ADvp equipped with an SPDM10Avp diode-array detector. ESI-MS spectra were recorded on a Shimadzu LC-MS-2010EV system with ESI interface and Shimadzu LC-MS solution Workstation software for data processing. A Q-array-octapole-quadrupole mass analyzer was used as detector. Mass tandem experiments were recorded on Shimadzu LC-MS-8040 triple quadrupole equipped with ESI ionization source. Argon was used as ion gas in the CID cell and data were analyzed by Shimadzu LC-MS solution Workstation software, while tandem mass spectra were analyzed using thesoftware Molecular weight calculator. The optimized MS parameters were selected as followed: curved desolvation line

(CDL) temperature 250°C; block temperature 250°C; probe temperature 250°C; detector gain 1.6 kV; probe voltage +4.5 kV; CDL voltage -15 V. Nitrogen served as nebulizer gas (flow rate: 1.5 $L \cdot min^{-1}$).

Preparative flash chromatography purifications were performed using a Biotage ISOLERA flash purification system, ISO-1SW model, equipped with a diode-array detector.

Preparative HPLC purifications were performed with a Shimadzu LC-8A equipped with an SPD-10A detector.

UV-Vis studies were performed on Cary Varian 50 Probe UV Spectrophotometer or a Shimadzu UV-2401PC spectrophotometer. Circular dichroism (CD) spectra were collected on a Jasco CD J-815 calibrated with ammonium [D10] camphorsulfonate ([θ] = 7910 deg $cm^2$ $dmol^{-1}$ 290.5), depending on the observed region, the 0.1-cm or 1.0-cm path-length quartz cells were used.

Kinetic studies were performed on stopped flow instrument SX20 from Applied Photophysics in double mixing mode was used to measure kinetic parameters such as $K_M$ and $k_{cat}$. Kinetics were acquired for 10 s (4000 points per acquisition with external trigger). All kinetic studies were performed at 25°C in a 20 μL chamber with 1.0 cm path length. Solution is incubated for 1 ms before acquisition. The instrument was blanked prior acquisition.

Electrochemical experiments were carried out with a 620D potentiostat (CH Instruments). Ag/AgCl (1 M KCl) and platinum wires were used as reference and counter electrode, respectively. Controlled potential electrolysis (CPE) was performed in a custom electrolysis cell (Adams & Chittenden) with three equi-volume chambers of 1.5 cm diameter and 6 cm height. The chambers are separated by 10-mm diameter P5 (1.0-

1.6 μm pore size) glass, the central cell compartment contains the mercury pool electrode, which is connected to the potentiostat through an insulated platinum wire, each compartment was sealed by a gas-tight septum. Cyclic voltammetry (CV) experiments were performed with a hanging mercury drop electrode (HMDE) from Institute of Physical Chemistry of the Polish Academy of Sciences. pH was monitored using a VWR SB70P pH-meter and a Mettler Toledo InLab semimicro pH probe. GC analysis was carried out on a Shimadzu GC-17A injection temperature 110 °C (direct injection), nitrogen was used as carrier gas with a pressure of 34 kPa, oven temperature at 28 °C and a detector temperature at 140 °C.

The molecular graphics pictures were generated with PyMOL software (DeLano Scientific ltd)[75] and VMD software (Visual Molecular Dynamics)[76].

Data analysis was made by using Origin Pro8 and Kaleidagraph softwares.

## *1.5.2 SOLID-PHASE PEPTIDE SYNTHESIS*

Peptides were synthesized using a ABI 433 automatic peptide synthesizer, and by the use 3L Steroglass reaction vessel equipped with IKA 20 Digital stirrer and Temp 7 PT100 XS digital thermometer and nitrogen delivery system. Protocols involving the use of 9-Fluorenylmethoxycarbonyl (Fmoc) chemistry were used. Super acid labile NovaSyn® TG Sieber amide resin (substitution level 0.45 mmol/g) was chosen for both peptides. The following peptides were synthesized:

- Tetradecapeptide (*TD*): Ac-Asp-Leu-Gln-Gln-Leu-His-Ser-Gln-Lys-Arg-Lys-Ile-Thr-Leu-$NH_2$;
- Decapeptide (*D*): Ac-Asp-Glu-Aib-Gln-Leu-Ser-Aib-Gln-Lys-Arg-$NH_2$;
- His6Orn(*TD*): Ac-Asp-Leu-Gln-Gln-Leu-Orn-Ser-Gln-Lys-Arg-Lys-Ile-Thr-Leu-$NH_2$;
- His6(3-Py)Ala (*D*): Ac-Asp-Leu-Gln-Gln-Leu-(3-Py)Ala-Ser-Gln-Lys-Arg-Lys-Ile-Thr-Leu-$NH_2$.

The following orthogonally protected amino acids were used during peptide synthesis: Fmoc-Asp(OtBu)-OH; Fmoc-Leu-OH; Fmoc-Gln(Trt)-OH; Fmoc-His(Trt)-OH; Fmoc-Ser(tBu)-OH; Fmoc-Lys(Mtt)-OH; Fmoc-Arg(Pbf)-OH; Fmoc-Lys(Boc)-OH; Fmoc-Ile-(OH); Fmoc-Thr(tBu)-OH; Fmoc-Glu(OtBu)-OH; Fmoc-Aib-OH; Fmoc-Orn(Mtt)-OH; Fmoc-3-(3-Pyridil)Ala-OH.

Once loaded Fmoc protected Siber amide resin in reaction vessel, it is washed twice with 20 mL/g of dichloromethane and twice with 20 mL/g of N-Methyl-2-pyrrolidone (NMP).

The steps performed in the synthetic procedure can be summarized as follows:

**1.** Deprotection: Fmoc group was removed with a 20% piperidine solution in NMP. After Fmoc deprotection, a washing step with NMP was performed.

**2.** Activation: the carboxyl group of each Fmoc-protected amino acid was activated by addition of 1 equivalent of PyBop. Alternatively, HATU was used for coupling reactions involving sterically hindered amino acids.

**3.** Coupling: the pre-activated Fmoc-amino acid reacted with the free amino-terminal group of the growing peptide chain on the resin using NMP as the reaction solvent.

**4.** Capping: this reaction was performed after each coupling step, using $Ac_2O$/HOBt/DIEA solution in NMP. Capping cycle was introduced to prevent deletion byproducts.

When peptide synthesis was achieved, the resin was repeatedly washed with DCM, NMP, ethyl ether and dried under vacuum.

## 1.5.3 SOLUTION-PHASE SYNTHESIS OF APO-MC6a

Commercial DPIX and the synthesized peptides were coupled by amide bond formation between propionic acids of DPIX and the amino group of the 4-methyltrityl (Mtt)-protected Lys at position nine of each peptide chain.[71]

### DEPROTECTION STEPS

Mtt deprotection from Lys9 (TD) and Lys9 (D) was performed by several wash cycles (approximately 20) using 1% trifluoroacetic acid (TFA), 5% triisopropylsilane (TIS) in DCM. A volume of 10 mL of cleavage solution for each gram of resin was used. Washes were performed until disappearance of the peptide spot on TLC (eluent: DCM/methanol=9/1). Visualization of TLC plates was performed both by UV light and the ninhydrin assay. All washes were collected and neutralized with pyridine until neutrality. The mixture was then concentrated up to 10% of its volume under reduced pressure. Peptide solutions were then transferred to centrifugal tubes and ice-cold deionized water was added to precipitate the protected peptides. The tubes were then centrifuged at 4000 rpm until clarification of the aqueous phase (about 10 minutes). The aqueous phase was then poured off and fresh ice-cold deionized water was added to wash the precipitate from any water-soluble contaminants. Before each centrifuge cycle, the suspension was left in an ice bath, in order to promote precipitation of the peptide. This procedure was repeated twice more. The peptide cakes were then dried over $P_2O_5$ under vacuum for 16h.

### *TETRADECAPEPTIDE CHAIN COUPLING TO DEUTEROPORPHYRIN IX*

To a stirring solution of DPIX (1.23 g; 2.8 mmol) in a pyridine-DMF mixture (200 mL, 1:4 v/v), kept under nitrogen atmosphere, HATU (1.1 equivalents)) was added in one portion. Then, a solution of the orthogonally protected peptide (4.45 g; 2.1 mmol) in DMF (50 mL) was added dropwise and in small portions (30 additions) in order to limit the formation of the undesired *bis*-substituted adduct. The reaction mixture was stirred for 2 h at room temperature and the pH value was adjusted by addition of DIEA (pH ≈ 8.0). HPLC analysis of the reaction mixture was run repeatedly for reaction monitoring (column: Vydac C8, 4.6 mm·150 mm; 5 μm; running eluent: solvent A, $H_2O$/0.1% TFA (v/v); solvent B, acetonitrile/0.1% TFA (v/v); linear gradient, from 50 to 90% B over 20 min, at 1.0 $mL \cdot min^{-1}$ flow rate.

Two equally abundant peaks were detected. Both peaks show the molecular mass expected for the (TD)-DPIX. The mixture was then evaporated under reduced pressure.

The resulting mixture (≈14g) was dissolved in DCM (10 mL) and eventually subjected to a rough purification from the excess of DPIX using a silica gel column chromatography (eluent: DCM/MeOH= 9/1).

### *COUPLING REACTION OF THE DECAPEPTIDE CHAIN TO (TD)-DPIX*

To a stirring solution of (TD)-DPIX (5,5 g; 2.1 mmol) in 300 mL of pyridine-DMF mixture (1/4 v/v), kept under nitrogen atmosphere, a solution of the orthogonally protected decapeptide (2.8g; 2 mmol) in anhydrous DMF (10 mL) was added in one portion. Then, HATU (1.1 equivalents) was added to the mixture. The resulting solution was left under stirring for 1h at room temperature. Since the lipophilicity of the coupling product was not suitable for RP-HPLC analysis, the latter was performed after deprotection of a small amount of the crude residue with TFA:EDT:$H_2O$:Thioanisole:TIS (90: 2.5: 2.5: 4 : 1 v/v; 3h; RT) (EDT: 1,2-ethandithiol). The deprotection product was precipitated in ice-cold methyl *t*-butyl ether (MTBE), redissolved in $H_2O$ 0.1% TFA and analysed (column: Vydac C18, 4.6 mm·150 mm; 5 μm; running eluent: solvent A, $H_2O$/0.1% TFA (v/v); solvent B,ACN/0.1% TFA (v/v); linear gradient, from 10 to 50% B over 60 min, at 0.5 mL·$min^{-1}$ flow rate.

MS analysis was consistent with the formation of the desired product (D)(TD)DPIX (experimental: *m/z* 1147.0 [M+3$H^+$]; 860.55 [M+4$H^+$]; theoretical: *m/z 3438.3*). Other products showing different retention time and m/z ratio also formed, as the peptides were not purified before conjugation to the DPIX. No signs of alkylation were detected, confirming the efficiency of the cleavage mixture.

### *FINAL DEPROTECTION STEP*

Protective groups in (D)-(TD)-DPIX were eventually removed using the same mixture as before (TFA : EDT : $H_2O$ : Thioanisole: TIS = 90 : 2.5 : 2.5 : 4 : 1 v/v, 200 mL). The deprotection mixture was kept in ice cold bath before addition of the dried peptide. After 2 hours, HPLC analysis confirmed the completion of deprotection reaction (Figure 1.34). The mixture was then concentrated under reduced pressure and transferred to glass centrifugal tubes for compound precipitation using ice-cold MTBE, which was performed repeatedly. The crude peptide was then dissolved in $H_2O$ 0.1% TFA (v/v) and lyophilized to obtain the desired product as an amorphous powder form (≈9 g).

The lyophilized free base was purified by HPLC. Samples of the crude peptide (500 mg dissolved in 200mL of $H_2O$ 0.1% TFA (v/v)) were purified by RP-HPLC (column: Vydac C18 250mm x 5cm; running eluents: solvent A, $H_2O$ 0.1% TFA; solvent B, ACN 0.1% TFA; linear gradient from 5 to 80% B over 55 min at 100 mL/min flow rate) (Figure 1.35 and 1.36).

Analytical RP-HPLC analysis (Vydac C18, 150mm x 4.6mm) was then performed for each fraction. Fractions with high purity (>90%) were concentrated under reduced pressure and lyophilized. The free base was obtained as TFA salt (40% yield).

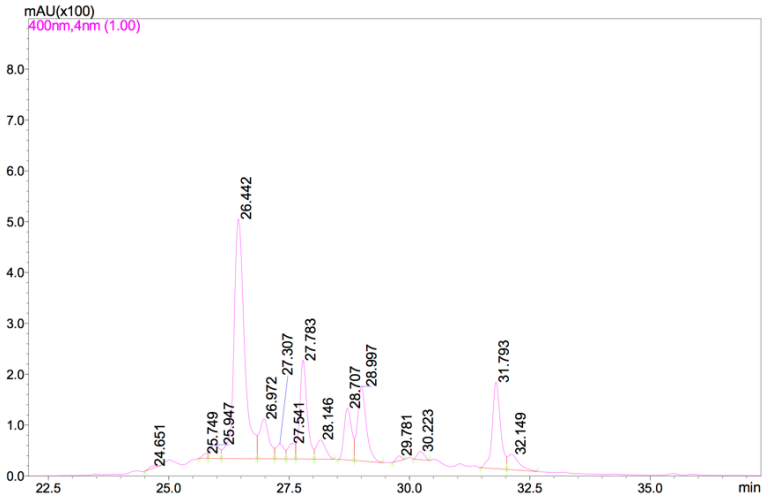


**Figure 1.34.** HPLC profile of apo-MC6a reaction crude. Desired product $R_t$ 26.442 min.

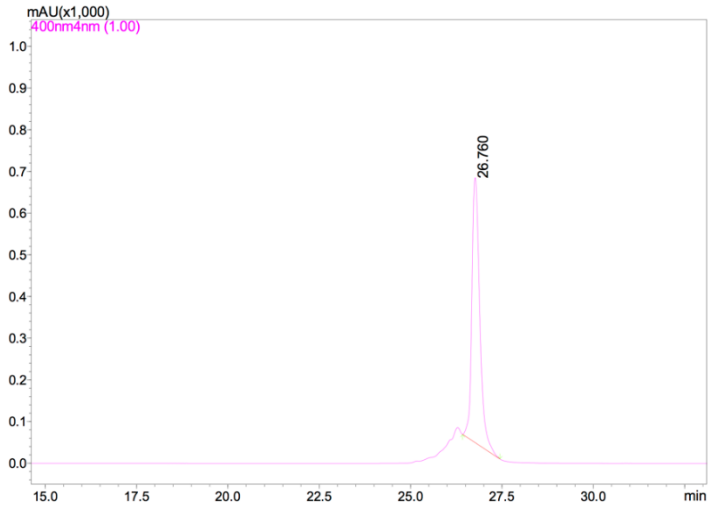


**Figure 1.35.** HPLC profile of *apo*-MC6a after purification by RP-HPLC.

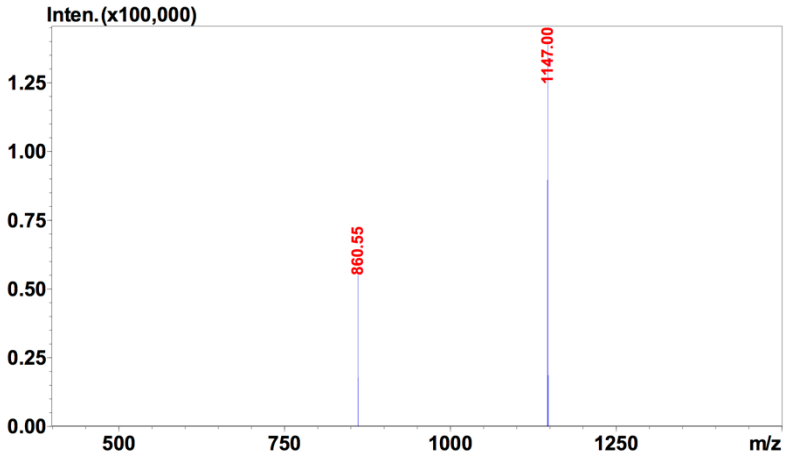


**Figure 1.36.** Mass spectrum of *apo*-MC6a after purification by RP-HPLC. *m/z* **1147.00** ($[M+3H]^{3+}$) and **860.55**($[M+4H]^{4+}$), which were consistent with the theoretical mass of *m/z* **3438.30** ($[M+H]^{+}$).

## *1.5.4 METAL INSERTION: GENERAL PROCEDURE*

*Apo*-Mimochrome VIa was dissolved in a AcOH-TFE mixture (6/4 v/v), with a concentration of 20mg/mL. Then, a 20-fold molar excess of metal ion as acetate salt was added.[60] The reaction was performed under nitrogen atmosphere at 50 °C for 3 h. Metal insertion was monitored by analytical RP-HPLC (column: Vydac C18 150mm x 4.6mm; running eluents: solvent A, $H_2O$ 0.1% TFA; solvent B, ACN 0.1% TFA, linear elution gradient from 5- to 80% B over 35 min, flow rate 1 mL/min) and by UV-Vis spectroscopy.

The resulting mixture was concentrated under reduced pressure, re-dissolved in 10mL of $H_2O$ 0.1% TFA and desalted by flash chromatography. Catalyst was loaded on a SNAP KP-C18-HS 50g $SiO_2$ C18 RP column, elution gradient from 0 to 95% ACN 0.1% TFA over 20 min, flow rate 40 mL/min. Fractions were then collected and concentrated. Pure products were obtained as the TFA salt. Reverse phase analytical HPLC coupled with ESI-MS confirmed the expected molecular weight.

## *1.5.5 STOPPED FLOW KINETIC STUDIES*

Catalytic activity of $Fe^{III}$-MC6a was tested by oxidizing chromogenic substrate ABTS by hydrogen peroxide, following absorption at $\lambda$ = 660 nm. $K_M$ for ABTS and $H_2O_2$ were measured keeping one of the two substrates constant while varying the other and *vice versa*.

Enzyme concentration in all the experiments was fixed at $2 \cdot 10^{-8}$ M. For the determination of $K_M^{H2O2}$, ABTS concentration was fixed at 2 mM while $H_2O_2$ was varied from 0 to 900 mM. For the determination of $K_M^{ABTS}$, $H_2O_2$ concentration was fixed at 450 mM while ABTS concentration was varied from 0 to 0.3 mM.

Pro-Data SX program was used to control the system and extract $v_0$ values (Abs $s^{-1}$). After conversion in mM $s^{-1}$, Kaleidagraph 4.1 was used to fit the data points into Michaelis and Menten equation.

The two sets of $v_0$ values obtained for both ABTS and hydrogen peroxide catalytic activity dependency, were then fitted separately using Michaelis-Menten Equation 1.4

$$v = \frac{v_{max}[S]}{K_m + [S]}$$

**Equation 1.4**

From these fittings, initial values of $K_M$ and $k_{cat}$ were found.

# *REFERENCES*

1. Thomson, Null & Gray, null. Bio-inorganic chemistry. *Curr. Opin. Chem. Biol.* **2,** 155–158 (1998).
2. Maglio, O., Nastri, F. & Lombardi, A. Structural and Functional Aspects of Metal Binding Sites in Natural and Designed Metalloproteins. in *Ionic Interactions in Natural and Synthetic Macromolecules* (eds. Ciferri, A. & Perico, A.) 361–450 (John Wiley & Sons, Inc., 2012).
3. Atkins, P. W. *Shriver & Atkins' inorganic chemistry*. (Oxford University Press, 2010).
4. Holm, R. H., Kennepohl, P. & Solomon, E. I. Structural and Functional Aspects of Metal Sites in Biology. *Chem. Rev.* **96,** 2239–2314 (1996).
5. Ciferri, A. & Perico, A. *Ionic Interactions in Natural and Synthetic Macromolecules*. (John Wiley & Sons, 2012).
6. Foster, A. W., Osman, D. & Robinson, N. J. Metal Preferences and Metallation. *J. Biol. Chem.* **289,** 28095–28103 (2014).
7. Gursahani, S., Schoephoerster, R. T. & Prabhakaran, M. Exploring electron transfer between heme proteins of cytochrome C super family in biosensors: a molecular mechanics study. *J. Biomol. Struct. Dyn.* **26,** 329–338 (2008).
8. Gray, H. B. & Winkler, J. R. Electron Transfer in Proteins. *Annu. Rev. Biochem.* **65,** 537–561 (1996).
9. Nastri, F. *et al.* Design and engineering of artificial oxygen-activating metalloenzymes. *Chem. Soc. Rev.* **45,** 5020–5054 (2016).
10. Chan, M. K. Heme protein biosensors. *J. Porphyr. Phthalocyanines JPP* **04,** 358–361 (2000).
11. Privalle, C. T. Regulation of Intramitochondrial Cholesterol Transfer to Side-Chain Cleavage Cytochrome P-450 in Rat Adrenal Gland. *Proc. Natl. Acad. Sci.* **80,** 702–706 (1983).
12. Schäfer, G., Purschke, W. & Schmidt, C. L. On the origin of respiration: electron transport proteins from archaea to man. *FEMS Microbiol. Rev.* **18,** 173–188 (1996).

13. Goldberg, M., Dunning, S. & Bunn, H. Regulation of the erythropoietin gene: evidence that the oxygen sensor is a heme protein. *Science* **242,** 1412–1415 (1988).
14. Correia, M. A., Sinclair, P. R. & De Matteis, F. Cytochrome p450 regulation: the interplay between its heme and apoprotein moieties in synthesis, assembly, repair and disposal. *Drug Metab. Rev.* **43,** 1–26 (2011).
15. Reedy, C. J. & Gibney, B. R. Heme Protein Assemblies. *Chem. Rev.* **104,** 617–650 (2004).
16. Martinez, S. E., Huang, D., Ponomarev, M., Cramer, W. A. & Smith, J. L. The heme redox center of chloroplast cytochrome f is linked to a buried five-water chain. *Protein Sci. Publ. Protein Soc.* **5,** 1081–1092 (1996).
17. Mogi, T., Saiki, K. & Anraku, Y. Biosynthesis and functional role of haem O and haem A. *Mol. Microbiol.* **14,** 391–398 (1994).
18. Vainshtein, B. K. *et al.* Three-dimensional structure of catalase from Penicillium vitale at 2.0 A resolution. *J. Mol. Biol.* **188,** 49–61 (1986).
19. Igarashi, N., Moriyama, H., Fujiwara, T., Fukumori, Y. & Tanaka, N. The 2.8 Å structure of hydroxylamine oxidoreductase from a nitrifying chemoautotrophic bacterium, Nitrosomonas europaea. *Nat. Struct. Mol. Biol.* **4,** 276–284 (1997).
20. Tripathy, B. C., Sherameti, I. & Oelmüller, R. Siroheme. *Plant Signal. Behav.* **5,** 14–20 (2010).
21. Permyakov, E. *Metalloproteomics*. (John Wiley & Sons, 2009).
22. Lombardi, A., Nastri, F. & Pavone, V. Peptide-based heme-protein models. *Chem. Rev.* **101,** 3165–3189 (2001).
23. J Smith, L., Kahraman, A. & Thornton, J. *Heme proteins-Diversity in structural characteristics, function, and folding*. **78,** (2010).
24. Lanzilotta, W. N. *et al.* Structure of the CO sensing transcription activator CooA. *Nat. Struct. Biol.* **7,** 876–880 (2000).
25. Fülöp, V., Moir, J. W., Ferguson, S. J. & Hajdu, J. The anatomy of a bifunctional enzyme: structural basis for reduction of oxygen to water and synthesis of nitric oxide by cytochrome cd1. *Cell* **81,** 369–377 (1995).
26. Li, T., Bonkovsky, H. L. & Guo, J. Structural analysis of

heme proteins: implications for design and prediction. *BMC Struct. Biol.* **11,** 13 (2011).
27. Hüttemann, M. *et al.* The multiple functions of cytochrome c and their regulation in life and death decisions of the mammalian cell: from respiration to apoptosis. *Mitochondrion* **11,** 369–381 (2011).
28. Willies, S. C., Isupov, M. N., Garman, E. F. & Littlechild, J. A. The binding of haem and zinc in the 1.9 Å X-ray structure of Escherichia coli bacterioferritin. *JBIC J. Biol. Inorg. Chem.* **14,** 201–207 (2009).
29. Werck-Reichhart, D. & Feyereisen, R. Cytochromes P450: a success story. *Genome Biol.* **1,** reviews3003.1-reviews3003.9 (2000).
30. Girvan, H. M. & Munro, A. W. Heme Sensor Proteins. *J. Biol. Chem.* **288,** 13194–13203 (2013).
31. Bowman, S. E. J. & Bren, K. L. The chemistry and biochemistry of heme c: functional bases for covalent attachment. *Nat. Prod. Rep.* **25,** 1118–1130 (2008).
32. Sibbett, S. S. & Hurst, J. K. Structural analysis of myeloperoxidase by resonance Raman spectroscopy. *Biochemistry (Mosc.)* **23,** 3007–3013 (1984).
33. Isaac, I. S. & Dawson, J. H. Haem iron-containing peroxidases. *Essays Biochem.* **34,** 51–69 (1999).
34. Krainer, F. W. & Glieder, A. An updated view on horseradish peroxidases: recombinant production and biotechnological applications. *Appl. Microbiol. Biotechnol.* **99,** 1611–1625 (2015).
35. Veitch, N. C. Horseradish peroxidase: a modern view of a classic enzyme. *Phytochemistry* **65,** 249–259 (2004).
36. Welinder, K. G. Covalent structure of the glycoprotein horseradish peroxidase (EC 1.11.1.7). *FEBS Lett.* **72,** 19–23 (1976).
37. Poulos, T. L. & Kraut, J. The stereochemistry of peroxidase catalysis. *J. Biol. Chem.* **255,** 8199–8205 (1980).
38. Veitch, N. C. & Smith, A. T. Horseradish peroxidase. in *Advances in Inorganic Chemistry* **51,** 107–162 (Elsevier, 2000).
39. Everse, J. The structure of heme proteins Compounds I and II: some misconceptions. *Free Radic. Biol. Med.* **24,** 1338–1346

(1998).
40. Moore, G. R. & Pettigrew, G. W. *Cytochromes c: Evolutionary, Structural and Physicochemical Aspects*. (Springer Science & Business Media, 2012).
41. Savenkova, M. I., Kuo, J. M. & Ortiz de Montellano, P. R. Improvement of Peroxygenase Activity by Relocation of a Catalytic Histidine within the Active Site of Horseradish Peroxidase. *Biochemistry (Mosc.)* **37,** 10828–10836 (1998).
42. Berglund, G. I. *et al.* The catalytic pathway of horseradish peroxidase at high resolution. *Nature* **417,** 463–468 (2002).
43. Penning, T. M. & Jez, J. M. Enzyme Redesign. *Chem Rev* **101,** 3027–3046 (2001).
44. Momenteau, M. & Reed, C. A. Synthetic Heme-Dioxygen Complexes. *Chem. Rev.* **94,** 659–698 (1994).
45. Traylor, T. G. *et al.* Syntheses and NMR characterization of chelated heme models of hemoproteins. *J. Am. Chem. Soc.* **101,** 6716–6731 (1979).
46. David, S., James, B. R., Dolphin, D., Traylor, T. G. & Lopez, M. A. Dioxygen and carbon monoxide binding to apolar cyclophane hemes: durene-capped hemes. *J. Am. Chem. Soc.* **116,** 6–14 (1994).
47. Tetreau, C., Lavalette, D., Momenteau, M., Fischer, J. & Weiss, R. Structure-Reactivity Relationship in Oxygen and Carbon Monoxide Binding with Some Heme Models. *J. Am. Chem. Soc.* **116,** 11840–11848 (1994).
48. Mashiko, T., Reed, C. A., Haller, K. J., Kastner, M. E. & Scheidt, W. R. Thioether ligation in iron-porphyrin complexes: models for cytochrome c. *J. Am. Chem. Soc.* **103,** 5758–5767 (1981).
49. Collman, J. P., Brauman, J. I., Fitzgerald, J. P., Sparapany, J. W. & Ibers, J. A. Reversible binding of dinitrogen and dioxygen by a ruthenium 'picnic-basket' porphyrin. *J. Am. Chem. Soc.* **110,** 3486–3495 (1988).
50. Marques, H. M. Insights into porphyrin chemistry provided by the microperoxidases, the haempeptides derived from cytochrome c. *Dalton Trans.* 4371 (2007). doi:10.1039/b710940g
51. Casella, L. *et al.* Covalently modified microperoxidases as

heme-peptide models for peroxidases. *J. Inorg. Biochem.* **79,** 31–40 (2000).
52. Colonna, S., Gaggereo, N., Carrea, G. & Pasta, P. The microperoxidase-11 catalyzed oxidation of sulfides is enantioselective. *Tetrahedron Lett.* **35,** 9103–9104 (1994).
53. Laganowsky, A. *et al.* An approach to crystallizing proteins by metal-mediated synthetic symmetrization. *Protein Sci. Publ. Protein Soc.* **20,** 1876–1890 (2011).
54. Ueno, T. & Watanabe, Y. *Coordination Chemistry in Protein Cages: Principles, Design, and Applications*. (John Wiley & Sons, 2013).
55. Watkins, D. W. *et al.* Construction and in vivo assembly of a catalytically proficient and hyperthermostable de novo enzyme. *Nat. Commun.* **8,** 358 (2017).
56. Faiella, M. *et al.* De Novo Design, Synthesis and Characterisation of MP3, A New Catalytic Four-Helix Bundle Hemeprotein. *Chem. – Eur. J.* **18,** 15960–15971 (2012).
57. Farid, T. A. *et al.* Elementary tetrahelical protein design for diverse oxidoreductase functions. *Nat. Chem. Biol.* **9,** nchembio.1362 (2013).
58. Koder, R. L. *et al.* Design and engineering of an O(2) transport protein. *Nature* **458,** 305–309 (2009).
59. Anderson, J. L. R. *et al.* Constructing a man-made c-type cytochrome maquette in vivo: electron transfer, oxygen transport and conversion to a photoactive light harvesting maquette. *Chem. Sci.* **5,** 507 (2014).
60. Nastri, F. *et al.* Hemoprotein Models Based on a Covalent Helix-Heme-Helix Sandwich: 1. Design, Synthesis, and Characterization. *Chem. - Eur. J.* **3,** 340–349 (1997).
61. Nastri, F. *et al.* Hemoprotein models based on a covalent helix-heme-helix sandwich. 3. Coordination properties, reactivity and catalytic application of Fe(III)- and Fe(II)-mimochrome I. *J. Biol. Inorg. Chem.* **3,** 671–681 (1998).
62. D'Auria, G. *et al.* Hemoprotein Models Based on a Covalent Helix-Heme-Helix Sandwich: 2. Structural Characterization of CoIII Mimochrome I δ and δ Isomers. *Chem. - Eur. J.* **3,** 350–362 (1997).
63. Lombardi, A. *et al.* Miniaturized hemoproteins: design,

synthesis and characterization of mimochrome II. *Inorganica Chim. Acta* **275–276,** 301–313 (1998).
64. Costanzo, L. *et al.* Miniaturized heme proteins: crystal structure of Co(III)-mimochrome IV. *JBIC J. Biol. Inorg. Chem.* **9,** 1017–1027 (2004).
65. Lombardi, A. *et al.* Design of a New Mimochrome with Unique Topology. *Chem. - Eur. J.* **9,** 5643–5654 (2003).
66. Nastri, F. *et al.* A Heme-Peptide Metalloenzyme Mimetic with Natural Peroxidase-Like Activity. *Chem. - Eur. J.* **17,** 4444–4453 (2011).
67. Vitale, R. *et al.* Artificial heme-enzyme with enhanced catalytic activity: evolution, functional screening and structural characterization. *Org. Biomol. Chem.* (2015). doi:10.1039/C5OB00257E
68. Schweitzer-Stenner, R., Gonzales, W., Bourne, G. T., Feng, J. A. & Marshall, G. R. Conformational Manifold of α-Aminoisobutyric Acid (Aib) Containing Alanine-Based Tripeptides in Aqueous Solution Explored by Vibrational Spectroscopy, Electronic Circular Dichroism Spectroscopy, and Molecular Dynamics Simulations. *J. Am. Chem. Soc.* **129,** 13095–13109 (2007).
69. Improta, R., Rega, N., Aleman, C. & Barone, V. Conformational Behavior of Macromolecules in Solution. Homopolypeptides of α-Aminoisobutyric Acid as Test Cases. *Macromolecules* **34,** 7550–7557 (2001).
70. O'Neil, K. T. & DeGrado, W. F. A thermodynamic scale for the helix-forming tendencies of the commonly occurring amino acids. *Science* **250,** 646–651 (1990).
71. Bourel, L., Carion, O., Gras-Masse, H. & Melnyk, O. The deprotection of Lys(Mtt) revisited. *J. Pept. Sci. Off. Publ. Eur. Pept. Soc.* **6,** 264–270 (2000).
72. Casella, L. *et al.* Axial Imidazole Distortion Effects on the Catalytic and Binding Properties of Chelated Deuterohemin Complexes. *Inorg. Chem.* **35,** 439–444 (1996).
73. Feis, A., Marzocchi, M. P., Paoli, M. & Smulevich, G. Spin state and axial ligand bonding in the hydroxide complexes of metmyoglobin, methemoglobin, and horseradish peroxidase at room and low temperatures. *Biochemistry (Mosc.)* **33,** 4577–4583

(1994).
74. A. Adams, P. The peroxidasic activity of the haem octapeptide microperoxidase-8 (MP-8): the kinetic mechanism of the catalytic reduction of H 2 O 2 by MP-8 using 2,2'-azinobis-(3-ethylbenzothiazoline-6-sulphonate)(ABTS) as reducing substrate. *J. Chem. Soc. Perkin Trans. 2* **0,** 1407–1414 (1990).
75. Schrödinger, L. L. C. The PyMOL Molecular Graphics System, Version 1.3r1. (2010).
76. Humphrey, W., Dalke, A. & Schulten, K. VMD: Visual molecular dynamics. *J. Mol. Graph.* **14,** 33–38 (1996).

# *SECTION 2*

## *Natural and Artificial Hydrogenases in Water Splitting Reaction*

# *CHAPTER 2.1*

## *Introduction to the*

## *Water Splitting Reaction*

## 2.1.1 WATER SPLITTING: THE "GREEN" WAY TO ENERGY STRORAGE

A large interest of scientific community versus renewable energy is currently increasing day by day, because of the climate changes due to the emissions of anthropogenic carbon dioxide ($CO_2$). Among all renewable energy sources, sunlight represents the biggest one in terms of energy density available on planet, with enough power to meet all of humanity's needs several times over.[1] However, this source is intermittent and not homogenously distributed on planet. Nature overpassed this inconvenient storing sun energy in chemical bonds. Using photosynthesis, plants and photosynthetic bacteria covert $CO_2$ and water into dioxygen and sugars. The energy needed to photosynthesis is provided by sunlight, which is captured with a fascinating reaction pathway.[2] Inspired by nature, the development of carbon free energy sources using sunlight represents a challenge in supplying the energy needs of the future.

Solar-driven water splitting in hydrogen and oxygen represents a valid alternative to the energy storage. Hydrogen is a dense energy source (enthalpy of combustion -286 kJ $mol^{-1}$) and a carbon-free fuel.[2] There are two general strategies potentially in use for water splitting, involving the employ of conventional solar panels for electricity generation (indirect hydrogen evolution by electrolysis), or the development of a single device enabling energy absorption from solar light and water splitting (direct conversion of solar energy in hydrogen through an artificial photosynthesis). The indirect approach (water electrolysis) needs of conventional and well-established technologies, even though multiple steps typically reduce process efficiency .[3]

Electrolytic cell for water splitting is reproduced in Figure 2.1. Under acidic conditions, water is oxidized at the anode, according to the reaction:

$$2H_2O \rightarrow O_2 + 4e^- + 4H^+$$

This is the oxygen evolution reaction (OER). Electrons move from the external circuit to the cathode, where they combine with protons to give hydrogen (hydrogen evolution reaction, HER) according to the following reaction:

$$4e^- + 4H^+ \rightarrow 2H_2$$

In the anodic section, four protons are produced, and vice versa four protons are consumed at the cathode. Protons move from the anodic to cathodic section: a semi-permeable membrane separator permits protons migration, allowing the cell to keep the overall electro-neutrality.

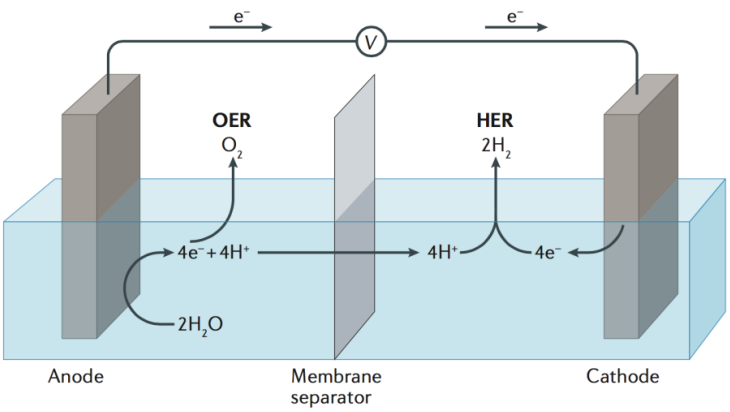


**Figure 2.1.** Schematic representation of an electrolytic cell for water splitting [reproduced from ref. 3].

To split water (as the sum of OER and HER), energy is needed, and the theoretical voltage that needs to be provided is 1.23 V. In addition, an extra-energy is required to observe electrons flowing

in the circuit. This additional voltage (often described with the symbol $\eta$) needed beyond the theoretical 1.23 V to observe a given current density is called "overpotential". Electrocatalysts have the role to reduce this overpotential as much as possible.[3] Noble metals like platinum and palladium present a near-theoretical overpotential (+0.07 V for platinum). However, noble metals are very expensive and their availability is scarce on earth. Therefore, research is currently focused on the development of catalysts for HER made by earth-abundant metals.[4]

Photovoltaic electricity generation from sun-light is grown considerably over the last years, but it is going to remain a small slice of global electricity generation, increasing from 0.4% to 2.6% in the next two decades. A problem limiting the wider expansion of solar energy is the high production price of photovoltaic cells.[5] However, the growing demand in photovoltaic cells allowed to increase the accessibility of that technology. Inspired by nature, scientists have been working to develop artificial photosynthesis, in which the light energy is stored in chemical bonds. Solar-driven water-splitting reaction represents a promising target reaction, because the energy storage in produced hydrogen, exceeds many times that of any existing battery.[6]

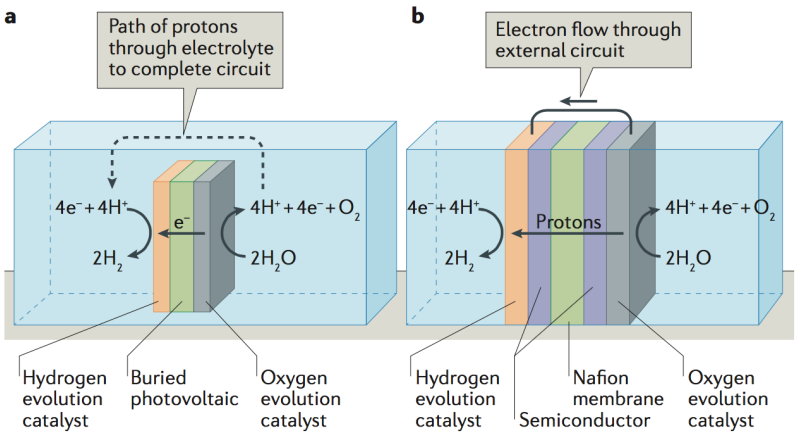


**Figure 2.2.** (a) Wireless configuration in which protons move through the solution and close the circuit. (**b**) Configuration in which the electrical circuit is closed by external wires. In both cases, light passes through the catalysts to be absorbed; thin and near-transparent catalyst layers are desirable. Figure reproduced from ref. 3.

To perform synthetic photosynthesis, sun-light energy has to be captured and employed to accomplish the water splitting reaction (involving both OER and HER). Solar hydrogen from water requires progress on both two half reactions and the coupling of them (Figure 2.2). HER half-reaction is less challenging to accomplish due to the smaller number of electrons needed to reduce one mole of hydrogen (2 electrons). *Vice versa* OER is hardly achieved, because it requires four-electrons for each oxygen molecule evolved, and last but not the least, the reaction passes through highly oxidizing intermedia, thus homogeneous catalysts bearing organic ligands are typically oxidized.[7]

Another effort to perform sunlight-promoted water splitting reactions is the needed to deliver electrons and protons rapidly and efficiently from the cathode to the anode. A delay in the charges migration cause a membrane potential, which is opposite to the reaction direction reducing the process total efficiency.

Because of the difficulty in performing the overall water splitting reaction, research is mainly focused on hydrogen evolution half-reaction from water using sacrificial chemical electron donors. This approach helps to bypass the problems typical of water oxidation half-reaction.[2]

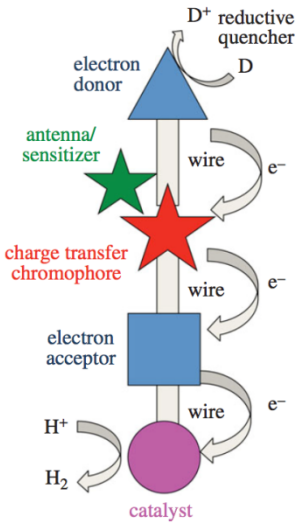


**Figure 2.3**. General scheme for the reductive side of water splitting. A photosensitizer converts light in energy that is transferred to a charge-transfer chromophore. Figure reproduced from ref. 2.

A general strategy for solar proton reduction is depicted in Figure 2.3. (1) Antennae and/or a charge-transfer chromophore captures solar photons efficiently. (2) An electron–hole pair is formed after chromophore excitation and/or by energy transfer, which must be separated with lower energy loss. (3) Charge accumulation on charge-transfer module and/or catalyst, represent the energy storage step. (4) Catalyst use this energy to promote the reaction. Electrons must have enough energy to

supply the reducing power and the overpotential value. (5) A sacrificial electron donor reduces the oxidized antenna/sensitizer, and the process can restart.[6]

Crucial points for the process are the antenna/charge-transfer chromophore energy conversion and the catalyst overpotential. It is possible to assume that high-performing electrocatalysts in the HER, are commonly good candidate in the photochemical hydrogen evolution.

## *2.1.2 NATIVE ENZYMES FOR PROTON REDUCTION: HYDROGENASES*

In nature are found metalloenzymes which are able to catalyze both hydrogen evolution and hydrogen oxidation reactions. Hydrogenases ($H_2$ases) catalyze protons reduction to molecular hydrogen and reversible hydrogen oxidation to give protons and electrons.[4]

$$2H^+ + 2e^- \rightleftharpoons H_2$$

$H_2$ase are widespread in nature, they are found in Archaea, Bacteria and in a few Eukarya and play a crucial role in microbial energy metabolism. The primary functions of hydrogenases are to provide energy for the organisms by oxidation of molecular hydrogen and to balance the redox potential of the cell.[8]

$H_2$ases can be classified in three subclasses, depending on the metal cofactor occurring in the active site: [NiFe], [FeFe], and [Fe] hydrogenases. The first two classes are the most abundant and studied; a common peculiarity among these enzymes is the presence iron sulfur clusters (4Fe4S and 3Fe4S), which are

involved in electron transfer processes between active site and protein surface (and vice versa)[9] (Figure 2.4). Another common feature of [NiFe] and [FeFe] enzymes is the presence of π-acid ligands, such as CO and $CN^-$, as ligands for metal ions in the active site (depending on the oxidation number of the metal ion in the active site). [Fe] $H_2$ases are less commonly found and studied, they are called iron-sulfur cluster free enzymes because of the absence of iron sulfur clusters. Iron hydrogenases use Fe-guanylylpyrodinol (Fe-GP) as the cofactor. This class of $H_2$ases catalyze the reduction of methenyltetrahydromethanopterin (metheny-H4MPT$^+$).

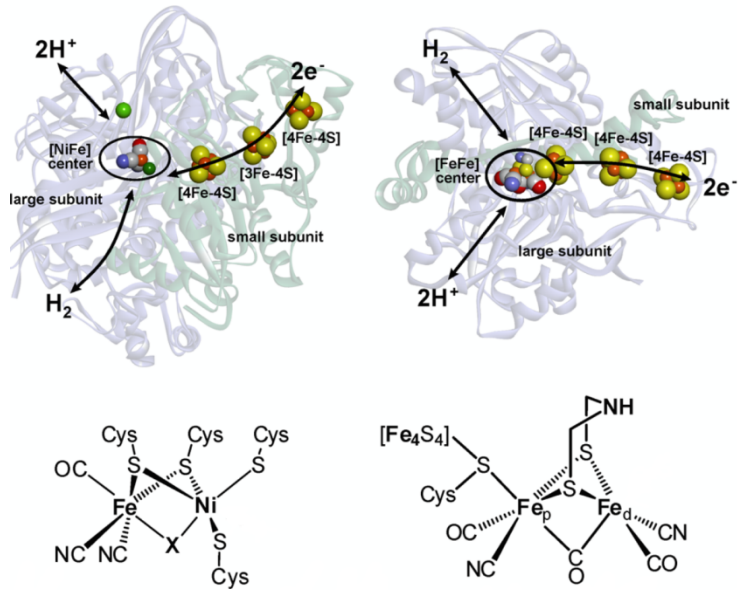


**Figure 2.4.** [NiFe] $H_2$ases (left) and [FeFe] $H_2$ases (right), with the corresponding active sites depicted below [image reproduced from ref. 4].

## 2.1.3 [NiFe] HYDROGENASES

[NiFe] $H_2$ases are generally composed of two subunits: one small subunit of ~29 kDa and one large subunit of ~63 kDa. The small subunit brings tree different iron-sulfur clusters, proximal 4Fe-4S, medial 3Fe-4S and distal 4Fe-4S clusters with respect to the distance from the active site. These three clusters connect the active site, which is deep inside the enzyme core, to the outside, allowing the electron transfer process. In the large subunit, the [NiFe] subcluster occurs, deeply buried into the core of the enzyme, and an additional Mg ion coordinate the C-terminus unit.[8] Only in the subclass of [NiFe] $H_2$ases, some specific enzymes were found to be oxygen tolerant. It should be noted that the structural features of all [NiFe] $H_2$ases are almost completely conserved, whether they are $O_2$-tolerant or $O_2$-sensitive enzymes. In the active site, there are four cysteine residues coordinating the nickel ion; two of them are involved in bridging the iron ion. In the resting state Fe center is in a low spin, +2 state, with an octahedral coordination geometry, involving two sulfide groups of bridging cysteines, three CO and or $CN^-$ ligands. The nature of the sixth bridging ligand depends on the oxidation state of the cluster. Cyanide and carbon monoxide are strong π-acid ligands and help to stabilize the lower oxidation number of the cluster; moreover, $CN^-$ is involved in hydrogen bonding with the protein backbone.[10]

In the large subunit, a gas-channel involved in the transportation of molecular hydrogen from the protein surface to the active site and vice versa has been identified.[11] The gas-channel is likewise accessible to inhibitory gases, such as CO and $O_2$. Its inner part is composed by nonpolar residues, such as Val74 and Leu122, which are conserved among all [NiFe] $H_2$ases.[12] These two

residues are located close to the active site, and represent a bottle neck limiting hydrogen diffusion.

The catalytic cycle of [NiFe] $H_2$ases starts from the resting state called Ni-$SI_a$ (Figure 2.5): the nickel ion is four-coordinated with one open bridge, both metals are in the +2 oxidation state. When hydrogen reaches the active site after passing through the gas-channel, a Ni-mediated heterolytic splitting occurs, releasing protons and hydride ions. $H^+$ protonates the Cys546 residues, while the hydride ion bridges the two metal ions. This second state in the catalytic cycle is named Ni-R.[13] The latter releases the proton from cysteine 546 and one electron from nickel ion, evolving in a paramagnetic state, identified as Ni-C. The loss of a further electron and a proton leads back to Ni-$SI_a$ closing the cycle.

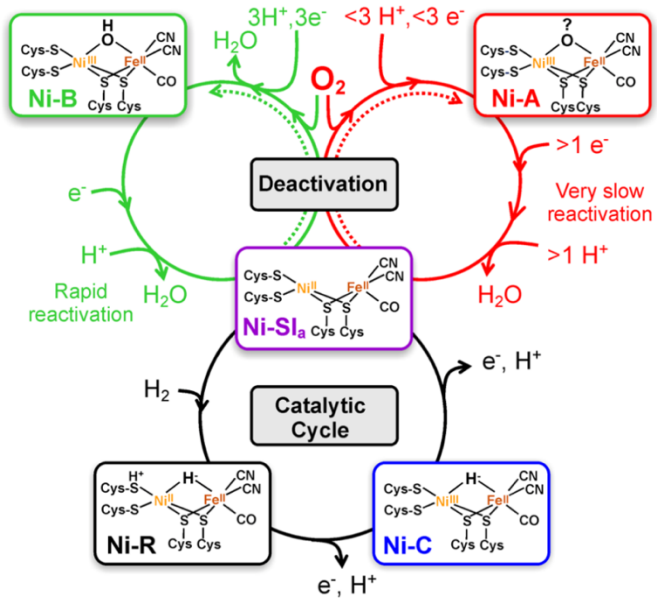


**Figure 2.5.** Black: catalytic cycle for [NiFe] hydrogenases. Red and green: deactivation and re-activation cycles for [NiFe] hydrogenases [reproduced from ref. 4].

Under aerobic conditions, [NiFe] hydrogenases are inactivated and occur as a combination of two resting states, named Ni-A and Ni-B.[14] Both states present the nickel ion in +3 oxidation state, with one bridging oxygen. The Ni-B state is also called "ready", because it is easily reactivated in seconds' time scale, vice versa the Ni-A state presents a slow activation rate. In Ni-B, studies indicated the presence of an oxygen bridging the two metal ions; however, its actual structure was not yet elucidated. When oxygen arrives to the active site, it needs four electrons to be completely reduced to a water molecule and a hydroxide ion, the latter bridging the position between iron and nickel, to form the Ni-B state. The first electron is easily taken from the reduced active site [Ni(II)Fe(II)]. Three remaining electrons could be given by the three FeS clusters occurring in the enzyme.[15] In fact the second electron is transferred from the proximal [4Fe-3S] and reduces the superoxide moiety into a hydroperoxide species, this reduction is fast because it requires little reorganization energy and is very close to the active site. The third electron comes from the medial cluster and formally breaks the oxygen bridge bond into water and a hydroxyl radical. Then, the distal [4Fe-3S] cluster reduces rapidly the medial cluster, providing the fourth electron to reduce the hydroxyl radical, forming the Ni-B state.[16]

Once obtained, the Ni-B state can be reactivated at high potential to release water. The high hydrophobicity of the active site suggested that water cannot escape from the active site. The crystal structures[17] suggest a direct water removal through a network of water molecules in a cavity. This detoxification process from oxygen is generally accepted, although not completely proved.

## 2.1.4 [FeFe] HYDROGENASES

[FeFe] hydrogenases are found in anaerobic prokaryotes, and eukaryotes such as clostridia, sulfate reducers and green algae.[8] Differently to [NiFe] hydrogenases, no [FeFe] $O_2$-tolerant enzymes have been discovered so far. Within the hydrogenases family, [FeFe] $H_2$ases showed the faster hydrogen evolution turnover frequency (TOF 1000 $s^{-1}$).[18] Accordingly, it is easy to understand the increasing interest for this class of enzymes.

All the [FeFe] $H_2$ases so far characterized share a common architecture, consisting of various [FeS] cluster domains linked to the H-cluster domain (Figure 2.6). The latter contains the active site and one additional [FeS] cluster, which function is to couple reversibly hydrogen oxidation/reduction electrons involved in metabolic processes.[19]

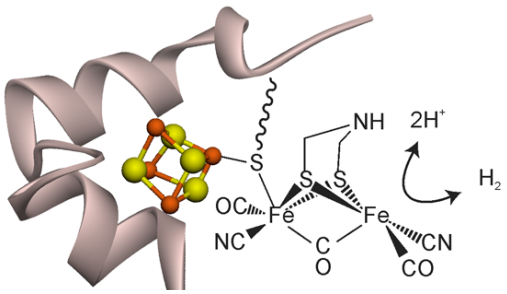


**Figure 2.6.** Representation of the [FeFe] hydrogenase (orange and yellow: the iron sulfur cubane) [reproduced from ref. 4].

Like in [NiFe] $H_2$ases, gas-channels are present to enable the access to substrate and inhibitors. In particular, in [FeFe] hydrogenases three gas channels have been found:[19] a "Channel A", which is connected to the cavity C; a "channel B", which is suggested to be the $O_2$ transport channel, and a "cavity C", which is near to the [FeFe] sub-cluster.

Many of the [FeFe] hydrogenases contain extra [2Fe-2S] or [4Fe-4S] clusters (F-clusters); however, [FeFe] hydrogenases from green algae only contain the H-cluster and no additional FeS cluster.[17] Therefore, the H-cluster domain is considered the functionally essential domain of [FeFe] hydrogenases.[20]

The active site is well conserved among [FeFe] $H_2$ases. It is the biggest subunit and is composed by two twisted β-sheet regions, coming together to form a cleft in which the H-cluster is located. The latter consists of a di-iron metal center with a disulfur bridge, which presents an amino group in beta position and one bridging CO. The coordination sphere of the two iron ions is eventually completed with $CN^-$ and CO ligands.[21] Furthermore, one of these irons (the proximal Fe) is linked to a cubane [4Fe-4S] cluster via a bridging cysteine sulfur. As observed earlier, $CN^-$ and CO act as π-acid ligands and stabilize the iron ion in low oxidation states.

Both cubane and the di-iron active site are redox active species, and six different oxidation states are possible. Two different oxidation states for cubane $[4Fe\text{-}4S]^{2+}$ or reduced $[4Fe\text{-}4S]^{+}$, and three for binuclear center (Fe(II)Fe(II), mixed Fe(I)Fe(II), and Fe(I)Fe(I)) may occur. Under physiologic conditions, only some of these states are accessible, i.e. the "active oxidized" state $H_{ox}$ ($[4Fe\text{-}4S]^{2+}$-Fe(I)Fe(II)) and the "active reduced state" state $H_{red}$ ($[4Fe\text{-}4S]^{2+}$-Fe(I)Fe(I)).[22]

For the two resting states $H_{ox}$ and $H_{red}$, a simple catalytic cycle has been proposed, in both resting states the cubane being in the oxidized +2 state (Figure 2.7).

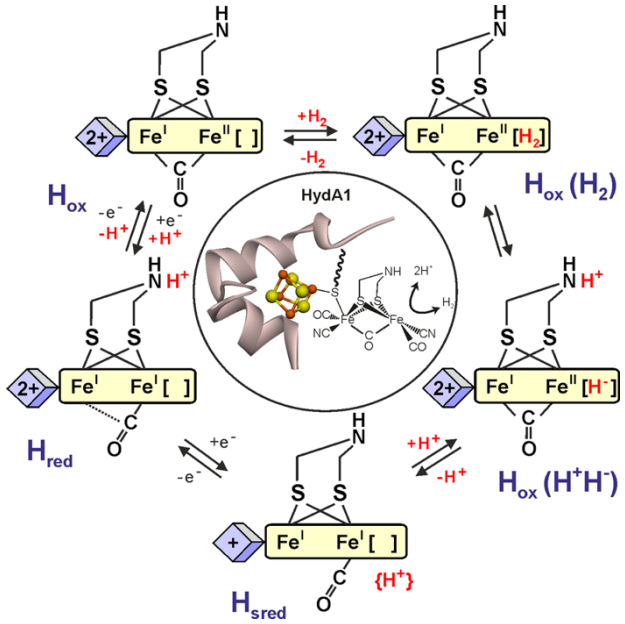


**Figure 2.7.** Catalytic cycle for [FeFe]$H_2$ases. Cubane is depicted as purple cube [reproduced from ref. 4].

Hydrogen coordinates $H_{ox}$-cluster in the open position of the iron ion, and it is rapidly splitted into $H^-$ and $H^+$, the latter protonating an endocyclic amino group ($H_{ox}$ $H^+H^-$). Two electrons from the hydride ion are transferred to the cluster, reaching the $H_{sred}$ state which is rapidly oxidized in the $H_{red}$ state. The fact that $H_{sred}$ has not been observed as a stable state in prokaryotic [FeFe] hydrogenases could be related to the presence of an accessory [4Fe-4S] cluster in these proteins. The intimate electronic contacts between the latter cluster and the $H_{sred}$-cluster contribute to the rapid re-oxidation of $H_{sred}$ to $H_{red}$.[22]

## 2.1.5 [Fe] HYDROGENASES

[Fe] hydrogenases are found only in *archaea* bacteria and catalyze one step of the pathway enabling the $H_2$-mediated conversion of $CO_2$ into methane; [Fe] hydrogenases in methanogens are up-regulated under conditions having a low nickel content.[23] This class of $H_2$ases is less studied and not yet well known.

If compared to the other two classes of hydrogenases, [Fe] $H_2$ases have a different action mechanism. They catalyze the reversible, $H_2$-mediated reduction of methenyltetrahydro-methanopterin (methenyl-$H_4$MPT$^+$) to methylene-$H_4$MPT, which represents the substrate. These enzymes have no iron sulfur clusters, accordingly they do not reduce electron acceptors.[24] Enzymes harbor only one Fe-guanylylpyrodinol (Fe-GP) cofactor, which is anchored to the protein through the guanosine monophosphate moiety (Figure 2.8).[25]

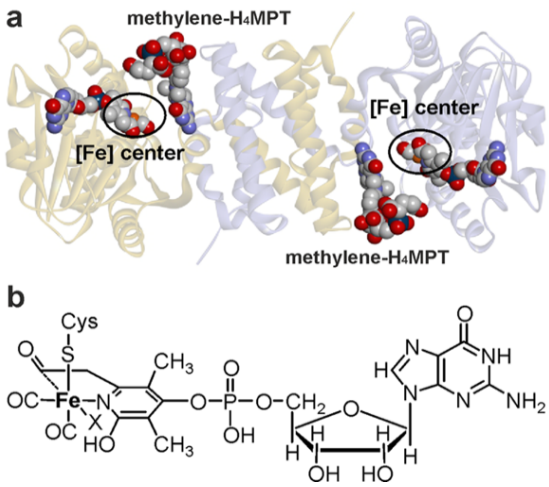


**Figure 2.8. a** Representation of the subunits of [Fe] hydrogenases with both the iron cofactor and the substrate in the active site. **b** Fe-guanylylpyrodinol (Fe-GP) cofactor. Figure reproduced from ref. 4.

[Fe] hydrogenase (38 kDa) is a homodimeric protein, consisting of two N-terminal units bound to the central globular C-terminal unit in a linear manner. It is suggested that the enzyme changes its conformation from close to open when two equivalents of methenyl-$H_4MPT^+$ bind the enzyme.

The iron center presents two CO ligands, one thiolate ligand from one Cys residue. The cofactor hosts two coordination sites, one pyridinyl moiety with the acyl-carbon ligand. Mössbauer data suggested that the oxidation state of the iron could be either low-spin Fe(0) or Fe(II).

The catalytic cycle of [Fe]$H_2$ases starts with the binding of methenyl-$H_4MPT^+$ to the open form of the enzyme.[22] Hydrogen enters through a hydrophobic gas-channel into the active site, which is shorter than the gas-channels found in the others hydrogenases. Then, the Fe-GP cofactor is activated and a hydrogen molecule binds to the open coordination site of the iron. The hydrogen molecule is heterolytically cleaved, the proton is transferred to the thiol function of Cys176, and the adjacent C14a carbocation of the methenyl- $H_4MPT^+$ accepts the hydride ion.[26]

## 2.1.6 ARTIFICIAL HYDROGENASES

Despite the considerable catalytic potential of hydrogenases in hydrogen oxidation, proton reduction devices based on natural hydrogenases to be used for artificial photosynthesis are far away to be developed. The main reasons should be searched into the size of hydrogenases, exceedingly larger than that of standard inorganic molecular catalysts, and in their sensitivity to dioxygen, which rapidly inactivate the enzymes. Accordingly, the number of artificial hydrogenases active in the water splitting reduction half-reaction, especially those made with earth abundant metals, is deeply increased over the last years. Indeed, there is a significant interest in developing small, functional hydrogenase mimics, as they are more amenable to detailed manipulation and study.[3,27]

A key inspiration tool behind the design of new catalysts for the hydrogen evolution reactions is the so-called Trasatti's volcano plot (Figure 2.9). The latter correlates, for a given metal, the HER exchange current densities (a measure of the capability of a catalyst for the HER) with the energy of the intermediate metal hydrogen bonding formed between absorbed H and the electrode surface. This trend was recorded for metals by Trasatti in the 1970s[28] and ever since it has been a fruitful treasure map for the development of new catalysts.[29] The plot highlights the optimum hydrogen binding energy (where the hydrogen is held neither too strongly nor too weakly) at which the maximum catalytic activity is obtained. Not surprisingly, noble metals such as platinum and rhodium fall near the apex of this volcano, where the maximal activity is found.[3]

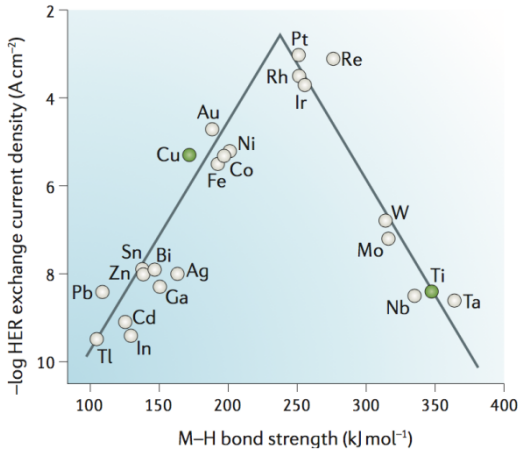


**Figure 2.9**. Trasatti's volcano plot of a bunch of transition metals [reproduced from ref. 3].

Interrogation of volcano plot allows to propose new catalysts for HER by combining catalysts that rank in the opposite positions of the volcano, with the aim to produce new molecules with intermediate hydrogen binding energy.[3]

Interestingly, in Trasatti's plot earth abundant metals including iron, cobalt, nickel and copper rank in a good position.[28] This suggests an explanation on why nature selected iron and nickel as metallic-cofactors for the active site of hydrogenases.

Among first transition metals raw, cobalt shows interesting catalytic property for HER. Cobalt complexes, and their interactions with hydrogen, have a long history from the original discoveries of $Co_2(CO)_8$, reacting with hydrogen to form $CoH(CO)_4$ by Hieber.[30] Numerous cobalt complexes, including systems containing macrocyclic and polypyridine ligands, were reported as catalysts for HER using proton sources upon electrochemical reduction more than twenty years ago.[31] In these

studies, organic acids such as triflic acid (HOTf) or anilinium salts were used as proton sources. Subsequently, Peters and coworkers studied the Co complexes depicted in Figure 2.10 as electrocatalysts for proton reduction.[30] Cobalt tetraimine was also soluble in non-aqueous media and trifluoroacetic acid was used as proton source.

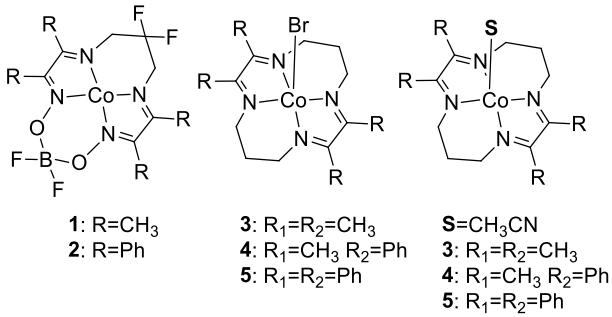


**Figure 2.10**. Cobalt tetraimine complexes tested in HERs as electrocatalysts [reproduced from ref. 30].

Compound **1** showed low overpotential values in HERs (~40mV; $E_{H^+/H}$ = −0.55 V vs. SCE). As an example, the diphenylglyoxime complex **2**[32] showed a more positive $Co^{II}/Co^{I}$ redox couple of −0.28V: nonetheless it exhibited lower activity. Other complexes (**3-5**) were characterized by more positive $Co^{II}/Co^{I}$ potentials and thereby a more positive proton reduction potential, conversely they displayed lower activity and required stronger acids for the reduction to occur.

In a different study, Stubbert *et al.*[33] found that a cobalt *bis*-(iminopyridine) molecule 6 (Figure 2.11) showed a good activity for proton reduction in aqueous media. A faradaic efficiency of 87 ± 10% was obtained at −1.4 V vs. SCE in aqueous buffered solutions. The complex was also electro-active over a wide range of pH values.

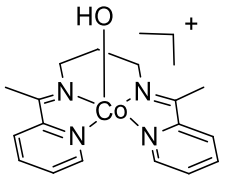


**6**

**Figure 2.11.** Cobalt *bis*-(iminopyridine) proposed by Stubbert. $Co^{2+}$ is present in the complex.

Synthetic Cobalt porphyrins (CoP) were also tested for HERs. Porphyrins provided four ligands to the cobalt center and they could be easily modified to improve performance. Nocera *et al.*[34] reported functionalized porphyrins with xanthene (Figure 2.12). Their activity as electrocatalysts was investigated using benzoic acid as the proton source. These systems showed higher overpotential values, if compared with the aforementioned cobalt complexes (~800 mV). Interestingly, in these complexes the substitution of bromide with a carboxylic acid on the xanthene moiety lowered the overpotential value of 120 mV. This improvement, defined to as the "hangman effect", relies on the assistance by the COOH group of the proton coupled electron transfer (PCET) process, facilitating hydrogen production. PCET was found to be three orders of magnitude faster when a carboxylic acid functionality was present in the close proximity of the Co ion.[34]

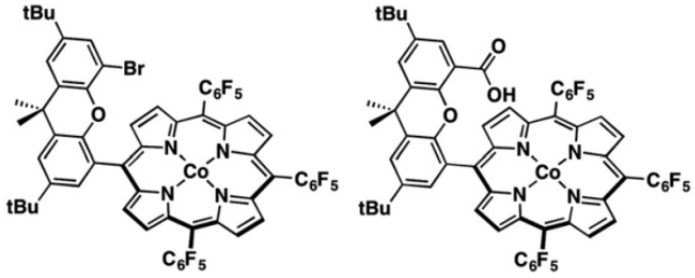


**Figure 2.12.** Cobalt porphyrins (CoPs) with xanthene moieties [reproduced from ref. 34].

Bren *et al.*[35] reported the first example of bioinorganic catalyst for HERs, involving the use of $Co^{III}$-MP11 (Figure 2.13 A). As reported earlier (Chapter 1.2), the latter is a water-soluble heme-undecapeptide, containing a heme *c* group covalently attached by two thioether bonds to the peptide chain in a CXXCH motif. His provided by peptide chain coordinate heme at to the proximal. $Co^{III}$-MP11 was reported to be active under electrochemical and photocatalytic conditions in the proton reduction reactions. In aqueous solution and at pH 7.0, this system demonstrated to be $O_2$-tolerant and to operate with a near quantitative Faradaic efficiency, with a TOF ~6.7 $s^{-1}$ and an overpotential value of 852 mV. However, $Co^{III}$-MP11 bleached rapidly in a few hours, cycling $2.5 \times 10^4$ times.[35]

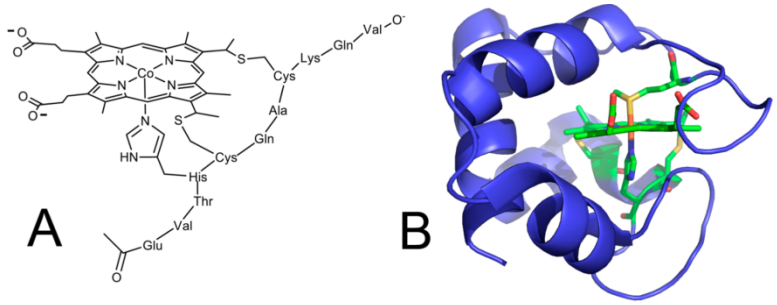


**Figure 2.13. a)** Schematic representation of Co-MP-11. **b)** Cytochrome c552 (Ht c-552) [taken from ref. 27].

A stronger catalyst was obtained by the replacement of Fe with Co in *Hydrogenobacter thermophilus* cytochrome c552 (Ht c-552) and engineering the active site to obtain the mutant Ht-CoM61A.[27] This modification allowed to obtain an interesting enzyme with hydrogen evolution activity. Similar to Co-MP11, the active site of Ht c-552 presents a heme *c* and a His residue as the axial ligand. To allow it to be active, the Met61 thioether side chain (acting as the distal heme ligand, Figure 2.13B) was mutated into an alanine. This mutation allowed for opening a ligand-binding site at the heme. Ht-CoM61A at pH 7 showed an overpotential value of 800mV and a Faradaic efficiency of 92 ± 8%, closer to that of MP11, but a much higher TON ($2.7 \times 10^5$).

## 2.1.7 INSIGHT INTO THE HER MECHANISM CATALYZED BY CO-PORPHYRINS

Cobalt complexes catalyze hydrogen evolution by different mechanisms.[30] It is not possible to explain the HER mechanism by a single pathway because the preferred one depends on the nature of the metal ligand, the starting oxidation number, and the basicity of the metal center. Moreover, the isolation of the reaction intermedia is not always possible.

Starting from Co-porphyrins, all possible catalytic pathways are below represented (Figure 2.14):

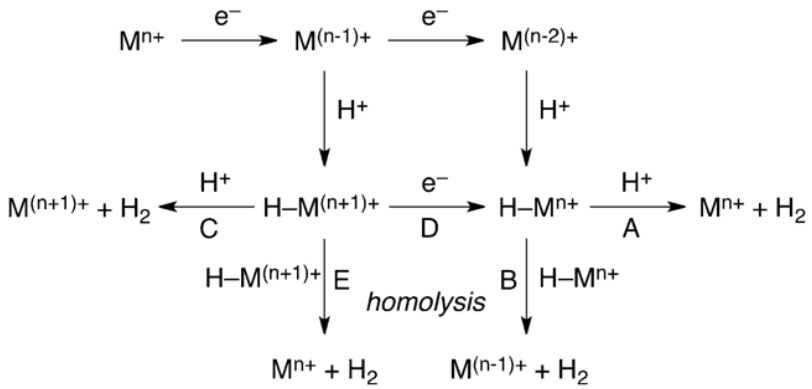


**Figure 2.14.** Different pathways regarding HERs for a given metal M [reproduced from ref. 30].

Hydrogen evolution require two electrons and two protons, then starting from ($Co^{n+}$) two different pathways are possible:

1. A double reduction, followed by a double protonation: "EEHH";
2. An alternate reduction/protonation: "EHEH".

In EEHH, $Co^{(n)+}$ achieves the oxidation state $Co^{(n-2)+}$ by two electrons reduction. $Co^{(n-2)+}$ is subsequently protonated to give the $HCo^{(n)+}$ intermediate. The latter is then protonated to give hydrogen and $Co^{(n)+}$, closing the cycle.

In EHEH, $Co^{(n)+}$ is reduced by a one electron process, achieving the oxidation number $Co^{(n-1)+}$, which is protonated by one proton giving $HCo^{(n+1)+}$. The latter is then reduced by a second electron, to give $HCo^{(n)+}$, which protonation releases hydrogen and $Co^{(n)+}$, closing the cycle.

The preferred pathway depends on catalyst's basicity and on acid's strength (Figure 2.15). For strong acids, hydrogen was thought to be evolved from HCo(III) complex, whereas for acids having intermediate strength, final protonation occurrs after reduction of HCo(III) to HCo(II). For weak acids, Co(I) was thought to be further reduced to Co(0) before protonation to HCo(II), followed by a second protonation.[36]

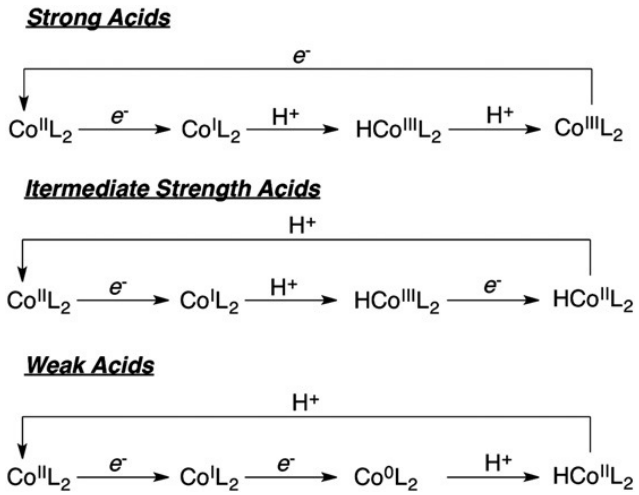


**Figure 2.15.** Key intermediates depending on the media acidity [reproduced from ref. 30].

# *CHAPTER 2.2*

## *Hydrogen Evolution Catalyzed by a Water-Soluble Metalloprotein Model*

## 2.2.1 $Co^{III}$-MC6a: SYNTHESIS AND CHARACTERIZATION

In the context of our ongoing program directed toward the achievement of novel catalytic applications of artificial metalloenzymes, we have herein studied the reactivity of a $Fe^{III}$-MC6a derivative containing a $Co^{III}$ ion ($Co^{III}$-MC6a), to investigate the potential use of this catalyst in proton reduction reactions, in view of its employ for water splitting experiments.

Cobalt was inserted in *apo*-Mimochrome VIa (obtained as reported in Chapter 1.3) using a slight modification of the standard acetate method, already described for $Fe^{III}$-MC6a.

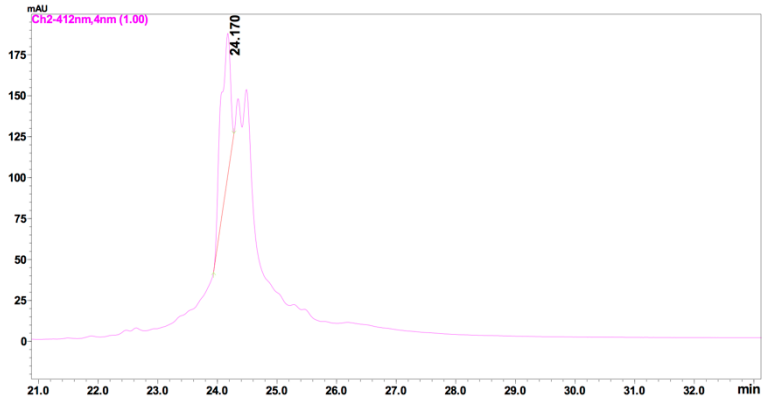


**Figure 2.16.** HPLC profile related to cobalt insertion in *apo*-MC6a. The numerous peaks are due to the partial separation of two regioisomeric species and, for each regioisomer, of two stereoisomers.

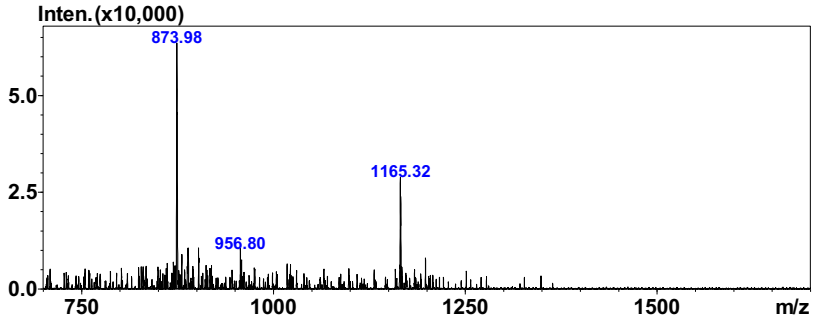


**Figure 2.17.** ESI-MS of $Co^{III}$-MC6a. The mass values at $m/z$ 1165.32 $[M+3H^+]$ and 873.98 $[M+4H^+]$ are consistent with theoretical value of 3493 Da $([M+H]^+)$.

As reported in Figure 2.16, HPLC analysis related to the cobalt insertion reaction gave four peaks. ESI-MS analysis of these peaks revealed that all had same mass values ($m/z$ 1165.32 and 873.98; Figure 2.17), which were consistent with the theoretical multi-charge ions 1165.38 $([M+3H]^{3+})$ and 874.29 $([M+4H]^{4+})$. In line with previous results reported for other members of Mimochrome's family,[37] the peaks were correlated to two regioisomeric species (since in DPIX two chemically different propionic acids are available for coupling) and, for each regioisomer, to two stereoisomeric (Δ and Λ) species (due to histidine coordination above or below the porphyrin ring). The separation between Δ and Λ isomers is especially apparent in Co-containing porphyrins rather than in Fe-porphyrins, since the coordination of His to cobalt occurs stably even under the acidic conditions used for HPLC analysis. Conversely, in Fe-porphyrins a rapid interconversion between the two species occurs, so that no separation can be achieved in this case.

UV-Vis analysis of $Co^{III}$-MC6a showed a Soret band at 412 nm and two Q bands at 523 and 554 nm, which were characteristic of Co(III)-porphyrins (Figure 2.18).[38] To provide further

confirmation the oxidation state of the metal ion, $Co^{II}$-MC6a was obtained treating the solution with a large excess (100-fold) of sodium dithionite. Compared to the previous spectrum, the UV-Vis profile of the reduction product showed a shift of the Soret band to 385 nm and a broadening of the Q band centered at 550 nm (Figure 2.18).[39]

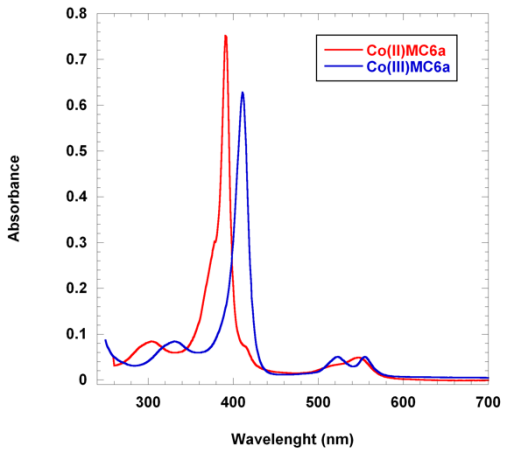


**Figure 2.18.** Overlapped UV-Vis spectra of 1 μM $Co^{III}$-MC6a (blue line) and $Co^{II}$-MC6a (red line) in $H_2O$ 0.1% TFA (pH 2). $Co^{II}$-MC6a was obtained treating the solution with 100-fold of sodium dithionite.

The determination of the molar extinction coefficient (ε) for $Co^{III}$-MC6a was carried out by spectroscopic studies. First, the concentration of an enzyme solution was determined by atomic absorption spectroscopy (AAS) after mineralization of the latter with concentrated $HNO_3$. Then, UV-vis measurements and the application of the Lambert-Beer's law enabled to correlate this concentration with the ε value. Under these conditions, the ε value was found to be $(1.47 \pm 0.1)*10^5\ L \cdot mol^{-1} \cdot cm^{-1}$.

In order to study the secondary structure of $Co^{III}$-MC6a, CD analysis of the enzyme in the far-UV region were then performed

(Figure 2.19). Analogously to $Fe^{III}$-MC6a, CD studies were acquired using different TFE concentrations. As TFE percentage increased, the wavelength of the minimum shifted from 202 nm to 207 nm; the ellipticity at 222 nm decreased; [θ]ratio increased from 0.42 to 0.77; $\lambda_0$ shifted from 194.2 nm to 199.4 nm.

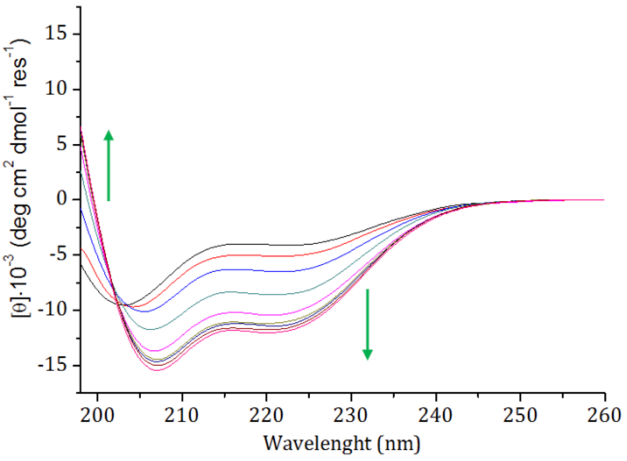


**Figure 2.19.** CD spectra in far UV region of $Co^{III}$-MC6a at different TFE concentrations. The green row summarizes how the curves changes during the titration.

Analogously to $Fe^{III}$-MC6a, TFE assisted the catalyst folding, the α-helix content increased, reaching a *plateau* at 30% of TFE (data not shown). Overall, the substitution of iron with cobalt did not change the amount of the secondary structure.

## 2.2.2 EVALUATION OF THE CATALYTIC POTENTIAL OF $Co^{III}$-MC6a IN HYDROGEN EVOLUTION

The activity of $Co^{III}$-MC6a as electrocatalyst for the hydrogen evolution reaction was evaluated in neutral buffer solutions. In a first short time (700 s), controlled potential electrolysis (CPE) of the total flowing charges was investigated by varying the electrolytic applied potential. All the experiments were carried out with 1 μM $Co^{III}$-MC6a in 2 M potassium phosphate buffer, the applied potentials ranged from -0.75 to -1.35 V vs SHE. Mercury pool was chosen as the working electrode because of its large cathodic window. As shown in Figure 2.20, the flowing charges were negligible with lower applied potential, they become appreciable at -1.05 V vs SHE with a significant increase at -1.25V vs SHE. Further increment of potential (-1.35V vs SHE, black curve) did not produce increase in current, thus indicating that proton reduction occurs in the proximity of -1.25 V vs SHE.

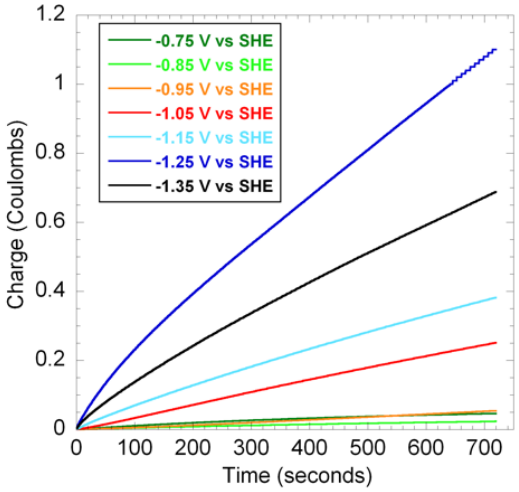


**Figure 2.20.** Short CPE experiments of 1 μM $Co^{III}$-MC6a in 2 M phosphate buffer (pH 7) at different applied potentials.

After 700 s of electrolysis with an applied potential of -1.25 V vs SHE, cell headspace was analyzed by gas chromatography (GC), which confirmed the production of hydrogen (Figure 2.21).

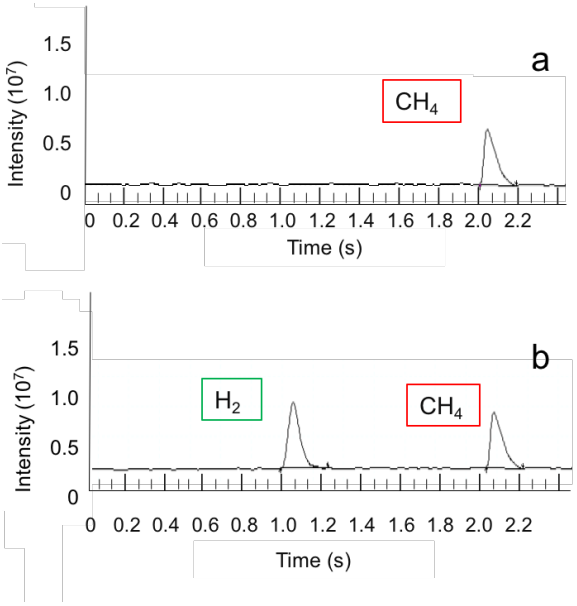


**Figure 2.21**. GC profile of CPE cell headspace after 700 s of 1 μM Co-MC6a solution in 2 M phosphate buffer (**a**, blank; **b**, with catalyst).

In order to confirm the role of $Co^{III}$-MC6a as electro-active catalyst in HERs, CPE experiments using *apo*-MC6a, $Fe^{III}$MC6a and cobalt chloride ($CoCl_2$) were also performed under the same reaction conditions of previous $Co^{III}$-MC6a CPE experiment (Figure 2.22). However, only $Co^{III}$-MC6a produced a significant charge increase with respect to the back ground (black curve).

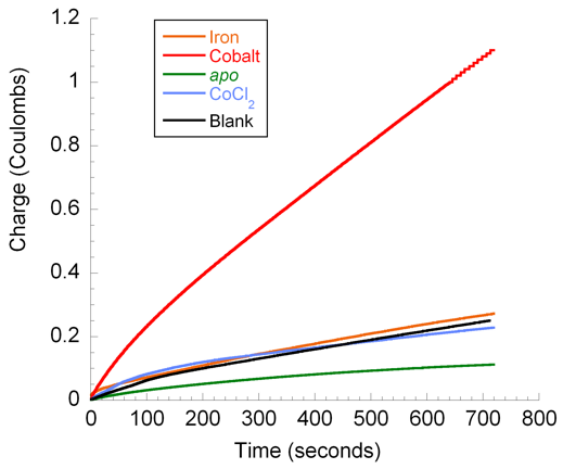


**Figure 2.22.** Bulk electrolysis for different MC6a congeners. All catalysts were used in a concentration of 1 μM at pH 7 (2 M phosphate buffer), applying a potential of -1.25 V vs SHE.

Further characterization studies of $Co^{III}$-MC6a were performed by cyclic voltammetry (CV) (Figure 2.23). Experiments were acquired using a 1 μM solution of $Co^{III}$-MC6a in 50 mM phosphate buffer (pH 7), using a hanging mercury drop electrode (HMDE) as the working electrode. CV was characterized by an irreversible cathodic peak centered at -1.2 V vs SHE, with onset potential of -1.0 V vs SHE. Considering the standard potential for proton reduction at pH 7 (E°') the overpotential value for $Co^{III}$-MC6a was -0.796 mV.

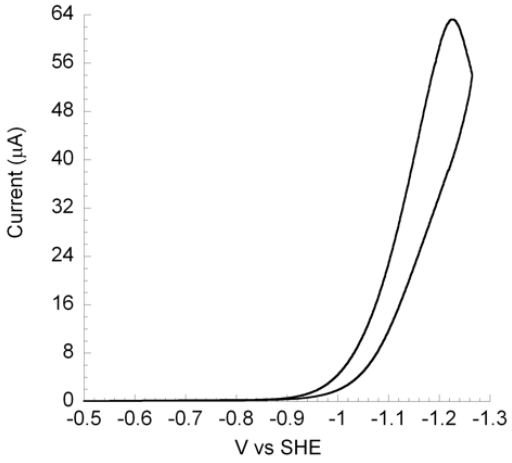


**Figure 2.23.** Cyclic voltammetry of HER catalyzed by 1 μM $Co^{III}$-MC6a in 25 mM phosphate buffer and 0.5 M KCl (pH 7), scan speed 100 mV/s mercury drop area of 0.038 $cm^2$.

The CV profile and particularly the peak current ($i_p$) appeared to be dependent on catalyst concentration. Using a mercury drop area of 0.038 $cm^2$, the cathodic peak currents were plotted as a function of $Co^{III}$-MC6a concentration (Figure 2.24). A linear increment of $i_p$ was observed, as long as catalyst concentration increased. With a further $Co^{III}$-MC6a concentration increment (higher than 2 μM), $i_p$ did not increase linearly. This can be explained considering that the reaction occurs at the mercury drop/solution interface, with conceivably a higher concentration of catalyst around the mercury drop. In such a crowded situation, not all $Co^{III}$-MC6a molecules are assumed to be able to catalyze the reaction; even worst, the multitude of catalysts could to interfere with the HER (determining a decrease in $i_p$).

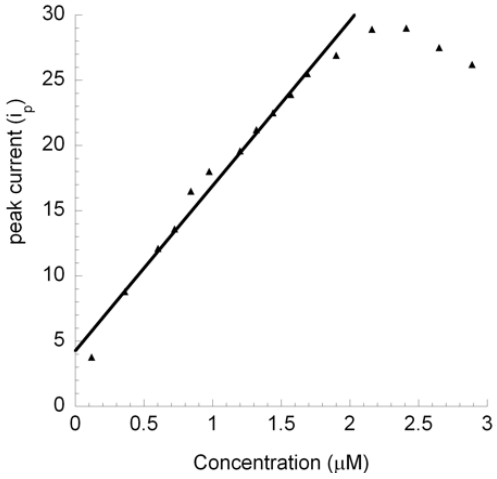


**Figure 2.24.** Peak current as a function of $Co^{III}$-MC6a concentration in 25 mM phosphate buffer and 0.5 M KCl (pH 7). The points with concentration ranging from 0.2 μM to 2 μM show a linear increment of peak current with respect to catalyst concentration (black line). Afterwards, saturation produces a decrease in $i_p$.

In a subsequent set of experiments, the activity of $Co^{III}$-MC6a was studied over a wide range of pH values (from 4.4 to 8.2). As pH increased, the peak current decreased as consequence of the lower proton concentration, although no shift of the potential peak ($E_p$) values was observed (Figure 2.25). Worthy to note, $Co^{III}$-MC6a exhibited activity until pH 8.2. This result is interesting especially considering of combining HER with Oxygen Evolving Reaction (OER), to obtain a whole water splitting process. OER is more complicated to accomplish compared to HER, and it is more favored at basic pH,[40] therefore a catalyst able to evolve hydrogen in neutral/basic pH values is a particularly valuable goal.

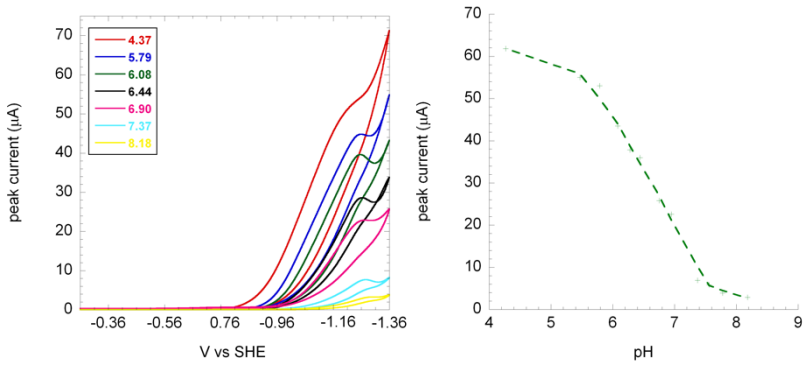


**Figure 2.25. Left:** cyclic voltammograms of 1 µM $Co^{III}$-MC6a at different pH values in 25 mM phosphate buffer and 0.5 M KCl . **Right:** plotting of peak currents as a function of pH.

Kinetic parameters were determined by CPE experiments ran under $N_2/CH_4$ atmosphere for several hours (15 h). After 10 min of electrolysis using 0.2 µM catalyst while applying a potential of −1.2 V vs SHE in 2 M KPi (pH 7), 4.5 coulombs were passed. The hydrogen evolved was determined by GC analysis of the cell headspace, using methane as the internal standard. An amount of 27.4 µmol of hydrogen was produced, which corresponded to a Faradaic efficiency (after background subtraction) of 93 ± 6%. A turnover frequency of 4.6 $s^{-1}$ was also measured.

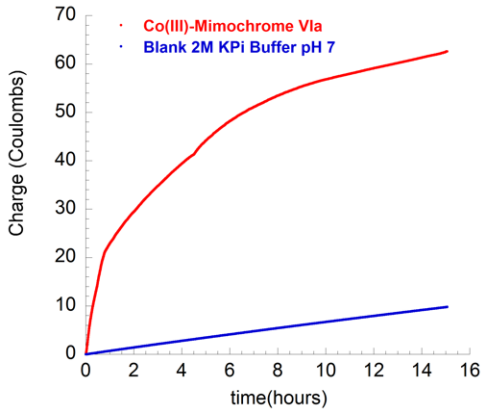


**Figure 2.26.** Bulk electrolysis over 15 h of 1 μM $Co^{III}$-MC6a in 2 M phosphate buffer at pH 7.

$Co^{III}$-MC6a showed the highest catalytic activity within the first 8 h, afterwards the current started to decrease, even though it showed activity up to 15 h. Considering the Faradaic efficiency as constant all over the electrolysis experiment, a TON of $3 \cdot 10^5$ was measured over 15h. (Figure 2.26).

The role of enzyme folding on proton reduction reaction was then explored by performing different CV studies by $Co^{III}$-MC6a varying the concentration of TFE. As shown in Figure 2.27, the peak current decreased, as consequence of the increase of TFE concentration from 0% to 40% (v/v). Furthermore, peak potential ($E_p$) was accompanied by a shift toward more positive values. Overpotential values decreased down to -0.746 mV.

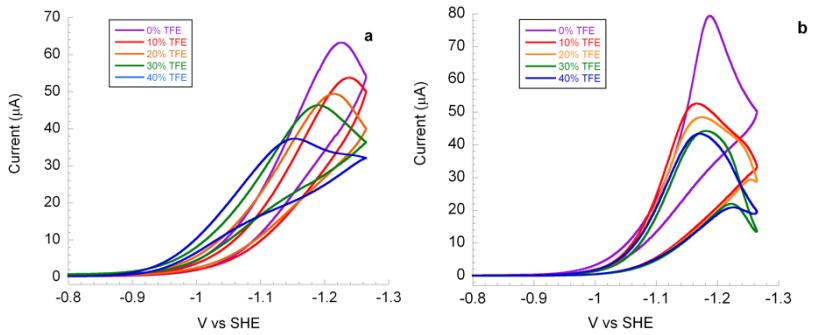


**Figure 2.27. a)** CV experiments of 1 µM $Co^{III}$-MC6a at varying TFE concentration in 25 mM phosphate buffer and 0.5 M KCl (pH 7). **b)** CV experiments of $Co^{III}$-MP11 in 25 mM phosphate buffer and 0.5 M KCl (pH 7) at varying TFE concentration.

To rationalize the data obtained, the experiment was repeated using $Co^{III}$-MP11 as electrocatalyst for HER under the same conditions. The latter displayed a different behavior. Indeed, cyclic voltammograms of $Co^{III}$-MP11 showed a decrease in the peak current as consequence of TFE addition, but this effect was not followed by changes in the $E_p$ and then in the overpotential values. The differences between the two catalysts are summarized below (Figure 2.28). On one hand, the reduction of $E_p$ as a function of TFE concentration was reported (Figure 2.28, left side), pointing out the marked decrease observed with $Co^{III}$-MC6a, while with $Co^{III}$-MP11 the $E_p$ value was substantially unvaried. On the other hand, the $i_p$ decrease as a function of TFE concentration is highlighted (Figure 2.28, right side), revealing that the peak current reduction is significantly minor in the case of Co-MC6a (from 65 to 40 µA) than in the case of $Co^{III}$-MP11 (from 80 to 40 µA).

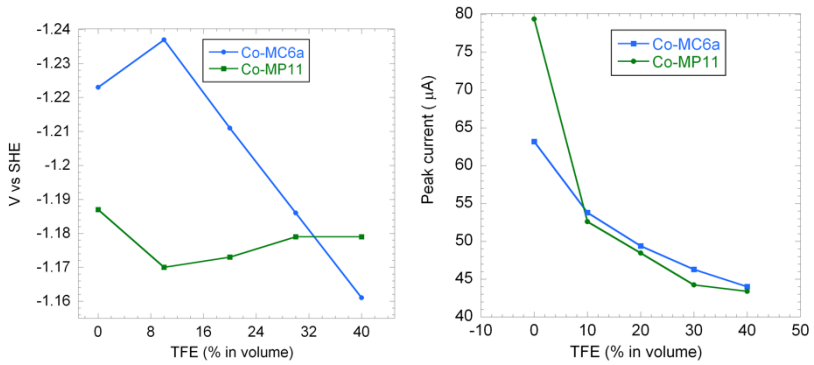


**Figure 2.28. Left:** plotting of peak potential $E_p$ as a function of TFE concentration for both $Co^{III}$-MP11 and $Co^{III}$-MC6a. **Right:** peak current for HER as a function of TFE concentration for both $Co^{III}$-MP11 and $Co^{III}$-MC6a.

From these data, it is possible to conclude that the folding of $Co^{III}$-MC6a mediated by TFE affect the proton reduction reaction mechanism. The difference in the reactivity observed between the two catalysts can be explained analyzing the structural differences between them. $Co^{III}$-MC6a adopts a sandwich-like structure, with the decapeptide chain on the distal site acting as a "lid". Conversely, $Co^{III}$-MP11 composed by one single peptide chain in a random coil conformation. Both catalysts adopt an α-helical conformation upon TFE addition.[41]

We can assume that the main difference between the two catalysts is the presence of the decapeptide chain in $Co^{III}$-MC6a. Accordingly, TFE-mediated enzyme folding is able to affect the proton reduction in three ways:

1. when arranged into an organized structure, the decapeptide chain can provide a more hydrophobic environment, which can decrease the dielectric constant around the metal site;

2. The folding of the decapeptide allows the side chain to approach the metal center, acting as a proton shuttle, thus assisting catalysis (hangman effect). Given the structure of $Co^{III}$-MC6a, $Arg^{10}$ and $Glu^{2}$ can possibly exert this effect.
3. Folding-induced porphyrin distortion tunes the cobalt porphyrin potential, lowering the HER overpotential.

The first two hypotheses are easy to proof considering the $Co^{III}$-MC6a secondary coordination sphere. Indeed, the overpotential shift reported by Nocera *et al.*[34] due to the hangman effect on cobalt porphyrin, is in the same order of magnitude to the one observed for $Co^{III}$-MC6a. The hangman effect consists in a overpotential decrease when an acidic group is added over to the porphyrin distal face and then acts as a proton-shutter. This modification can cause a decrease in the overpotential of about 100 mV.

The effect of distortion is more complicated to proof.

Distortion of porphyrins is very common in proteins, nature uses protein matrix to alter porphyrin planarity to modulate the redox potential.[42] Cotton's effect observed on heme-proteins can be explained by multiple effects, one of them is ascribable to the porphyrin distortion from planarity, which gives rise to an inherent chirality.[43]

It's worth noting that in all members of MC6 family, CD spectra in the Soret region are strictly dependent from TFE concentration. It has been reported that CD signal increases (higher Cotton's effect) upon increasing TFE concentration.[32] The same behavior was observed for all MC6a members (data not shown). Then it is possible to suppose that the decrease in proton reduction potential observed in folded $Co^{III}$-MC6a could be also explained considering a more distorted porphyrin, due to

the higher structuration of the peptides mediated by TFE. This distortion could modulate the cobalt potential for the HER.

Further experiments will be necessary to investigate and assess what influences the catalytic shift of overpotential observed with $Co^{III}$-MC6a.

## 2.2.3 NEW $CO^{III}$-MC6a DERIVATIVES AS ELECTROCATALYSTS FOR HER

A Structure Activity Relationship (SAR) study aimed at identifying the existing correlation between coordination shell of Co-MC6a and its efficacy in proton reduction has eventually been herein approached. The final aim of this work was the identification of the chemical space enabling further improvement in the catalytic potential to perform HERs by our Mimochromes.

In order to reduce the proton to hydrogen, cobalt has to reach low oxidation numbers (ON).[34] Stabilization of cobalt ion in low ONs (which means, reduced transition state (TS) energy) implies that less energy (potential) is necessary to reach the TS. Accordingly, a lower potential (in absolute value) is needed to reduce the cobalt center, and likely less potential to reduce protons. The π-acceptor ligands are characterized by π* antibonding orbitals, which are able to accept electrons from the metal center. In π-back-donation mediated by π-acceptor ligands, the electrons deriving from metal are used to bind the ligand, in this process cobalt electrons are dislocated on ligand orbitals, thereby π-acceptor ligands stabilize low oxidation numbers.[44,45]

Based on this observation, the synthesis of two new analogues was conceived by replacing the proximal His with the two aminoacids: ornithine and the not natural 3-(3-pyridyl)-L-alanine.

3-(3-Pyridyl)-L-alanine (3'pyAla) presents a pyridine moiety as side chain group. Pyridine was chosen because it presents a greater π-acceptor character compared to the imidazole group in His. Conversely, Ornithine (Orn) bears an amino function as the axial ligand, which is not a π-acceptor ligand, but rather a *n*-donating ligand. Orn variant was chosen as a negative proof of

our hypothesis. In both His$^6$Orn-MC6a and His$^6$(3'py)Ala-MC6a, the decapeptide chains were unvaried with respect MC6a. The sequences for the new tetradecapeptide chains are reported below:

**His$^6$Orn-MC6a**
Ac-Asp$^1$(tBuO)-Leu$^2$-Gln$^3$(Trt)-Gln$^4$(Trt)-Leu$^5$-**Orn$^6$(Boc)**-Ser$^7$(tBu)-Gln$^8$(Trt)-Lys$^9$(Mmt)-Arg$^{10}$(Pbf)-Lys(Boc)$^{11}$-Ile$^{12}$-Thr(tBu)$^{13}$-Leu$^{14}$-$NH_2$

**His$^6$3'pyAla-MC6a**
Ac-Asp$^1$(tBuO)-Leu$^2$-Gln$^3$(Trt)-Gln$^4$(Trt)-Leu$^5$-**(3'py)Ala$^6$**-Ser$^7$(tBu)-Gln$^8$(Trt)-Lys$^9$(Mmt)-Arg$^{10}$(Pbf)-Lys(Boc)$^{11}$-Ile$^{12}$-Thr(tBu)$^{13}$-Leu$^{14}$-$NH_2$

The peptides were synthesized via SPPS, using the standard Fmoc chemistry on a 0.1 mmol scale. The deprotection, coupling with DPIX, and purification stages were the same as for MC6a. Once obtained the pure *apo*-His$^6$(3'py)Ala-MC6a and *apo*-His$^6$Orn-MC6a, cobalt was inserted in the catalysts following the usual acetate method.

In preliminary studies, the activity of His$^6$Orn-MC6a in HER was analyzed performing CV of 1 μM catalyst in 50 mM phosphate buffer (pH 7), using hanging mercury drop electrode as working electrode (Figure 2.29).

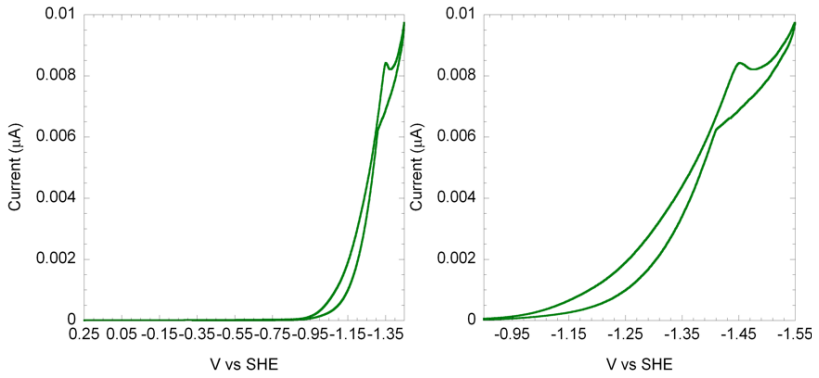


**Figure 2.29. Left:** cyclic voltammograms for His$^6$Orn-MC6a in 25 mM phosphate buffer and 0.5 M KCl (pH 7). **Right:** zoom-in of potential range from -0.90 to -1.55 V vs SHE.

The cyclic voltammogram for the HER catalyzed by His$^6$Orn-MC6a was characterized by an irreversible cathodic peak centered at -1.45 V vs SHE, with onset potential of -1.17 V vs SHE. Considering the standard potential for proton reduction at pH 7 (E°'), the overpotential for His$^6$Orn-MC6a was determined to be -1.04 mV. The overpotential shift of 0.244 V toward more negative potential values supports the initial hypothesis that a ligand with a greater n-donating character with respect to His, such as the amino group of Orn, limits the proton reduction reaction. More extensive SAR studies, especially those using the Co$^{III}$-His$^6$(3'py)Ala-MC6a analogue, will need to be performed, with the aim to provide a more robust confirmation of our working hypothesis on the correlation between cobalt reduction potential and the proton reduction. Studies are also currently ongoing on performing CV analyses of these new compounds in organic solvents (such as DMF), with the aim to this study this correlation in a non protic solvent and thereby appreciate the only contribution of Co reduction.

# *CHAPTER 2.3*

## *Concluding Remarks and Outlook*

Among natural hydrogenases and artificial biomimetics thereof, $Co^{III}$-MC6a represents an interesting candidate in HER. Indeed, this new enzyme demonstrates to catalyze the proton reduction reactions in neutral water and in the presence of dioxygen. Kinetic parameters of $Co^{III}$-MC6a such as overpotential and Faradaic efficiency were similar to other cobalt (III) porphyrin derivatives. However, especially if correlated to $Co^{III}$-MP11, $Co^{III}$-MC6a has demonstrated to work with much higher TON (up to 300000) as well as to retain its activity for several hours longer. The difference in the TON between the two catalysts has been rationalized considering that $Co^{III}$-MP11 presents an "open" active site with a porphyrin ring directly in contact with the solvent. On the other hand, the robustness of $Co^{III}$-MC6a was attributed to the presence of the *D* chain, which protects the catalyst against undesired bleaching.

The effect of peptide folding on the catalytic efficiency has also been studied. TFE-mediated $Co^{III}$-MC6a folding has proved to cause a shift of the peak potential toward less negative values (lower overpotential) and concurrently a decrease in the $i_p$. By comparison, in $Co^{III}$-MP11 TFE addition caused a decrease in the $i_p$, but not a change in the peak potential. Various hypotheses have been formulated to rationalize the correlation between peptide folding and catalytic efficiency. Considering the structural differences between the two catalysts, the most conceivable cause has been identified in the effect of an acidic group approaching the metal center (the hangman effect). Indeed, this modification has been suggested to cause a decrease in the overpotential value of about 100 mV. The overpotential decrease observed during the $Co^{III}$-MC6a folding has been found in line with that reported in the hangman porphyrins reported by Nocera. Moreover, $Arg^{10}$ and $Glu^{2}$ residues in the decapeptide chain have been supposed to be close enough to exert the hangman effect.

New MC6a analogues have been eventually designed for SAR studies. In particular, an analysis of the existing correlation between coordination shell of the enzyme and its efficacy in proton reduction has been undertaken, through the mutation of proximal His with two amino acid residues, i.e. Orn and (3'py)Ala, which have been conceived to provide as axial ligands an amino or a pyridinyl group, respectively. The analogues were synthetized and $Co^{III}$-His$^{6}$Orn-MC6a was preliminary tested in HER. Interestingly, $Co^{III}$-His$^{6}$Orn-MC6a is active in proton reduction, showing a shift in the peak potential toward more negative values, which supports in part the starting hypothesis.

Overall, the obtained results allow us to point out that the new artificial enzymes coming from the last generation of Mimochromes hold powerful activity and represent suitable candidates for applications in hydrogen evolution. Ongoing endeavors are in progress, to identify the structural requirements for enzymatic activity, in order to develop even higher performing catalysts than natural metalloenzymes.

# CHAPTER 2.4

## *Materials and Methods*

## 2.4 MATERIALS AND METHODS

Electrochemical experiments were carried out with a 620D potentiostat (CH Instruments). Ag/AgCl (1 M KCl) and platinum wires were used as reference and counter electrode, respectively. Controlled potential electrolysis (CPE) was performed in a custom electrolysis cell (Adams & Chittenden) with three equi-volume chambers of 1.5 cm diameter and 6 cm height. The chambers are separated by 10-mm diameter P5 (1.0-1.6 μm pore size) glass, the central cell compartment contains the mercury pool electrode, which is connected to the potentiostat through an insulated platinum wire, each compartment was sealed by a gas-tight septum. Cyclic voltammetry (CV) experiments were performed with a hanging mercury drop electrode (HMDE) from Institute of Physical Chemistry of the Polish Academy of Sciences. pH was monitored using a VWR SB70P pH-meter and a Mettler Toledo InLab semimicro pH probe. GC analysis was carried out on a Shimadzu GC-17A injection temperature 110 °C (direct injection), nitrogen was used as carrier gas with a pressure of 34 kPa, oven temperature at 28 °C and a detector temperature at 140 °C.

Catalytic activity of CoMC6a in hydrogen evolution reaction (HER) was characterized by electrochemistry. Controlled Potential Electrolysis (CPE) was used to determinate the catalytic parameters, Cyclic Voltammetry (CV) was used to explore catalyst behavior in different experiment condition. In both cases, mercury was chosen as working electrode because of its large cathodic window and low background in water. CPE studies were performed using 5 mL of 0.2 M CoMC6a in 2 M potassium phosphate buffer (pH 7.0). Before each experiment, the cell was purged for 15 min with a $N_2/CH_4$ mixture (8/2), methane was used as the internal standard. Hydrogen ($H_2$)

quantification was performed by GC analysis of cell head space. The ratio between hydrogen and methane peak areas was compared with a standard calibration curve. Therefore, turnover number (TON), turnover frequency (TOF) and Faradic efficiency were calculated using the following equations:

Faradaic efficiency (%) = (ne • F)/QT • 100%

TON = n ($H_2$)/n (CoMC6a)

TOF = TON/t

The general procedure for cyclic voltammetry is as follows: 5 mL of 1 μM CoMC6a in 0.5 M KCl and 25 mM potassium phosphate buffer was used. Each measurement was repeated twice and a fresh mercury drop (surface area 0.038 cm2) was used for each experiment. Before start, the solution was purged 15 min with nitrogen. The measurements were performed under gentle nitrogen flow. pH titration was performed adjusting the pH value with amounts of 2 M NaOH or HCl.

# *REFERENCES*

1. Han, Z. & Eisenberg, R. Fuel from Water: The Photochemical Generation of Hydrogen from Water. *Acc. Chem. Res.* **47,** 2537–2544 (2014).
2. Bren, K. L. Multidisciplinary approaches to solar hydrogen. *Interface Focus* **5,** (2015).
3. Roger, I., Shipman, M. A. & Symes, M. D. Earth-abundant catalysts for electrochemical and photoelectrochemical water splitting. *Nat. Rev. Chem.* **1,** s41570-016-0003-016 (2017).
4. Lubitz, W., Ogata, H., Rüdiger, O. & Reijerse, E. Hydrogenases. *Chem. Rev.* **114,** 4081–4148 (2014).
5. Alstrum-Acevedo, J. H., Brennaman, M. K. & Meyer, T. J. Chemical Approaches to Artificial Photosynthesis. 2. *Inorg. Chem.* **44,** 6802–6827 (2005).
6. McCrory, C. C. L. *et al.* Benchmarking Hydrogen Evolving Reaction and Oxygen Evolving Reaction Electrocatalysts for Solar Water Splitting Devices. *J. Am. Chem. Soc.* **137,** 4347–4357 (2015).
7. Esswein, A. J. & Nocera, D. G. Hydrogen production by molecular photocatalysis. *Chem. Rev.* **107,** 4022–4047 (2007).
8. Vignais, P. M., Billoud, B. & Meyer, J. Classification and phylogeny of hydrogenases. *FEMS Microbiol. Rev.* **25,** 455–501 (2001).
9. Vincent, K. A., Parkin, A. & Armstrong, F. A. Investigating and Exploiting the Electrocatalytic Properties of Hydrogenases. *Chem. Rev.* **107,** 4366–4413 (2007).
10. Happe, R. P., Roseboom, W., Pierik, A. J., Albracht, S. P. & Bagley, K. A. Biological activation of hydrogen. *Nature* **385,** 126 (1997).
11. Fontecilla-Camps, J. C., Amara, P., Cavazza, C., Nicolet, Y. & Volbeda, A. Structure-function relationships of anaerobic gas-processing metalloenzymes. *Nature* **460,** 814–822 (2009).
12. Volbeda, A. *et al.* Crystal structure of the nickel-iron hydrogenase from Desulfovibrio gigas. *Nature* **373,** 580–587 (1995).

13. YAGI, T. & HIGUCHI, Y. Studies on hydrogenase. *Proc. Jpn. Acad. Ser. B Phys. Biol. Sci.* **89,** 16–33 (2013).
14. Pandelia, M.-E., Ogata, H., Currell, L. J., Flores, M. & Lubitz, W. Probing intermediates in the activation cycle of [NiFe] hydrogenase by infrared spectroscopy: the Ni-SIr state and its light sensitivity. *J. Biol. Inorg. Chem.* **14,** 1227–1241 (2009).
15. Bleijlevens, B., Faber, B. W. & Albracht, S. P. The [NiFe] hydrogenase from Allochromatiumvinosum studied in EPR-detectable states: H/D exchange experiments that yield new information about the structure of the active site. *JBIC J. Biol. Inorg. Chem.* **6,** 763–769 (2001).
16. Parkin, A. & Sargent, F. The hows and whys of aerobic H2 metabolism. *Curr. Opin. Chem. Biol.* **16,** 26–34 (2012).
17. Evans, R. M. *et al.* Principles of sustained enzymatic hydrogen oxidation in the presence of oxygen--the crucial influence of high potential Fe-S clusters in the electron relay of [NiFe]-hydrogenases. *J. Am. Chem. Soc.* **135,** 2694–2707 (2013).
18. Madden, C. *et al.* Catalytic turnover of [FeFe]-hydrogenase based on single-molecule imaging. *J. Am. Chem. Soc.* **134,** 1577–1582 (2012).
19. Mulder, D. W. *et al.* Insights into [FeFe]-hydrogenase structure, mechanism, and maturation. *Struct. Lond. Engl. 1993* **19,** 1038–1052 (2011).
20. Nicolet, Y., Lemon, B. J., Fontecilla-Camps, J. C. & Peters, J. W. A novel FeS cluster in Fe-only hydrogenases. *Trends Biochem. Sci.* **25,** 138–143 (2000).
21. Jablonskytė, A., Wright, J. A., Fairhurst, S. A., Webster, L. R. & Pickett, C. J. [FeFe] Hydrogenase: Protonation of {2Fe3S} Systems and Formation of Super-reduced Hydride States. *Angew. Chem. Int. Ed.* **53,** 10143–10146 (2014).
22. Mulder, D. W. *et al.* EPR and FTIR analysis of the mechanism of H2 activation by [FeFe]-hydrogenase HydA1 from Chlamydomonas reinhardtii. *J. Am. Chem. Soc.* **135,** 6921–6929 (2013).
23. Thauer, R. K. *et al.* Hydrogenases from methanogenic archaea, nickel, a novel cofactor, and H2 storage. *Annu. Rev. Biochem.* **79,** 507–536 (2010).
24. Thauer, R. K., Klein, A. R. & Hartmann, G. C. Reactions

with Molecular Hydrogen in Microorganisms: Evidence for a Purely Organic Hydrogenation Catalyst. *Chem. Rev.* **96,** 3031–3042 (1996).
25. Vogt, S., Lyon, E. J., Shima, S. & Thauer, R. K. The exchange activities of [Fe] hydrogenase (iron-sulfur-cluster-free hydrogenase) from methanogenic archaea in comparison with the exchange activities of [FeFe] and [NiFe] hydrogenases. *J. Biol. Inorg. Chem. JBIC Publ. Soc. Biol. Inorg. Chem.* **13,** 97–106 (2008).
26. Yang, X. & Hall, M. B. Monoiron hydrogenase catalysis: hydrogen activation with the formation of a dihydrogen, Fe-H(delta-)...H(delta+)-O, bond and methenyl-H4MPT+ triggered hydride transfer. *J. Am. Chem. Soc.* **131,** 10901–10908 (2009).
27. Kandemir, B., Chakraborty, S., Guo, Y. & Bren, K. L. Semisynthetic and Biomolecular Hydrogen Evolution Catalysts. *Inorg. Chem.* **55,** 467–477 (2016).
28. Trasatti, S. Work function, electronegativity, and electrochemical behaviour of metals: III. Electrolytic hydrogen evolution in acid solutions. *J. Electroanal. Chem. Interfacial Electrochem.* **39,** 163–184 (1972).
29. Sheng, W., Myint, M., Chen, J. G. & Yan, Y. Correlating the hydrogen evolution reaction activity in alkaline electrolytes with the hydrogen binding energy on monometallic surfaces. *Energy Environ. Sci.* **6,** 1509–1512 (2013).
30. Eckenhoff, W. T., McNamara, W. R., Du, P. & Eisenberg, R. Cobalt complexes as artificial hydrogenases for the reductive side of water splitting. *Biochim. Biophys. Acta* **1827,** 958–973 (2013).
31. Krishnan, C. V., Brunschwig, B. S., Creutz, C. & Sutin, N. Homogeneous catalysis of the photoreduction of water. 6. Mediation by polypyridine complexes of ruthenium(II) and cobalt(II) in alkaline media. *J. Am. Chem. Soc.* **107,** 2005–2015 (1985).
32. Hu, X., Brunschwig, B. S. & Peters, J. C. Electrocatalytic hydrogen evolution at low overpotentials by cobalt macrocyclic glyoxime and tetraimine complexes. *J. Am. Chem. Soc.* **129,** 8988–8998 (2007).
33. Stubbert, B. D., Peters, J. C. & Gray, H. B. Rapid Water Reduction to H2 Catalyzed by a Cobalt Bis(iminopyridine)

Complex. *J. Am. Chem. Soc.* **133,** 18070–18073 (2011).
34. Lee, C. H., Dogutan, D. K. & Nocera, D. G. Hydrogen Generation by Hangman Metalloporphyrins. *J. Am. Chem. Soc.* **133,** 8775–8777 (2011).
35. Kleingardner, J. G., Kandemir, B. & Bren, K. L. Hydrogen Evolution from Neutral Water under Aerobic Conditions Catalyzed by Cobalt Microperoxidase-11. *J. Am. Chem. Soc.* **136,** 4–7 (2014).
36. Baffert, C., Artero, V. & Fontecave, M. Cobaloximes as Functional Models for Hydrogenases. 2. Proton Electroreduction Catalyzed by Difluoroborylbis(dimethylglyoximato)cobalt(II) Complexes in Organic Media. *Inorg. Chem.* **46,** 1817–1824 (2007).
37. Costanzo, L. *et al.* Miniaturized heme proteins: crystal structure of Co(III)-mimochrome IV. *JBIC J. Biol. Inorg. Chem.* **9,** 1017–1027 (2004).
38. Kellett, R. M. & Spiro, T. G. Cobalt(I) porphyrin catalysts of hydrogen production from water. *Inorg. Chem.* **24,** 2373–2377 (1985).
39. Li, C., Nishiyama, K. & Taniguchi, I. Electrochemical and spectroelectrochemical studies on cobalt myoglobin. *Electrochimica Acta* **45,** 2883–2888 (2000).
40. Lu, X. & Zhao, C. Electrodeposition of hierarchically structured three-dimensional nickel–iron electrodes for efficient oxygen evolution at high current densities. *Nat. Commun.* **6,** ncomms7616 (2015).
41. Kadnikova, E. N. & Kostić, N. M. Effects of the environment on microperoxidase-11 and on its catalytic activity in oxidation of organic sulfides to sulfoxides. *J. Org. Chem.* **68,** 2600–2608 (2003).
42. Bowman, S. E. J. & Bren, K. L. The chemistry and biochemistry of heme c: functional bases for covalent attachment. *Nat. Prod. Rep.* **25,** 1118–1130 (2008).
43. Blauer, G., Sreerama, N. & Woody, R. W. Optical activity of hemoproteins in the Soret region. Circular dichroism of the heme undecapeptide of cytochrome c in aqueous solution. *Biochemistry (Mosc.)* **32,** 6674–6679 (1993).
44. Taube, R. The Stabilization of Low Oxidation States in σ-Organo Transition Metal Chemistry by Coordinative Lithium

Transition Metal Interaction. *Comments Inorg. Chem.* **3,** 69–81 (1984).
45. Han, Y. *et al.* Singly versus Doubly Reduced Nickel Porphyrins for Proton Reduction: Experimental and Theoretical Evidence for a Homolytic Hydrogen-Evolution Reaction. *Angew. Chem. Int. Ed Engl.* **55,** 5457–5462 (2016).